Spectroscopy of Colloidal Quantum Dots of Controlled Shape and Size

Arjen Toni Dijksman

▶ **To cite this version:**

Arjen Toni Dijksman. Spectroscopy of Colloidal Quantum Dots of Controlled Shape and Size. Micro and nanotechnologies/Microelectronics. Université Pierre et Marie Curie - Paris VI, 2013. English. NNT : . pastel-00876357

HAL Id: pastel-00876357
https://pastel.hal.science/pastel-00876357

Submitted on 24 Oct 2013

HAL is a multi-disciplinary open access archive for the deposit and dissemination of scientific research documents, whether they are published or not. The documents may come from teaching and research institutions in France or abroad, or from public or private research centers.

L'archive ouverte pluridisciplinaire **HAL**, est destinée au dépôt et à la diffusion de documents scientifiques de niveau recherche, publiés ou non, émanant des établissements d'enseignement et de recherche français ou étrangers, des laboratoires publics ou privés.

THÈSE DE DOCTORAT

PRÉSENTÉE A

L'UNIVERSITÉ PIERRE ET MARIE CURIE

ÉCOLE DOCTORALE n°389 : « La physique, de la particule à la matière condensée »

Par Arjen Toni DIJKSMAN

POUR OBTENIR LE GRADE DE

DOCTEUR

SPECTROSCOPIE DE BOITES QUANTIQUES COLLOÏDALES DE FORME ET TAILLE CONTROLEE

SPECTROSCOPY OF COLLOIDAL QUANTUM DOTS OF CONTROLLED SHAPE AND SIZE

Directeur de recherche : Benoit DUBERTRET

Soutenance le 27 septembre 2013

Devant la commission d'examen formée de :

M. Christophe	DELERUE	Rapporteur
M. Nikolay	GIPPIUS	Rapporteur
M. Alberto	BRAMATI	Examinateur
M. Mathieu	KOCIAK	Examinateur
M. Benoit	DUBERTRET	Directeur de thèse

To Nguyen Tan Tai, inspirer

Contents

1. Introduction

Studying physics, delving deeply into its fundamentals and those broad ideas on which it is based and, especially, independent scientific work bring enormous mental satisfaction.

Leonid Mandelstam

1.1. Context

The study of single nanostructures is fostering a great number of technological applications. Single nanostructures have very promising potential as exceptional photon emitters (single-photon emitters for quantum cryptography [1, 2], nanolasers [3, 4], light-emitting diodes [5] and resistant fluorophores in biomedical imaging [6, 7]), as well as highly efficient photon absorbers (photovoltaic devices [8]). Such nanostructures can be grown either epitaxially on a substrate or colloidally in solution or matrix. Both techniques have their advantages and disadvantages. Epitaxial growth allows better control of their insertion in devices, while colloidal synthesis yields higher efficiencies at room temperature and assures lower cost per unit production.

A key issue for any nanostructure technology is the optimization of single nano-object localization, while controlling its physical behaviour. Both localization and physical behaviour have statistical properties due to quantum indeterminacies inherent to the nanosized constituents. The present work is essentially motivated by this optimization issue. It is funded by a joint project of the Agence Nationale de la Recherche, for the DEterministic Implementation of LIGHT-matter control for efficient single photon sources (DELIGHT).

This research work has been performed at the Laboratoire de Physique et d'Etude des Matériaux (LPEM) of the Ecole Supérieure de Physique et de Chimie Industrielles (ESPCI), where the team directed by Benoit Dubertret has gained an acknowledged expertise in the synthesis and characterization of high-quality colloidal nanocrystals [9, 10, 11].

In the context of this scientific environment, the different aspects of this doctoral research work have been:

- Exploring the synthesis of colloidal core-shell CdSe/CdS semiconductor nanocrystals (also called quantum dots, QDs) in order to optimize their photoluminescence properties. Previous work in the group has been done by Benoit Mahler [12] and Clémentine Javaux [13], who have succeeded in developing a rapid and robust protocol that gives non-blinking QDs with quantum yields of 100%. This chemical synthesis part of the work is the subject of chapter 2.
- Characterizing single core-shell QDs with time-resolved confocal spectroscopy and electron microscopy techniques, including a collaboration on cathodoluminescence with the group of Mathieu Kociak at the Laboratoire de Physique des Solides (LPS) in Orsay. This physical characterization part is the subject of chapter 3.
- Modeling the energy-size dependence of semiconductor nanocrystals, using a phase jump approach for charge carriers represented by phasors and probing it on different nano-objects. This theory and modeling part is the subject of chapter 4.

This work has been done in the framework of the Ecole Doctorale 389 of the Université Pierre et Marie Curie: La physique, de la matière à la particule, directed by Jean Hare.

1.2. Semiconductors

Roughly said, semiconductors are materials that have an electrical conductivity that is intermediate between insulators and metals. In a graph, we like to situate the semiconductors in between insulators and conductors, with typical conductivity values ranging from 0.001 to 10^6S/m, see Fig. 1.1.

As can be seen on Fig. 1.1, the range over which the conductivity of semiconductors may vary is very wide. In proper conditions, the conductivity of a semiconductor can be steered over a range of several orders of magnitude. Contrarily to metals, semiconductors conduct better when energy is supplied, whether this energy is of thermal, mechanical, electronical, optical or other origin. This means that semiconductors may absorb energy that they can store temporarily as high conductive carrier concentrations. Of course the reverse is also true: they may pay back energy upon loss of mobility of the carriers. The present research work investigates processes related to these energy variations between energy absorption and energy payback. All of these properties make them very interesting materials for electronic applications.

The science of semiconductors has a long story which has privileged investigation of properties that could deliver new applications. It is of interest to take a brief historical tour.

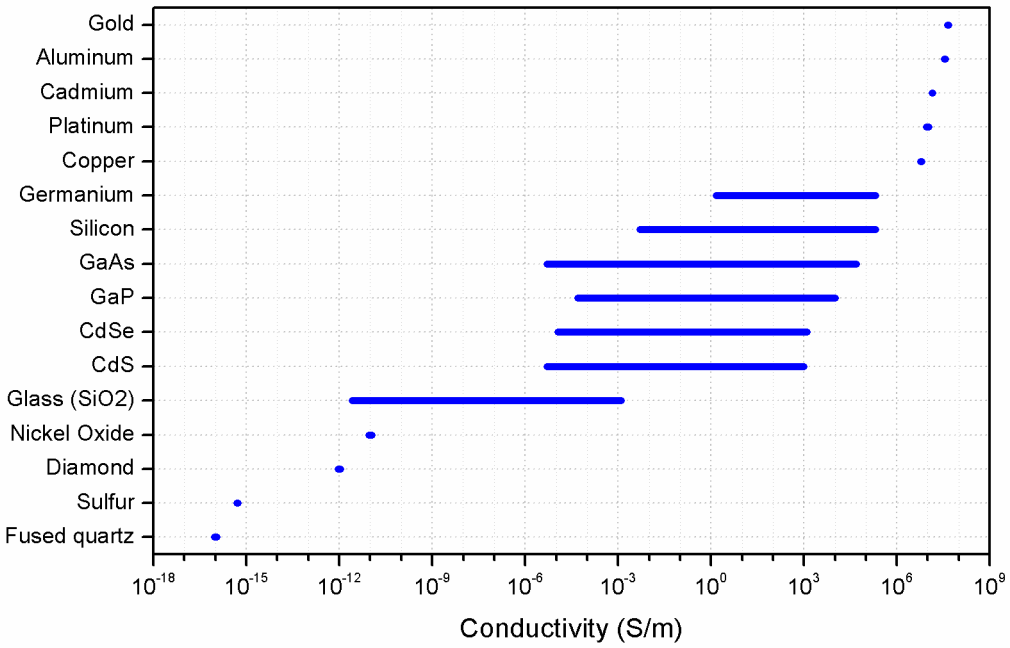

Figure 1.1.: Comparison of electrical conductivities for different metals, semiconductors and insulators. Values are rough estimates collected from literature.

1.3. Historical background

In solid state physics, semiconductors take a unique place. Historically, when first investigating electrical conduction, scientists divided matter in two species: conductors and isolators. Intermediate materials took a secondary place and attracted much less attention in the 19th century context of harnessing the newly discovered applications of electromagnetism. The study of conventional metallic conductors overshadowed the interest in semiconductors. Electrical conductivity benefited from important financial investment during the 19th century industrial progresses, in order to optimize the transport of electric energy and signals over long distances. Since then, the situation has changed. In our microelectronics and nanoelectronics era, semiconductors take a foreground position in solid state physics.

1.3.1. Thermoconductive and photoconductive effects

Since the pioneering experiments of Sir Humphrey Davy around 1810, it was paradigmatically admitted that heating a material lowered its conduction. When Faraday discovered in 1833 that heat acts exactly the opposite way on silver sulphide, it was not without surprise that he reported "*I have lately met with an extraordinary*

case... the conducting power rose rapidly with the heat" [14]. From that point on, discoveries and investigation of semiconductor effects unrolled slowly [15, 16]. Hittorf systematically studied the temperature dependence of different semiconductors and extended the list to copper sulfide, cadmium sulfide, manganese sulfide, antimony sulfide and selenium. He published his results in 1851. All these solids show increased conductivity upon temperature increase [17, 18].

In 1839, Alexandre-Edmond Becquerel discovered another interesting effect. In one of his experiments, sunlight shone upon silver chloride electrodes at the end of platinum wires bathed in a nitric acid electrolyte. He then noticed that a permanent current was flowing through the wires [19], a manifestation of photoconductivity.

This photoconductive effect was much later rediscovered by Willoughby Smith's assistant Joseph May who tested the conductivity of selenium in telegraph cables. In the early 1870s, Smith needed to incorporate portions of poorly conducting material in the transatlantic submarine cables, in order to supervise the quality of the signal. Selenium was tested at an Irish cable station by May and, much to his surprise, he noticed that the conductivity increased when light shone on it [20]. Even dim light of our selenial satellite sufficed to induce a noticeable change in conductivity. Selenium's denomination seemed to be well chosen. This discovery was rapidly incorporated in various devices by commercially driven inventors.

As soon as 1875, Werner von Siemens produced selenium-based photometers [21], which is still the dominant technology for photometers. Alexander Graham Bell, in 1878, incorporated selenium in receiver cells of his photophone which served to transmit sound via optical way. Sound was modulated into a light signal and the selenium receiver demodulated the light into modulated resistivity [22]. William Grylls Adams and his student Richard Evans Day discovered that shining light on selenium could also generate a small electric current without applying any voltage [23]. Further on, in 1883, Charles Fritts designed the first fully operating photovoltaic cell, with an efficiency of 1%, sandwiching selenium between a metallic substrate and a gold sheet [24, 25].

1.3.2. Current rectification

In the meantime, Carl Ferdinand Braun discovered that devices with metal/metal-sulphide interfaces showed direction-depending resistivity, a behaviour departing from Ohm's law paradigm. The sulphides he investigated were chalcopyrite ($CuFeS_2$), pyrite (FeS_2), galena (PbS) and fahlore (copper sulphide) [26]. The same year, Arthur Schuster made similar observations on screwed copper circuitries [27]. The contact points probably got oxidized, with the consequence that current rectification occurred through the copper oxide. Besides, both Willoughby Smith and Charles Fritts also observed rectification in their investigation of photoconductive effects on selenium. The first current rectifiers, which would evolve into our present day

diodes, were born. Thanks to the ingenious contributions of radio pioneers like Jagadish Bose and Greenleaf Pickard, they found application in the first wireless radio receivers: the cat's whisker detectors.

Unfortunately, uncontrolled impurities and fragile assembly of the cat whiskers made these early solid state semiconductor devices much less reliable than vacuum-tube electronic devices. Therefore, technical developments on semiconductor devices, like Julius Lilienfeld's 1926-patented field-effect transistor [28], got very little attention.

It was only after World War II, that the full potential of solid state amplifiers could be unraveled with the technology driven researchers at Bell Labs. Their goal was to replace large energy consuming vacuum tube devices with smaller solid state devices. This yielded Bardeen and Brattain's point junction transistor, theorized by Shockley, which is the key component of nowadays active electronic devices.

1.3.3. Luminescence

Luminescence, the physical property of emitting light from a "cold" state, *i.e.* at room temperature, has a long history. Already in the Middle Ages some solids or liquids were described as phosphorescent after having been submitted to light, *i.e.* from $\varphi\omega\varsigma$ = light and $\varphi o\rho\varepsilon\iota\nu$ = to bear, "bearing light" [29]. Alexandre-Edmond Becquerel and George Gabriel Stokes were its most prominent investigators in the 19th century. Becquerel designed an ingenious rotating wheel setup that could measure phosphorescence lifetimes down to 0.1 ms. This timescale became a popular distinction between fluorescence, with shorter lifetimes, and phosphorescence, with longer lifetimes. In fact, Francis Perrin later gave a physically better definition: fluorescence occurs when the emission originates directly from the excited state, while phosphorescence occurs through an intermediate state. Stokes discovered that the wavelength of emission seemed to be always longer than the wavelength of the absorbed light, resulting in a so-called Stokes shift. Some exceptions were later discovered for some cases: an anti-Stokes shift can occur.

Théodore Sidot, a collaborator of Becquerel and chemical preparator at the Lycée Charlemagne in Paris, seemed to be the first to discover photoluminescence for a semiconductor, after he synthesized a crystalline zinc sulfide in 1866 [30].

During investigations on current rectification with cat's whiskers, Henry Joseph Round discovered in 1907 that carborundum (SiC) could glow with "yellow light green, orange or blue" colors, but he did not proceed with further study of this electroluminescence effect [31]. In 1922, Oleg Losev, a radio research technician in the Soviet Union, rediscovered the luminescence of carborundum, and succeeded to engineer the first Light Emitting Diode (LED) [32], some 35 years before Nick Holonyak and Sam Bevacqua's celebrated 1962 gallium arsenide phosphide LED [33].

1.3.4. The semiconductor era and down-sizing to the nano

With the use of semiconductors for commercial purposes, its technological development got into an accelerated pace. The number of scientific contributors grew exponentially. Germanium replaced other semiconductors. Independently, in 1952, Heinrich Welker, in Germany, and Nina Goryunova, in the Soviet Union under supervision of her mentor Anatoli Regel, discovered new binary semiconducting III-V and II-VI compounds. The effects of doping and heterostructures were better understood, miniaturization and cost-effective design of semiconductor devices entered in a commercial race, yielding the current familiar electronic consumer goods. For a detailed review of this progress, the reader is referred to different publications [34, 35, 36].

Onwards from the 1970s, a new domain emerged thanks to improving technologies: solid state physics at nanometric scales. In 1961, Richard Feynman foresaw this scientific and technological revolution in a renown lecture "There's plenty of room at the bottom", with numerous predictions for extremely tiny devices and machines [37]. Between molecular and atomic physics at the bottom side and conventional classical physics at the top side, there exists a wide gap at nanometric scales which could be exploited to the benefit of all sciences. Ultimately, Feynman was *"not afraid to consider the final question as to whether, ultimately - in the great future - we can arrange the atoms the way we want; the very atoms, all the way down!*" At present day, with our nano-sized materials engineering technology, this is becoming reality, within the limits of quantum rules. But before we consider this quantum confinement range, let us take a short theoretical tour.

1.4. Theory of semiconductors

1.4.1. Solid state physics

For pre-quantum physicists, it was impossible to understand the properties and behaviour of semiconductors.

Max Strutt was the first to resolve the Schrödinger equation of a particle in a crystal with a periodical potential, in his case a sinusoidal potential. Forbidden gaps occurred between continuous bands [38]. This idea was further developed by Bloch and several other physicists [39], giving rise to band theory. In any crystalline structure, the electrons are constrained to a discontinuous energy spectrum, thermodynamically filling bands of increasing energy.

But understanding the full dynamics of electrons in a semiconductor wasn't that easy. On September 29, 1931, Wolfgang Pauli wrote in a letter to Rudolph Peierls: *One should not work on semiconductors, it is a filthy mess; who knows if semiconductors exist after all* [40]. Two days later, the Royal Society published a paper by

Alan Herries Wilson, who explained how the filling of the energy bands determines the way how charge carriers are conducted in a material. For semiconductors, he introduced the concept of holes, which represent the lacking electrons in the valence band and which has motion, mass and energy of their own [41].

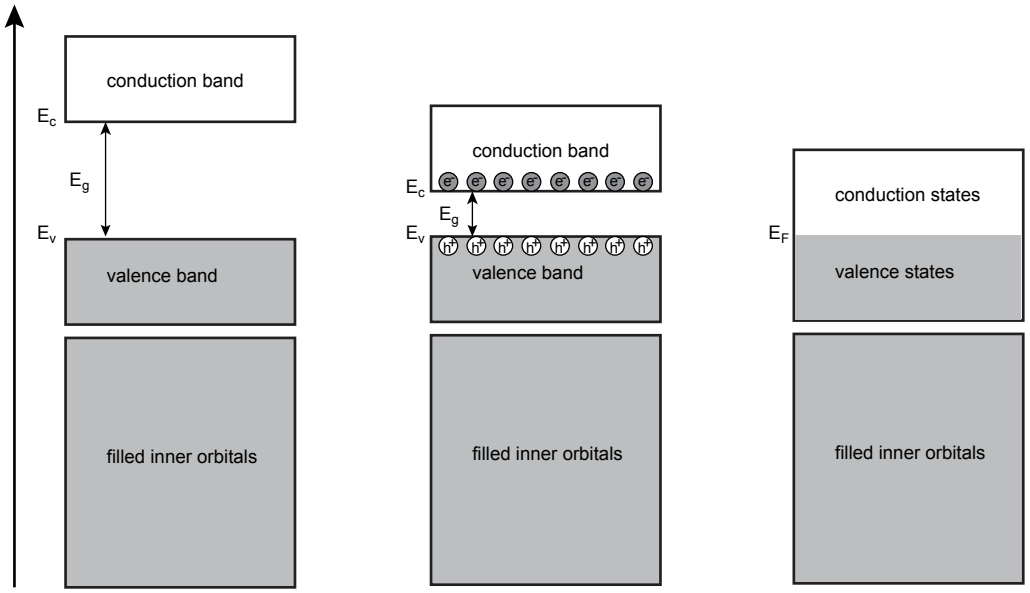

Figure 1.2.: Diagram of energy bands for insulators (left), semiconductors (middle) and metals (right). In insulators, the bandgap E_g is large enough to prevent electrons to bridge the gap from from the top of the valence band E_v to the bottom of the conduction band E_c through ordinary excitations. In semiconductors, energies in the frequency range of visible light may promote electrons to the conduction band and leave holes in the valence band. In metals, the highest energy orbital is partially empty, so that a tiny amount of energy may already induce mobility of the electrons in conduction states.

For semiconductors, roughly said, energy must be supplied to the outer bound atomic electrons – the valence electrons – in order to be raised above a forbidden gap and being allowed to circulate through its crystalline structure under the influence of a voltage, see the diagram in Fig. 1.2. Faraday in 1833 supplied thermal energy, Becquerel in 1839 supplied electromagnetic radiation energy but any form of energy would do, in proper conditions. One could for example also raise the energy of the valence electrons by doping the crystalline structure with impurity atoms. Or one could supply mechanical energy by way of pressure, inducing piezoconductivity.

Once electrons are raised above the bandgap energy, they can circulate through the crystal, while leaving holes of positive charge at the locations they left. These holes play an important role in the electron dynamics of the semiconductor. The

holes can migrate and attract the conduction electrons, giving Coulomb interacting electron-hole pairs, so called excitons. There is a finite probability that an electron and a hole recombine, paying back the energy they lose. This energy payback can be substantiated by radiative (luminescence photons) or non-radiative (phonons, Auger or electron-electron scattering) decay. The nature of the energy payback depends on the physical environment of the electron-hole pair just before it recombined.

1.4.2. Electron hole excitons

After Alan Herries Wilson explained the specific conductivity properties of semiconductors by electrons and holes populating the energy bands, other theorists worked on the dynamics of the electron-hole pairs in the semiconductor.

Frenkel had been worrying about the fact that the Bloch model of energy gaps did not allow traveling electronic excitation waves without net transfer of charge. As an expedient, he introduced in 1936 the bound electron-hole state for isolators which he called an exciton [42]. Wannier extended this concept to excited electron-hole states where its spatial extension exceeded the unit crystallographic cell, typically in semiconductors [43]. The characteristic size of an exciton may be defined by its effective Bohr radius

$$a_B^* = \frac{\epsilon \hbar^2}{m^* e^2} = \frac{m_0 \epsilon a_B}{m^*} \tag{1.1}$$

where m^* is the reduced effective mass of the electron and hole and a_B the regular Bohr radius for the hydrogen atom [44].

An exciton is an excitation occurring in a patterned crystallographic lattice (or molecule). It is composed of an electron and a hole. The hole is the vacancy left by the excited electron. The electron has negative charge; the hole has positive charge resulting from the net charge (nucleic and electronic) left at the vacant orbital. Therefore, the exciton has a net neutral charge. If the electron is excited below the energy freeing it from the hole, the exciton may travel as a whole through the crystal [45]. To be more precise, an exciton is the name given to a bound system of electrons and equally numbered holes. Generally, one refers to an exciton as being the mono-exciton, an electron-hole pair, while multi-excitons are multiple excitons. We adopt this general denomination of an exciton being a mono-exciton.

The important point is that the material investigated in this research work, semiconductor nanocrystallites, host excitons when excited with electromagnetic radiation in the ultraviolet, visible and near infrared. The mobility of the charge carriers (electrons and holes) is then insufficient to allow unbinding of the electron-hole pair. Excitons are generated through absorption of energy. Excitons may disappear either through recombination of electron and hole, which implies restitution of energy

(emission of photons, thermal dissipation) or through unbinding of the electron-hole pair (because one or both charges gets trapped or lost in the environment).

1.4.3. Creation of exciton

In the ground state, all electrons are localized in the core orbitals around the atomic nuclei or involved in valence bonds extending over a range of two or a few more atomic nuclei. An exciton is created when an electron absorbs enough energy to be delocalized to an orbital that extends over a spatial range larger than the valence bonds [46]. The absorbed energy is supplied by quantum excitations: photons, electrons, phonons ... or a combination of these. The delocalized excitonic orbitals are conduction orbitals for electrons, valence orbitals for holes. An application of an electric field will allow the electrons filling the conduction orbitals to flow across the semiconductor. Of course the amount of absorbed energy must not exceed the energy that would unbind the electron-hole pair (the exciton-binding energy in the case of bulk materials; the ionization energy in the case of quantum confined systems), otherwise independently moving charge carriers are created, which don't form excitons anymore.

In order to probe directly the creation of excitons, one disposes over several techniques. Absorption spectroscopy is the most widely used. In its common setup, radiation is sent on the sample and the transmitted radiation is detected at the end side. The difference between incoming and transmitted radiation gives a measure of the absorbed and scattered radiation. Monochromators can be placed at either side, in order to get information about the wavelength of the absorbed, transmitted or scattered radiation.

Other techniques exist which we did not use in this research work. Pump-probe spectroscopic techniques have the specificity to observe induced absorptions or bleaches. Photothermal spectroscopy takes advantage of the thermal variations induced in the sample by absorption of radiation.

1.4.4. Life and disappearance of the exciton

After being created, the exciton has a story to tell. It lives for a certain time: its lifetime. The lifetime will depend on the environment and energy of the electron and hole. Eventually, if the excitation has enough energy or intensity, one may observe signs of its existence during its life. It can for example affect the creation and lifetime of other excitons, through induced absorption or bleaching. In general, if it is not further excited, it will thermalize to a lower lying energy level, the exciton ground state, where it will remain until it can recombine or unbind.

1.4.4.1. Electron-hole recombination

When an excited electron fills a vacancy, we speak of recombination, even if the vacancy may not be the original vacancy left during the excitation. This electron looses energy and may transmit it to photons (luminescence), to single electrons or holes (Auger recombination) or to vibrations in the crystalline lattice (phonons).

Luminescence The most spectacular mark that testifies of the recombination of an electron and a hole is luminescence, i.e. emitted radiation. Typical luminescence lifetimes are of the order of 1-10 ns. This luminescence was coined by Gabriel Stokes with the name fluorescence, when he described the luminescence on the mineral fluorite [47]. When the luminescence occurs after a notable large time-lapse, it is often called phosphorescence, see sec. 1.3.3 Luminescence.

The loss of energy of the electron is taken over by one or several photons. Between absorbed and emitted radiation, there is generally a shift in energy, which shows evidence of dynamic processes occurring during the lifetime of the exciton. Most commonly, this shift is directed towards lower energy, as observed by Stokes; it is called the Stokes shift. If the shift is directed towards higher energy, one speaks of an anti-Stokes shift, for example through phonon or photon up-conversion.

Auger recombination For semiconductors with high carrier concentration, the recombination energy payback can be given to a third carrier, electron or hole. This process has some similarity with the higher energy inner shell Auger effect. It has been denoted by the same name [48]. When the right circumstances occur, Auger recombination has typically shorter lifetimes and will take priority over luminescent excitonic transitions, especially in nanocrystallites [11], giving rise to intensity fluctuations and blinking.

Thermal dissipation When the electron and hole recombine with thermal energy payback, the energy is dissipated in the lattice.

In case of continuous excitonic excitation, the total rate at which the exciton recombines is given by the sum of the rates of each recombination path:

$$\kappa_{tot} = \kappa_{lum} + \kappa_{Aug} + \kappa_{th} \tag{1.2}$$

The efficiency of each recombination path is given by its ratio with respect to κ_{tot}. The efficiency of the luminescence pathway is often denoted as the quantum efficiency, implicitly the luminescence quantum efficiency.

1.4.4.2. Unbinding of electron-hole pair

An exciton can also disappear when the electron and the hole separate, either through trapping of one of the carriers at a defect or a surface site, or through ionization of the object containing the exciton, or through free carrier transport.

1.5. Quantum confinement

1.5.1. Thin films

In the 1960s, with the advent of solid state lasers and p-n junctions, the trend in semiconductor technology was to investigate thin film heterostructures, in which photons and electrons could be confined. The advantage was that this confinement required lower thresholds and higher outputs for solid state lasers [34]. Vapor deposition and molecular beam epitaxy methods to deposit thin films were improved. In 1974, Dingle *et al.* clearly demonstrated quantum confinement effects for a GaAs quantum well sandwiched between two GaAs-AlGaAs layers [49]. The absorption energies shifted to higher energies upon confinement.

In 1982, Bastard and colleagues modelized the thickness dependence of exciton energies in epitaxially grown thin films [50].

1.5.2. Colloidal crystals

At about the same time, various groups also observed shifts of the excitonic absorption and emission lines towards higher energies in colloidal nanocrystals.

In Japan, in 1973, Kishishita noticed several characteristic features of the low energy (LE) excitons in CuCl nanocrystallites grown in alkali halides with a Bridgman technique. With respect to bulk CuCl, the nanocrystallites showed a 20 meV blueshift, a larger shift between the absorption and emission lines (the so-called Stokes-shift) and an unbinding of the exciton. He interpreted it as size-dependent effects, due to nanocrystal sizes smaller than the bound exciton [51]. Tsuboi investigated these features in more detail for various sizes (in fact for various annealing times of the CuCl dopants) and concluded : "*... we find that, as the microcrystal size becomes large, two LE bands shift toward lower energy and approach the peak positions of the $Z_{1,2}$ and Z_3 exciton bands of the pure CuCl*" [52]. Itoh and Kirihara continued those investigations by correlating the energy shift of emission spectra with size-selective excitation [53].

Similar findings were reported by Ekimov and colleagues at the Ioffe Institute in the Soviet Union while growing nanocrystals in glass matrices, first for CuCl and then for CdS [54, 55, 56]. The advantage of their method was a better size control,

henceforth sharper transitions and better experimental determination of the energy-size dependence. This in turn motivated the first theoretical treatments by Efros and Efros [57] which have set the pace for all further theory on quantum size effects in colloidal nanocrystals. We will review this part in more detail in the next section.

At about the same time, while growing ZnS and CdS shells on silicon dioxide nanocrystallites, Henglein and co-workers noticed energy shifts in the fluorescent transitions depending on the age of the sample or degree of agglomeration [58, 59].

In 1983, in the United States, Louis Brus gave a higher visibility to these colloidal quantum confinement effects and its theoretical predictions, essentially on the hand of CdS nanocrystallites in liquid colloidal solutions [60]. Precise comparison between experiment and theory however remained wanting, because the synthesized nanocrystals had a high size polydispersity. With the improvement of synthesis methods, Murray *et al.* were able to synthesize TOPO-capped CdS, CdSe and CdTe nanocrystals with polydispersity as low as root mean square 5% [61]. These high-quality samples afforded Norris *et al.* to assign as much as ten CdSe photoluminescence excitation features to effective mass modelized transitions [62]. In 1998, Banin *et al.* repeated this assignment for the lower band-gap material InAs [63].

Since these pioneering experiments, numerous improvements have been made to enhance luminescence (quantum-yield) by capping the nanocrystals with an inorganic shell that isolates the exciton from surface trapping and subsequent non-radiative recombinations [64]. Shape-dependent properties were also explored thanks to a large variety of different shapes, nanorods, nanowires, nanocubes, nanoribbons, nanoplatelets, nanobelts... [65, 66, 67, 68]. Self-assembly of these nanocrystals in ordered superstructures and super-lattices also emerged as an important field of investigation [69, 70].

1.6. Theory of semiconductor nanocrystals

In order to investigate the excitonic transitions, the natural way involves solving the time-independent Schrödinger equation and determining standing wave solutions with energy eigenvalues as a function of the size of the nanocrystal. The whole procedure consists in using an appropriate eigenfunction basis of Bloch wavefunctions and formulating a correct Hamiltonian.

In bulk materials, the electron-hole pair is treated as a two-particle system in a crystalline dielectric environment with infinite dimensions. In reciprocal space, the electron and hole wavevectors $\boldsymbol{k_e}$ and $\boldsymbol{k_h}$ are then practically free to take a continuous range of values, which results in a continuous absorption band. In the case of confined excitons, the most commonly used theoretical approach is a top-down approach which consists in thinking of the dielectric environment as limited by the surface. The surface is then modeled by potential barriers. As this reduces considerably the number of allowed wavevectors, quantization of the energy spectrum occurs,

like in atoms. Quantum confined semiconductor systems were therefore coined as artificial atoms [71].

We will now give a brief introduction to the effective mass theory for excitons in semiconductor nanocrystallites. We do not pretend exhaustivity, but rather give some entry points for theoretical approaches.

1.6.1. Particle confined in a sphere: envelope function

Theoretical treatments of quantum confined systems started with the modeling of electronic transitions of semiconductor thin films [72, 49], *i.e.* a one-dimensional theoretical treatment.

For the three-dimensional case, pertaining to nearly spherical quantum dots, the theoretical modeling of colloidal nanocrystallites starts with a spherical potential well. In such a nanocrystallite, the electron-hole system can be thought of two interacting charges attracted towards the center of the spherical potential. The earliest models are inspired by analogical treatments for the helium atom, which also consists of two charges in the potential well of the helium nucleus.

The first step was taken by Efros and Efros who, in 1982, published a model where the quantum dot is assumed to be spherical with radius a and with dielectric constant ϵ. Upon creation of an exciton, the electron and hole will be submitted to two potentials: the confinement potential and the Coulomb potential [57]. They respectively have effective masses m_e^* and m_h^*. Depending on the relative strength of confinement and Coulomb potentials, different confinement regimes are specified. It is convenient to consider the exciton Bohr radius defined in Equation 1.1, which sets a delimiter to the different confinement regimes. One considers the following confinement regimes: strong confinement ($a \ll a_B$), intermediate confinement ($a \sim a_B$) and weak confinement ($a \gg a_B$) [73].

Energy term of the potential well If the size of the potential well is smaller than the Bohr diameter of the combined electron and hole, *i.e.* in the regime of strong confinement, the Coulomb electron-hole interaction can be neglected and the problem then consists in solving the radial Schrödinger equation in a spherical well [74]:

$$\frac{1}{r}\frac{d^2}{dr^2}(r\psi) = -k^2\psi \tag{1.3}$$

Its solutions are the wavefunctions:

$$\psi_{klm}(r,\theta,\phi) = R_{kl}(r)Y_{lm}(\theta,\phi) \tag{1.4}$$

where Y_{lm} are the spherical harmonics corresponding to the angular momentum orbitals and respective projections l and m and $R_{kl} = 2kj_l(kr)$ are the spherical Bessel functions of half-integral order. The wavefunction must be zero at the surface of the dot $r{=}a$. For the first zero of the Bessel function, we have $k = \pi/a$. Energy and wavevector are related through the kinetic quantum energy definition $E = \hbar^2k^2/2m^*$. In the parabolic approximation, the size-dependence of the confinement energy for the first transition is therefore given by:

$$E = \frac{(\pi\hbar)^2}{2m^*a^2} \tag{1.5}$$

In the weak confinement regime, the distance between the electron and the hole is essentially determined by the Coulomb interaction.

In the idealized case the confining potential is assumed to be infinite at the nanocrystal boundary. Some theoretical treatments include a finite potential, which physically accounts for the effect of capping ligands or a matrix whose dielectric constant is quite different from 1 [75, 76]. Such a finite potential will lower the energy of the transition.

1.6.2. Coulomb interaction correction and effective Rydberg energy

Efros and Efros' calculations were in first instance applied to CuCl nanocrystallites, whose effective exciton Bohr radius is about 7 Å, smaller than the radius of the investigated crystallites. In this weak confinement regime, the distance between electron and hole could be considered as constant and should therefore predominantly be governed by their coulombic binding, which could be taken as constant in their crystallite size-dependent energy expression. This corroborated with their experimental data showing a $1/a^2$ confinement dependence [56]. Brus devised theoretical expressions applicable to InSb, ZnO and CdS crystallites. Because these materials have much larger excitonic radii than CuCl, he formulated a full size-dependent expression of the confinement energy for the first excitonic transition. This expression, containing a size-dependent Coulomb term, can be resumed as [60, 77, 78]:

$$E = \frac{h^2}{8a^2}\left(\frac{1}{m_e^*} + \frac{1}{m_h^*}\right) - 1.8\frac{e^2}{\epsilon a} + \text{smaller terms} \tag{1.6}$$

with the smaller terms including a solvation term averaging polarization differences.

Kayanuma further adapted Brus' expression by treating the electron hole system in triangular coordinates relatively to the center of the spherically symmetric potential, like Hylleraas' method for the helium atom [79]. He took into account a

constant remnant third energy term which represents the effective Rydberg energy of the exciton without any quantum or coulombic potential constraints, the so-called electron-hole spatial correlation term [80, 81]. His corrected energy-size dependence of the confinement energy of the ground state in the effective mass approximation (EMA) writes [82]:

$$E = \frac{h^2}{8a^2}\left(\frac{1}{m_e^*} + \frac{1}{m_h^*}\right) - 1.786\frac{e^2}{\epsilon a} - 0.248E_{Ry}^* \tag{1.7}$$

E_{Ry}^* is the effective Rydberg energy of the electron hole system, related to the Rydberg energy by replacing the electron's mass by the effective electron and hole masses and taking into account the permittivity of the dielectric, which writes $\left(\frac{1}{m_e^*} + \frac{1}{m_h^*}\right)\epsilon^2 E_{Ry}^* = \frac{1}{m_e}E_{Ry}$. Similar calculations were performed independently by Schmidt and Weller [83] and Nair [84].

Kayanuma's expression is taken as a reference equation for the energy-size dependence of the lowest excited state. It has the advantage of simplicity. However, probing this expression with high-quality experimental data prompted further corrections [85]. These refinements address all the excited states.

1.6.3. Tight-binding approximations

With respect to experiment, EMA generally gives too high an energy for small crystallites. Bottom up tight-binding calculations, linearly combining the individual atomic orbitals lower this energy and thus are a better approximation in the strong confinement regime. These are applied with success to various systems [86, 87, 88, 89, 90, 91]. The drawback is a complexification of the calculational scheme leading to solutions of the energy size dependence.

1.6.4. Valence band degeneracy

So far we have considered the energy levels in the quantum dot as resulting from the difference in energy between two bands taken at the allowed wavevectors $\boldsymbol{k}$. However, in reality, the levels related to a wavevector are degenerate. The excited electron and hole each have multi-fold degenerate levels dependent on their spin and orbital angular momentum. Interactions between the different magnetic momenta and/or the electromagnetic fields in the quantum dot lift this degeneracy, resulting in multiple peaks and inhomogeneous broadening.

Spin-orbit coupling of the hole in the valence band results in three degenerate levels: heavy hole, light hole and split off band, which account for three clear excitonic transitions in the absorption spectra of quantum dots and nanoplatelets. Structural

anisotropy in the wurtzite lattice will further separate the heavy and light hole bands. For detailed description of these effects, we refer to the literature [92, 93, 94, 95, 96, 97].

1.6.5. Electron hole exchange interaction

A fundamental quantum principle is the Pauli exclusion principle, which states that no two identical particles can occupy the same state. As the excited electron and hole are not in the same orbital, the energy of this interaction in bulk is negligible, of the order of 0.1 meV in CdSe nanocrystallites. However, in strong confinement regime, the electron and hole wavefunctions have a large overlap and the interband terms in the exchange Hamiltonian therefore increase and can be of the order of a few tens of meV [98, 99].

1.6.6. k.p perturbation and Kane model

Another way to determine the energy dispersion relation of the valence and conduction bands is to write the kinetic energy term $\hbar k^2/2m^*$ of the Hamiltonian as a term in $k.p$. Near $k = 0$, this term can then be treated as a perturbation. The dispersion of the energy bands then appear as couplings between the different bands. We refer to Ref. [100] for details.

Various optimizations, first proposed by Kane [101], Luttinger and Kohn [102], and Pidgeon and Brown [103], resolve non-parabolicities and splitting of degenerate levels of the energy bands. These methods are widely used for refinements of the effective mass approach for semiconductor nanocrystallites [97, 104, 73].

1.6.7. Alternative approaches

Numerous alternative approaches have been developed. Instead of implementing periodical potentials in the effective mass approximation, as a correction to the overall envelope function, another method is to set up the resultant potential starting from individual potentials, combining them linearly as a linear combination of atomic orbitals [105]. This bottom-up approach may give satisfactory results for the size dependence of the CdSe excitonic transitions, for example when the Coulomb interaction is corrected with a size-dependent dielectric constant [106]. Other methods are the design of effective bond orbitals, empirical pseudo-potentials or bond deficiencies which result in close predictions of the experimental features due to the specific band structure of nanocrystallites [107, 76, 108, 109].

1.7. Experimental setups

This research work builds on the presented technological and theoretical developments. Before presenting the work on chemical synthesis and physical characterization of colloidal quantum dots, we will give a brief presentation of the used experimental facilities.

In this doctoral research work, we benefited from various experimental facilities for the characterization of the nanocrystallites. The nanocrystallites are synthesized in the chemistry laboratory. Some rapid standard spectrometry procedures are used to control the synthesis of the nanocrystallites. These involve the recording of absorption, luminescence and excitation spectra. After the synthesis, one can also control the fluorescence of single nanocrystallites with the help of epifluorescence microscopy. An extension of the epifluorescence microscope is the confocal time-resolved microscope which affords to record single object's time traces upon excitation. These time-resolved measurements give information on the statistics of the excitonic recombinations. This confocal microscope has been extended with a grating spectrometer.

Electronic imaging of the nanocrystals can be done with transmission electron microscopy. In the context of the TEM-confocal microscopy colocalisation project, we have collaborated with Zackaria Mahfoud from the LPS in Orsay, which hosts a cathodoluminescence setup.

Structural information about nanocrystals dispersed on a substrate is obtained with X-ray diffraction.

Ensemble measurement of sizes of nanocrystallites can be obtained by small angle X-ray scattering in collaboration with Benjamin Abécassis from the LPS in Orsay.

1.7.1. Spectroscopy

The standard spectrometers are located in the chemical rooms.

1.7.1.1. Absorption spectroscopy

Absorption spectra of the QD samples were obtained with a Varian Cary 5E double-beam scanning spectrophotometer. The sample is placed on the path of a beam whose wavelength is scanned. The photometer measures the transmitted intensity and deduces the absorbance and diffusion of the sample comparing it with a neutral baseline. At low nanocrystal concentrations, diffusion can be subtracted from the absorbance. The wavelength of the first excitonic transition is characteristic of the size of the nanocrystal. The width of the peaks gives a good measure of its polydispersity in size or shape. The relative position of the different excitonic peaks are characteristic of their crystalline structure [12].

1.7.1.2. Photoluminescence spectroscopy

Photoluminescence spectra of the samples were obtained with a FluoroMax-3 Horiba Jobin Yvon analytical spectrofluorometer or with a Edinburgh Instruments FSP920 spectrometer controlled with the F900 software package.

Roughly the spectra could be obtained in two scanning modes.

1. Keeping a constant excitation window, the emission window is scanned and one obtains emission spectra of the nanocrystals in the sample. This is the photoluminescence mode.

2. Keeping a constant emission window, the excitation window is scanned and one obtains photoluminescence excitation (PLE) spectra. This is the photoluminescence excitation mode.

The Edinburgh Instruments FSP920 spectrometer may also record time-resolved luminescence decays.

1.7.2. Epifluorescence microscopy

Epifluorescence experiments have been performed with an Olympus IX71 inverted microscope with CCD camera (Roper 512b). The excitation light is provided by a mercury illuminator U-LH100HG.

A cryostatic Oxford Instruments sample holder can be installed at working distance from the microscope objective. It affords cooling down and warming up of the observed quantum dots in a range from 4 K to 500 K.

1.7.3. Time-resolved confocal microscopy and spectroscopy

Confocal microscopy has been performed with the MicroTime 200 fluorescence lifetime scanning microscopy (FLSM) setup as add-on to the epifluorescence microscope. Its description is given in chapter 3 dedicated to the physical characterization.

1.7.4. TEM, HRTEM

Transmission electron microscopy (TEM) and high-resolution TEM (HRTEM) imaging has been performed on the JEOL 2010 at 200kV of the ESPCI. This TEM is equipped with a field emission gun. Typical electron beam current values are of the order of 160µA.

1.7.5. Cathodoluminescence

Cathodoluminescence experiments in parallel with the confocal microscopy experiments have been performed on a Vacuum Generators HB-501 scanning transmission electron microscope (STEM) at LPS-Orsay by Zackaria Mahfoud of the team of Mathieu Kociak. Details are given in sec. 3.3.3.3.

1.7.6. X-Ray diffraction

X-Ray diffraction experiments have been performed on the Philips X'Pert Diffractometer with Cu K_α X-ray source, at ESPCI.

1.7.7. SAXS

Small angle X-ray scattering (SAXS) experiments on the CdSe cores have been carried out by Benjamin Abécassis at the SWING beamline of the SOLEIL Synchrotron at Saint-Aubin. The nanocrystals were dispersed in an hexane solution and flame-sealed in glass capillaries. Measurements were performed using Measurements were carried out using a fixed energy of 12 keV and two sample-to-detector positions (1.07 and 6.56 m). The typical accessible range of scattering vector modulus $\mathbf{q}$ was 0.02-10 /nm ($\mathbf{q} = 4\pi \sin\vartheta/\lambda$, where 2ϑ is the scattering angle and $\lambda = 1.033$ Å the wavelength). Scattering patterns were recorded on an AVIEX 170170 CCD camera formed by four detectors and radially averaged.

2. Synthesis of CdSe and CdSe/CdS semiconductor nanocrystals

It is easy for a chemist to write an equation for a desired reaction, but this does not mean that the reaction will actually take place.

William F. Giauque

For the purpose of characterizing quantum dots spectroscopically, we began to prepare them by colloidal synthesis, firstly CdSe cores with narrow size distribution, secondly CdS shells around the cores. Synthesis has been performed using the facilities of the two chemistry rooms of the laboratory: fume hood with vacuum and argon flow circuitry, absorption and photoluminescence spectrometers (described in sec. 1.7.1).

During the synthesis work, we have used a synthesis protocol developed by Yang *et al.* for the zincblende CdSe cores [110] completed by a continuous drop by drop injection protocol in order to grow CdSe or CdS shell monolayers on the CdSe cores. The injection protocol was developed by Benoit Mahler [12] and further refined by Clémentine Javaux [13]. We have adapted details in concentrations, temperature and ramping speed, aiming to improve the luminescence properties of the larger core/shell nanocrystals. All of the syntheses have been performed after degassing below 0.5 mb and with continuous argon flow. The colloidal solutions were warmed up with a heating mantle with control loop feedback, in a three-neck flask of 100 ml, see Fig. 2.2. Octadecene was used as non-coordinating solvent.

2.1. Dynamics of synthesis

The principle of nanocrystal colloidal synthesis is to oversaturate a colloidal solution with reactive monomer precursors. Sudden nucleation of little crystalline cores can be activated thermally while ramping up the temperature in a short time, through so called “burst nucleation”, modelized by LaMer and Dinegar [111], see Fig. 2.1.

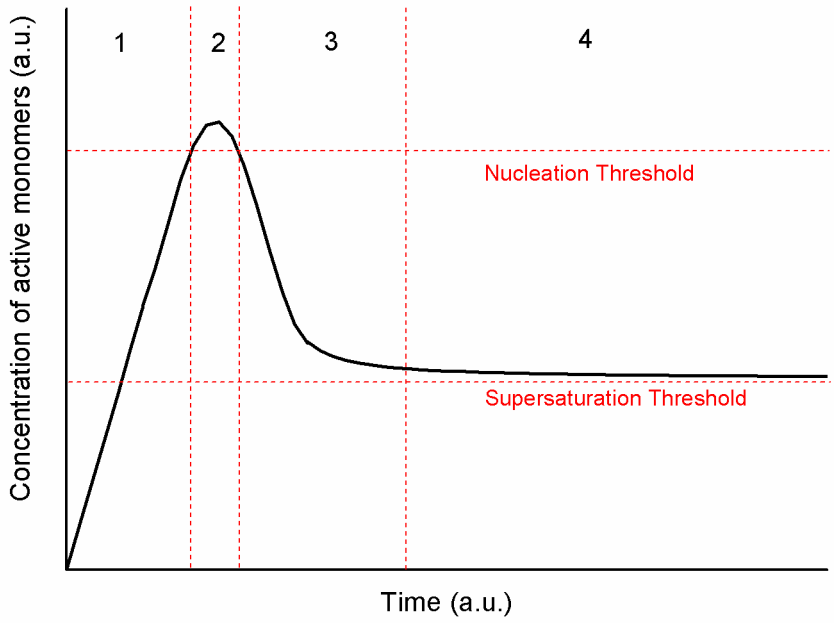

Figure 2.1.: Burst nucleation diagram for colloidal synthesis. The synthesis goes through four steps: 1. Injection or activation of monomers. 2. Nucleation. 3. Growth. 4. Ostwald ripening.

Above a given nucleation threshold concentration, the reactive monomers crystallize in little nuclei. Very rapidly, due to their sudden consumption, the monomer concentration decreases and passes under the nucleation threshold. The nuclei therefore appear only during this short time interval. After this nucleation step, the monomers will continue to feed the growth of nuclei until an equilibrium is attained at the supersaturation threshold. During this growth phase, for high monomer concentrations, it has been shown that there is size focusing, because the smaller nanocrystals grow faster than the larger ones [112]. Finally, there is a phase of ripening (so-called "Ostwald ripening") with interdiffusion of monomers from the smallest nanoparticles towards the largest. The nanocrystal size-dispersion becomes less homogeneous and it is best to stop the synthesis before this ripening takes places.

2.2. Precursors

The cadmium and chalcogenide precursors were synthesized following protocols used in the group [113]. 1-Octadecene (90%, Aldrich), oleylamine (70%, Fluka), oleic acid (90%, Aldrich), sodium myristate (99%, Fluka), cadmium nitrate tetrahydrate

(99.999%, Aldrich), cadmium oxide dihydrate (99.99%, Aldrich), cadmium acetate tetrahydrate (99.99%, Aldrich), selenium powder 100 mesh (99.99%, Aldrich) and sulfur (99.998%, Aldrich) were used as received.

2.2.1. Cadmium

Cadmium myristate For the core synthesis, we used cadmium myristate as a precursor, which we synthesize following a protocol used in the group. We dissolve 1.23 g of cadmium nitrate tetrahydrate (5 mmol) in 40 ml of methanol (easy dissolution). At the same time, 3.13 mg of sodium myristate (13,1 mmol) is dissolved in 250 ml of methanol (1 hour strong stirring after sonication). After complete dissolution, the cadmium nitrate solution is precipitated in the sodium myristate solution, giving a white precipitate. This precipitate is filtered and washed on Buchner (vacuum flask) and dried under vacuum for a night. The white cadmium myristate powder can be stored for months.

Cadmium oleate For the shell growth, we used cadmium d-oleate. We add 10 g of cadmium oxide dihydrate (78 mmol) to 150 ml of oleic acid (476 mmol) in a 250 ml three-neck flask and heat the mix for about 2 hours at 180°C under argon atmosphere and continuous stirring. When the solution becomes transparent and colorless, we cool it down at 80°C and degas it under 0.5 mbar vacuum to let water evaporate. Cadmium oleate is a white wax at room temperature, liquid at about 65°C.

2.2.2. Sulfur and Selenium

The selenium for the cores was supplied as elemental selenium.

For the precursors used for shell growth, the sulfur and selenium were first diluted in octadecene.

For the purpose of obtaining a sulfur-octadecene solution, 167 ml of octadecene is degassed beforehand and heated until 180°C with 533 mg paillettes of elemental sulfur under argon and continuous stirring for about 2 hours. The product is colorless.

For the purpose of obtaining a selenium-octadecene solution, 140 ml of octadecene is degassed in a three neck flask at 70-100°C at 0.5 mbar and heated until 180°C under argon atmosphere. At the same time, 1.185 g of selenium powder is sonicated in a little volume of octadecene (10 ml) and very slowly injected in the warm flask. The temperature can be raised by steps until 210°C to facilitate dissolution. Dissolved in warm octadecene, the selenium octadecene solution becomes yellow. One needs to inject little quantities of selenium in order to avoid accumulation and aggregation of selenium powder which melts at 221°C and which would imply massive blocks of selenium at the bottom of the flask. After injection of all the selenium, the solution

is kept at 210°C during 30 min to ensure complete dissolution of selenium. The resultant solution is transparent and yellow-colored.

2.3. CdSe cores synthesis

2.3.1. General protocol

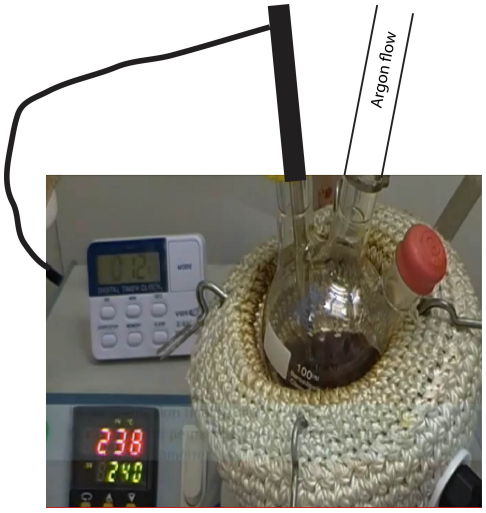

Figure 2.2.: Synthesis of CdSe cores in a three-neck flask with heating mantle

The CdSe cores were synthesized using a protocol inspired from that developed by Yang *et al.* in Cao's group [110]. In a 100 ml three-neck flask with 16 ml of octadecene, we add 174 mg of cadmium myristate (0.307 mmol), 11.8 mg of selenium (0.149 mmol). Under continuous stirring, we degas the solution at 0.5 mb at room temperature for 30 min. After that, we open the argon flow and the solution is heated ramping up at 20°C/s towards 240°C. Around 170°C, the solution changes color, indicating an absorption in the visible light by the nanocrystallites. After reaching the target temperature of 240°C, the solution is kept at that temperature for 10 minutes. The synthesis is then stopped. We let the solution cool down slowly and 0.2 ml of oleic acid is injected in order to assure colloidal stability at ambient temperature. We precipitate the dots twice with methanol or ethanol, depending on their size. The washed precipitate is re-suspended in 10 ml of hexane. The photoluminescence spectrum of these dots shows an emission peak around 575 nm, which corresponds to a diameter of about 3.5 nm.

For the purpose of obtaining smaller quantum dots, we can stop the synthesis and cool down the colloidal solution at any time depending on the desired size of quantum dots.

In order to obtain larger CdSe cores, we can use the product of the previous synthesis, raise the temperature and inject additional cadmium and selenium precursors, following the protocol developed by Mahler and Javaux [12, 13]. We add 2 mL of oleic acid (for faceted QDs) or oleylamine (for spherical QDs) and raise the temperature to 280°C. When the temperature reaches 280°C, we begin drop by drop injection with speed 12 ml/h of a cadmium-selenium stoechiometric mixture with the prepared cadmium oleate and selenium-octadecene precursors, increasing stepwise the temperature until 305°C. At the end of the reaction, we cool down at ambient temperature, collect the end product, precipitate twice in 50 ml ethanol or butanol and dilute dots in 10 ml of hexane. In order to prevent obstruction of the syringe needle by the cadmium oleate during injection, it is best to heat moderately the syringe.

2.3.2. Core size prediction

The CdSe quantum dots obtained through the described synthesis have a relatively homogeneous size dispersion. Their average size may be predicted using different methods.

2.3.2.1. Energy-size relations

In the confinement regime, the energy of its excitonic transitions depends on the size of the nanocrystal. Theoretical models exist but due to the complexity of the physical effects that are taken into account, they generally yield non-analytical expressions.

For CdSe, which is extensively studied, one prefers generally the use of empirical polynomial formulas that express the size as a function of the absorption wavelength [114, 115]. Another possibility is to use inverse polynomial expressions based on tight binding calculations expressing the increase in energy as a function of the size. This was first applied successfully to PbSe quantum wells and colloidal QDs [90], and adapted for CdSe [116, 117]. Another way of expressing the increase in bandgap due to quantum confinement is the use of a fractional exponent [118]. The relations for CdSe QDs are given below.

Yu *et al.* [114] relate the size d and wavelength λ in nm :

$$d = (1.6122\times10^{-9})\lambda^4-(2.6575\times10^{-6})\lambda^3+(1.6242\times10^{-3})\lambda^2-(0.4277)\lambda+41.57 \quad (2.1)$$

Jasieniak *et al.* [115] relate the size d and wavelength λ in nm :

$$d = (1.62974\times10^{-9})\lambda^4-(2.85743\times10^{-6})\lambda^3+(1.8873\times10^{-3})\lambda^2-(0.54736)\lambda+59.60816$$

(2.2)

De Mello Donega and Koole [116] relate the size d in nm and energy and E_g in eV:

$$E_g = 1.858 + \frac{1}{0.22d^2 + 0.008d + 0.373} \tag{2.3}$$

Karel Capek *et al.* [117] relate the size d in nm and energy gap E_g in eV:

$$E_g = 1.74 + \frac{1}{0.22d^2 - 0.36d + 0.89} \tag{2.4}$$

Wang and Seo [118] relate the size d in nm and energy gap E_g in eV:

$$E_g = 1.74 + 2.06/d^{1.25} \tag{2.5}$$

These expressions are plotted in a next section together with the CdSe cores experimental data (see Fig. 2.6). Except for the expression 2.4 of Karel Capek which applies to zincblende CdSe QDs, these expressions apply to wurtzite QDs.

Variations in the size dependence of the transitions occur due to difference in ligands and structure. Therefore, the given expressions should be applied with care, taking into account these differences. The larger dispersion in size in the sample also broadens the full width half maximum of the excitonic peak.

2.3.2.2. Absorbance measurement, extinction coefficient and precursor consumption

Once the nucleation step is over and if there is no secondary nucleation, the precursor monomers are consumed in the growth of the nanocrystal nuclei. Knowing the concentration and the size of the nanocrystals at a given time, we can thus deduce the amount of precursors needed to grow the nuclei by a given amount.

Practically it is however a challenge to determine precisely the concentration of a solution. A widely used method is to deduce it from the absorbance of an aliquot. The aliquot must be diluted in a transparent solvent, in order to limit the diffusion of the quantum dots.

For CdSe QDs, Leatherdale *et al.* established a simple formula linking the molar extinction coefficient ϵ for a probing beam at $\lambda = 350$nm to the radius r of a QD (ϵ in $M^{-1}cm^{-1}$ and r in nm) [119]:

$$\epsilon = 1.438 \times 10^5 \times r^3 \tag{2.6}$$

The Beer-Lambert law links the absorbance A to the concentration [QD] and extinction coefficient of the QDs through the formula:

$$A = [\text{QD}]\epsilon l \tag{2.7}$$

where l is the path length of the probing beam through the sample, in cm. Combining these two equations, the concentration [QD] can be deduced from the average radius r in the CdSe QDs sample and from the absorbance A_{350} at 350 nm:

$$[\text{QD}] = \frac{A_{350}}{r^3} \times 6.954 \times 10^{-6} \tag{2.8}$$

In the used protocols, selenium is the limiting reagent. In the zincblende CdSe QDs, selenium has a density of 4 atoms per unitary cell of volume a^3, where a=0.608nm is the zincblende lattice constant. If all selenium is consumed in the reaction, the size of the nanocrystals is related to the concentration and the crystalline volume taken by the monomers.

When we continue the growth of the nanocrystals through a continuous injection of precursors, we are thus able to predict the final size of the quantum dots knowing the quantity of injected selenium and the concentration of the initial cores. In a solution of volume V, the number of selenium atoms consumed in QDs is:

$$N_{Se} = 4.\frac{4r^3}{3a^3}.[\text{QD}].V \tag{2.9}$$

An extra shell of thickness (R-r) would thus consume an extra number of selenium atoms $N_{Se} = 4.\frac{4(R^3 - r^3)}{3a^3}.[\text{QD}].V$, which relates to the required mass m via Avogadro's number N_A and the molar mass M_{Se} of selenium (79 g/mol) through:

$$m = \frac{N_{Se}}{N_A} M_{Se} \tag{2.10}$$

2.3.3. Characterization

2.3.3.1. Spectra

During a typical synthesis of CdSe cores, as the cores grow in size, the excitonic transitions shift from blue to red. Aliquots are taken at regular points from which

emission and absorption spectra are measured in order to monitor the growth and dispersity in size of the nanocrystals. Fig. 2.3 shows a typical set of normalized emission spectra viewed during the progression of the synthesis. Two great stages can be seen in this progression. Firstly a rapid growth of the QDs until the emission wavelength has reached about 575 nm. This corresponds to the small cores synthesis. Secondly, another redshift of the emission peak occurs due to the growth of the QDs through the drop-by-drop injection.

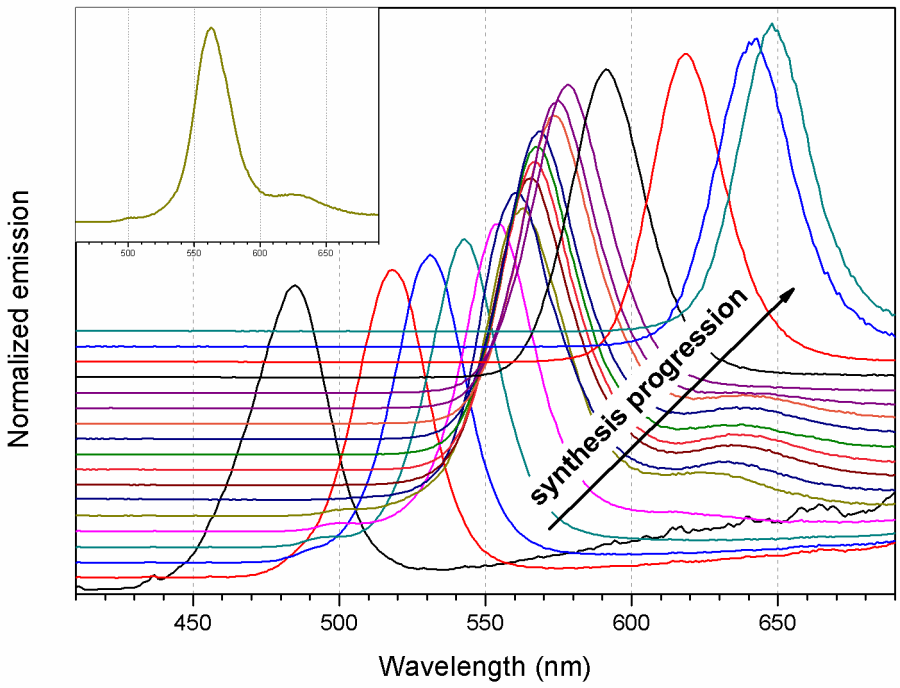

Figure 2.3.: Typical aspect of emission spectra (stacked) during the progression of a CdSe cores synthesis. Inset gives the 6th emission spectrum, showing two secondary peaks at blue and red side.

Different other features can be observed in these spectra.

First of all, the full width at half maximum (FWHM) which varies between 25 - 32 nm depending on the control of the monodispersity in the synthesis (i.e. about 5% in dispersion). This spectral dispersion is a good measure for the dispersion in size of the QDs.

We also observe a wide peak at large wavelengths in the early stages of the synthesis, which disappears at later stages. This peak is related to the detrapping of the exciton from surface sites, so called deep traps [120]. As the size of the CdSe core increases, the proportion of surface trapping sites with respect to volume excitons decreases.

On some of the emission spectra during the small core synthesis, we can also observe a small secondary peak at the blue side, the origin of which is unclear. It may be related to secondary nucleation or to the occurrence of little nanoplatelets. Another secondary peak can be seen at the red side, see the inset of Fig. 2.3 for an example. These peaks will be discussed below on the hand of other characterizations.

Fig. 2.4 shows the absorption spectrum of the fifth aliquot in Fig. 2.3, together with its emission spectrum. CdSe core absorption spectra at room temperature clearly show three excitonic transitions, as well as a Stokes shift of about 10 nm in wavelength, for QDs emitting around 550 nm.

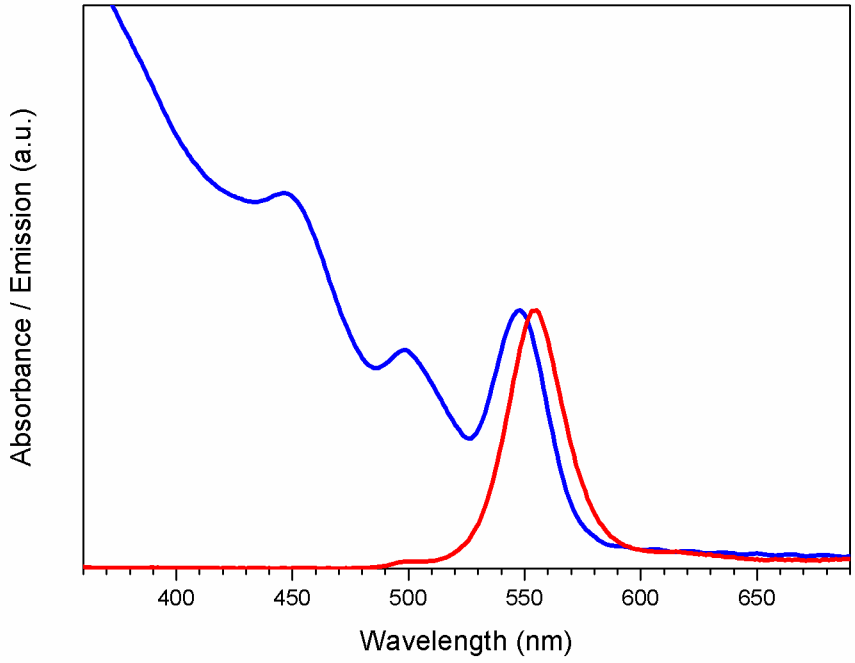

Figure 2.4.: Absorption and emission spectrum of CdSe cores of diameter about 3.2 nm.

Fig. 2.5 gives the time and temperature progression of the excitonic peaks during the synthesis. We see that they all follow the same trend, except the higher energy emission peak which stagnates at 500-510 nm. This stagnation suggests that they are likely related to 4 monolayer CdSe nanoplatelets, which emit at 513 nm when they are fully grown laterally. On TEM images of aliquots with this emission peak, one observes indeed little platelet shaped objects.

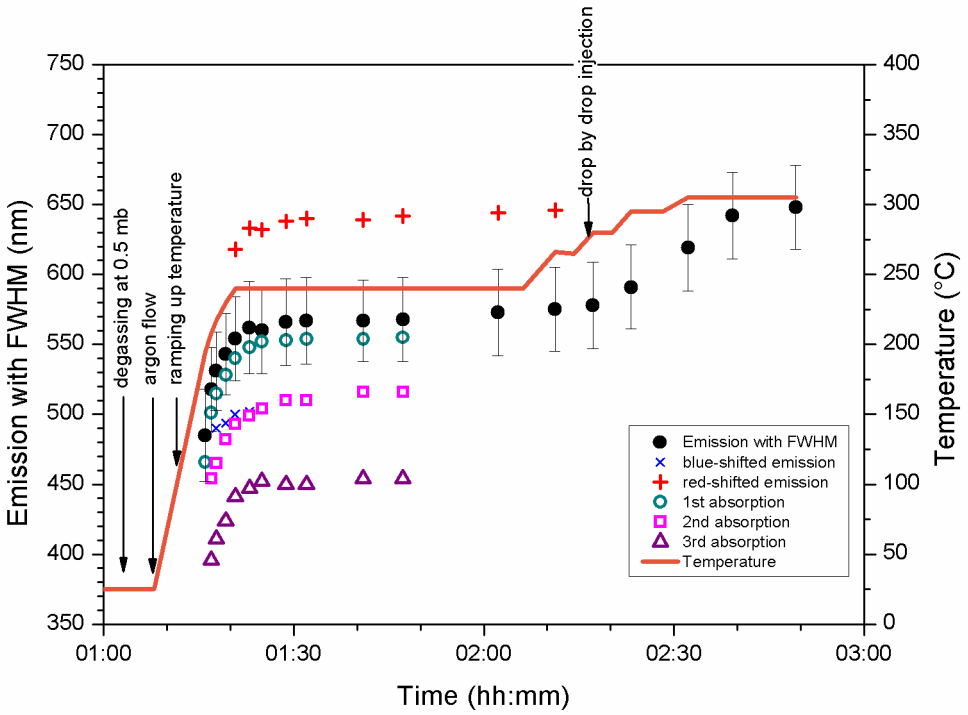

Figure 2.5.: Wavelength of excitonic peaks of CdSe cores viewed with respect to time and temperature progression of a typical core synthesis. The bars relative to the emission peak indicate the extent of the full width half maximum.

During a synthesis, it is also of interest to record the PLE spectra and compare them to the absorption spectra. For samples which have one emission peak (for example homogeneous spherical quantum dots, without secondary nucleation), the photons absorbed over the whole spectrum should equally give luminescence at the emission peak's wavelength. The normalized PLE and absorption spectra should therefore overlap.

2.3.3.2. Size determination

Size determination of the synthesized CdSe cores has been done with TEM. Some sizes have also been cross-checked by Benjamin Abécassis with SAXS. In order to obtain a sizing curve for the CdSe core quantum dots, we determined the room temperature transitions for the quantum dots of different sizes. Details about these determinations are given in the annex sec. A.1.

The sizing curve relating the wavelength of the first excitonic transition of the absorption spectra to the diameter of the QDs is given in Fig. 2.6, together with the plots of the empirical fitting equations 2.1 to 2.5 for the small QD samples. We notice excess in size (diameter) with respect to the fitting formulas of the literature

for the small QD samples which may be due to difference in diameter determination from TEM images. As can be seen in the figure, a remarkable kink in the experimental sizing curve trend of the QDs occurs at a diameter of about 6 nm. Above this size, the QDs follow the sizing curve of zincblende determined by Karel Capek *et al.* [117]. We will discuss the sizing curves in more detail in chapter 4.

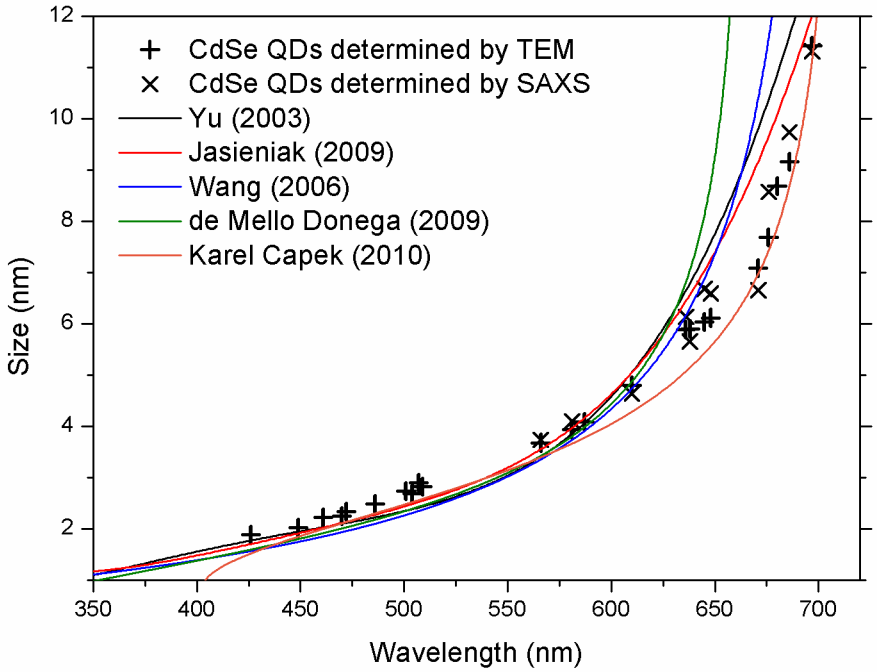

Figure 2.6.: Size-wavelength dependence of the first excitonic transition of the CdSe quantum dots at room temperature obtained from absorption spectra, size as diameter. The fitting expressions 2.1 to 2.5 are plotted in solid lines for comparison.

2.3.3.3. Secondary peak

In order to investigate the origin of the secondary peak mentioned in sec. 2.3.3.1, we have performed syntheses where this peak was enhanced. On TEM imaging, rod-like objects appear, seemingly aggregations of 2 to 5 quantum dots, see Fig. 2.7. These objects appear essentially for high cadmium myristate concentrations. If we inject oleylamine in the solution, the peak shifts towards the primary peak or vanishes, see the emission spectra before and after oleylamine injection Fig. 2.8. It is known that CdSe nanocrystal syntheses yield nanorods for high monomer concentrations and higher temperatures [65, 121].

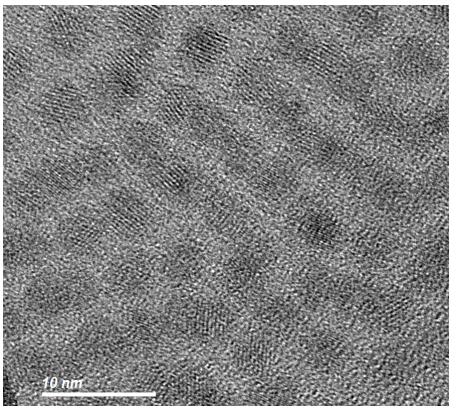

(a) Aggregating quantum dots

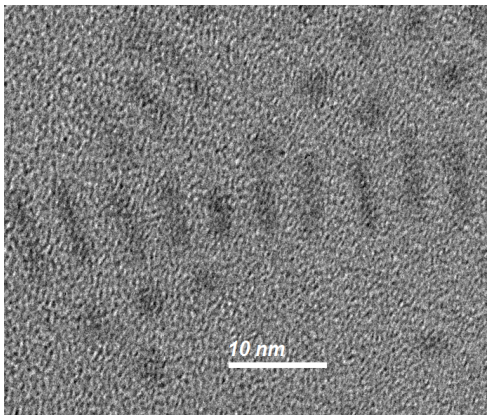

(b) Dots and rods

Figure 2.7.: TEM images of samples with a secondary emission peak at the red side of the primary peak.

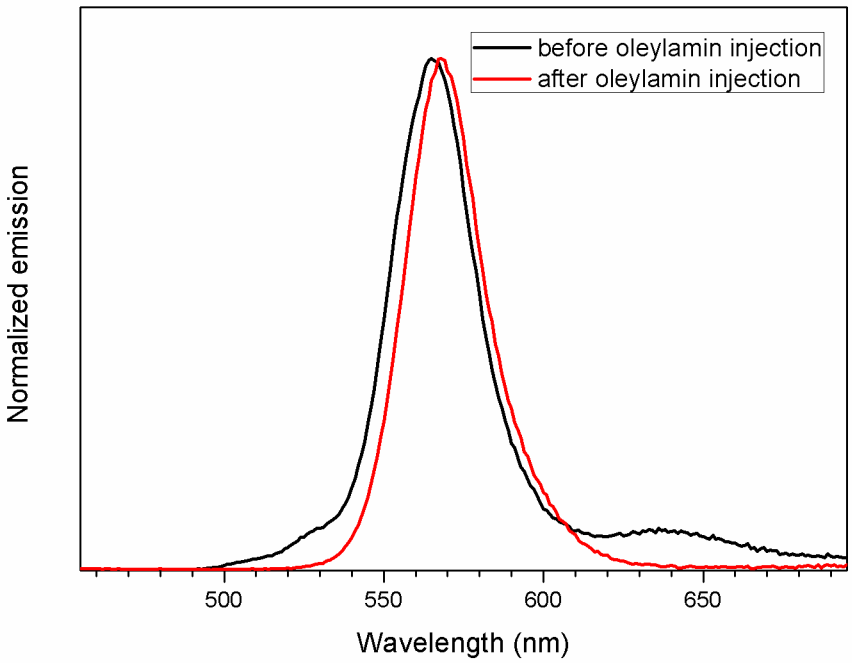

Figure 2.8.: Difference in emission of 3 nm diameter QDs before and after injection of 2 ml of oleylamine

For samples with this secondary peak, the PLE spectra with emission detection at the primary peak follows a trend below the absorption spectrum, see Fig. 2.9, meaning that the excitons of the absorbed photons recombine with emission at other wavelengths. We may notice that the first transition of the PLE spectrum for emission detection at the secondary peak differs sensibly from the first excitonic transition of the primary peak, while the second and third transitions have same wavelength for both PLE spectra. The Stokes shift of 30 nm of the secondary red peak is important with respect to the Stokes shift of QDs emitting at the same wavelength.

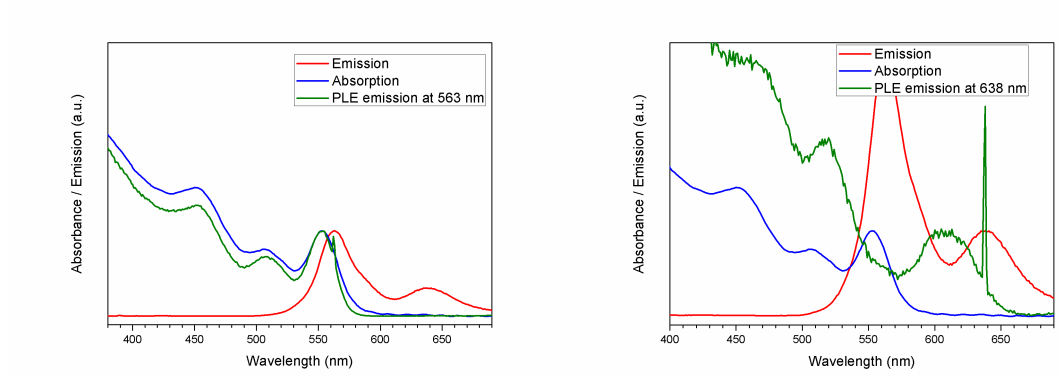

Figure 2.9.: Normalized emission, absorption and PLE spectra for a sample with secondary peak, for emission at 563 nm (left) and emission at 638 nm (right).

The secondary peak's energy dependence upon the primary emission peak will be investigated in more detail in sec. 4.2.3.3.

2.3.3.4. Variations

The general protocol has been varied in order to obtain different shapes and sizes. Lower concentrations and temperatures generally give more faceted QDs (tetrahedra or cubes), while higher concentrations may give rods.

2.4. CdSe/CdS shell coating

2.4.1. General protocol

For the growth of CdS shells, we may use directly the cooled down end product of the core synthesis. We keep one fourth of it in the three-neck flask, degas it for 30 min at 0.5 mbar and heat it up under argon flow at 260°C. We inject 2 ml of oleylamine and keep the solution at 260°C for 20 min. We begin drop by drop injection with syringe pump of a 20 ml cadmium-sulfur mixture with the prepared cadmium oleate (3.5 ml at 0.5M) and sulfur-octadecene (16.5 ml at 0.1M), with speed 2.25 ml/h. After two hours, the temperature is raised to 310°C and the remaining 15,5 ml are injected within an hour. At the end of the reaction, we obtain core-shell QDs with a shell of about 5 nm thickness.

The shell can be grown further. To that purpose, one third of the content is kept in the flask. We raise the temperature to 310°C and inject 20 mL of the same selenium-octadecene/cadmium oleate mixture in 3 hours. At the end of the synthesis, we obtain core-shell QDs with a shell of about 10 nm thickness. We cool down at

ambient temperature, collect the end product, precipitate twice in 50 ml ethanol or butanol and dilute the quantum dots in 10 ml of hexane.

If the last injection is performed at a much slower rate (20 ml in 15 hours in a typical case), we noticed that the luminescence stability of the core-shell QDs was improved. For the reference QDs sample used in all optical-electronical microscopy colocalisation, there is a non-blinking fraction of 95% after 10s (20 ms binning) on statistical measurements at ambient temperature. These results are similar to those obtained by Clémentine Javaux [13], with a very uniform luminescence intensity for all QDs observed under the microscope. This synthesis could however not be reproduced regularly. The reason for this non-reproducibility may be related to variations in precursor and ligand purity.

2.4.2. Core-shell size prediction

For CdS shell prediction on the CdSe cores, the same procedure may be applied as for the growth of CdSe shells, *cf.* sec. 2.3.2.2.

2.4.3. Characterization

2.4.3.1. Spectra

Fig. 2.10 shows the emission and absorption spectra of aliquots taken during the progression of a typical core-shell synthesis.

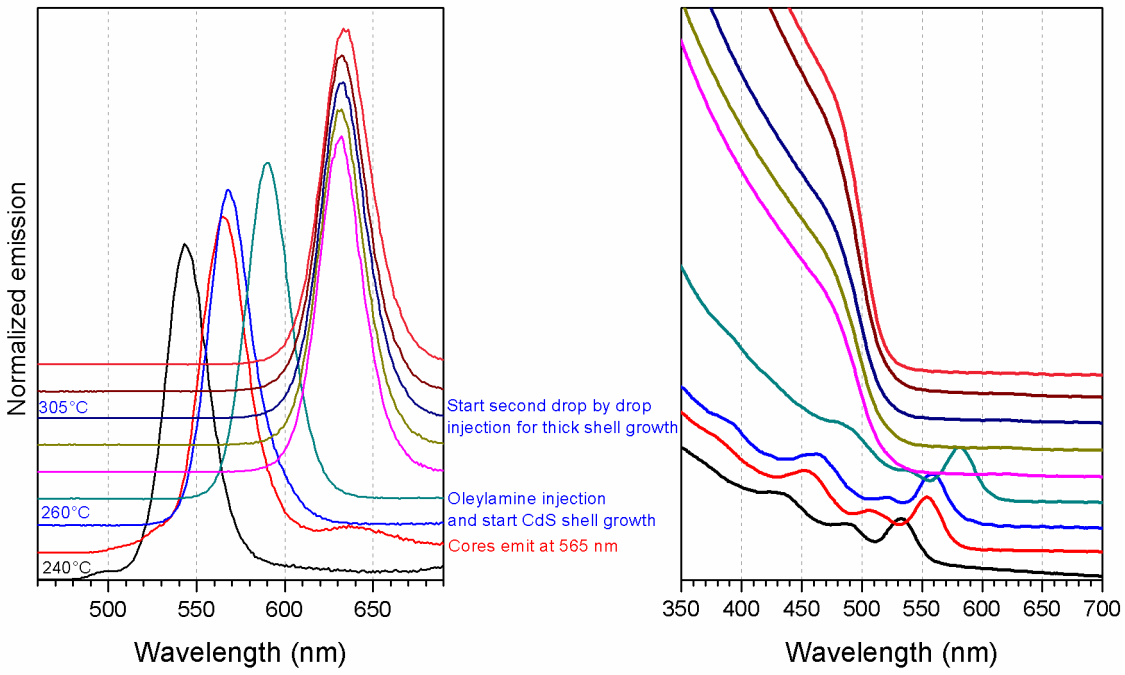

Figure 2.10.: Emission (left) and absorption (right) spectra during a core-shell CdSe/CdS synthesis

With increasing thickness of the CdS shell, the CdSe excitonic features disappear from the absorption spectra and are replaced by the typical CdS absorption onset at about 530 nm which becomes steeper with increasing shell thickness.

With the given protocol, after the first CdS drop by drop injection, the shell thickness is about 5-6 nm, resulting in slightly faceted QDs of diameter 12-16 nm, for cores of diameter 3.5 nm.

After the second CdS injection, the "thick" shell QDs have in majority a bipyramidal shape, with long axis between 22 and 30 nm, see an example in Fig. 2.11a.

2.4.3.2. Polytypism

On TEM images, the thick shell QDs show bipyramidal shapes with contrasting lines perpendicular to the height of the pyramids, see Fig. 2.11a. These differences in contrast suggest variations in the stacking of the planes, with alternating wurtzite and zincblende domains. This seems to be the case even with wurtzite cores [13]. This polytypic growth may be the reason for the non-blinking behaviour of the quantum dots cores, as it decreases the overlap of electron-electron or electron-hole wavefunctions responsible for Auger processes.

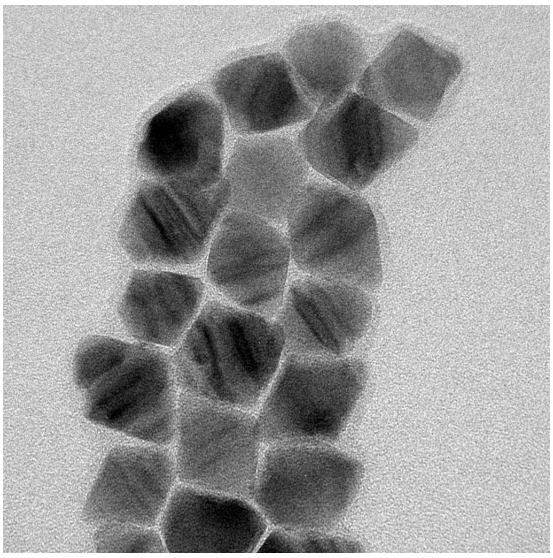

(a) TEM images of CdSe/CdS thick shell QDs, showing polytypic structure (obtained at magnification x120000).

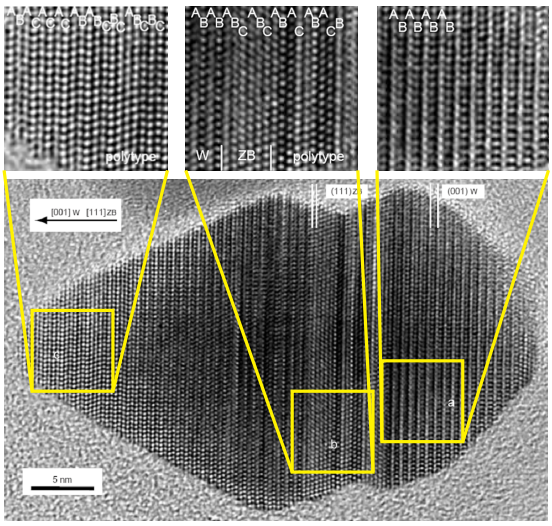

(b) Core-shell dot with wurtzite-zincblende polytypism (obtained at magnification x300000, courtesy of P. Bassoul). From left to right, the magnified areas represent: - a polytypic area, - an area with side by side wurtzite, zincblende and polytypic domains, - a wurtzite domain.

Figure 2.11.: Polytypism in CdSe/CdS core-shell quantum dots

Fig. 2.11b shows a special case of bipyramidal core-shell quantum dot. Two bipyramids seem to have fused. It is possible to distinguish the stacking faults of the planes perpendicular to the long axis (the wurtzite <001> axis, or zincblende <110> axis).

We have alternating ABABAB wurtzite and ABCABC zincblende planes. In some areas, the stacking is highly polytypic. It is suggested that the double hexagonal pyramid has (101)-equivalent wurtzite facets [122].

2.5. CdSe nanoplatelets

2.5.1. General protocol

The group in which was performed this research work is specialized in CdSe nanoplatelets (NPLs), which were discovered by Sandrine Ithurria [123]. These objects are very interesting for theoretical modeling as they can be isolated in samples of NPLs with precisely defined thickness. FWHM of their excitonic peaks (emission and absorption) is about 2% which is exceptional for colloidal nanocrystals.

We have synthesized some CdSe nanoplatelets emitting at 551 nm, using a protocol developed by Mickaël Tessier [124]. In a 100 ml three-neck flask with 14 ml of octadecene, we add 170 mg of cadmium myristate (0.3 mmol). Under continuous stirring, we degas the solution at 0.5 mb at room temperature for 30 min. After that, we open the argon flow and the solution is heated at 250°C. We quickly inject a selenium solution of 12 mg (0.15 mmol) dispersed in 1 ml octadecene. This starts the nucleation of little CdSe seeds. A minute later, we rapidly introduce cadmium acetate tetrahydrate in the flask and we continue the heating for 10 minutes. The solution contains QDs and nanoplatelets which are separated through selective precipitation. The nanoplatelets are dispersed in hexane.

2.5.2. Characterization

2.5.2.1. Spectra

The synthesis can be monitored by taking emission or absorption spectra of aliquots, see Fig. 2.12. After injection of selenium in the hot octadecene/cadmium myristate solution we have a characteristic CdSe QD emission spectrum with FWHM of about 25-30 nm. After the introduction of cadmium acetate, we see that the peak narrows until reaching a FWHM of 8 nm which is typical of room temperature nanoplatelet emission spectra.

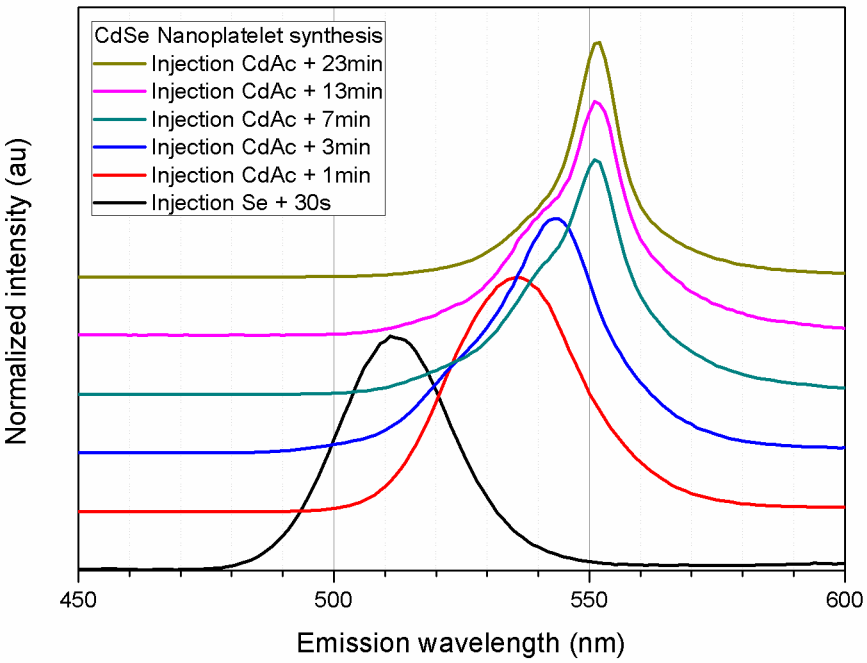

Figure 2.12.: Emission spectra during a 5 monolayer CdSe nanoplatelet synthesis

Of course, we can also monitor the nanoplatelet synthesis with the absorption spectrum. Fig. 2.13 shows the absorption spectrum of a solution of CdSe nanoplatelets together with its emission spectrum. The first excitonic absorption peak has a FWHM similar to the emission peak and the Stokes shift is only 2 nm.

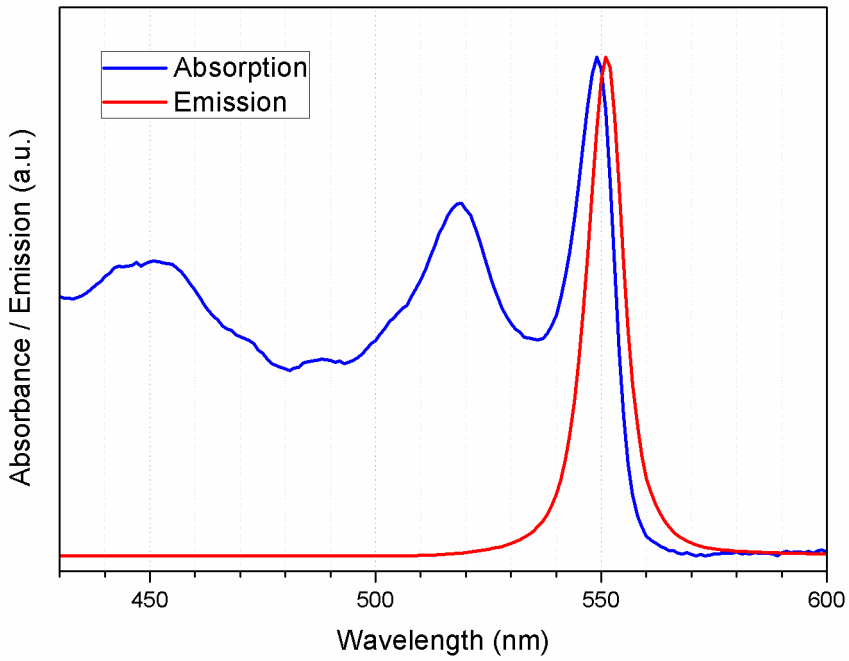

Figure 2.13.: Absorption and emission spectrum of CdSe nanoplatelets.

2.5.2.2. General aspect

The synthesized nanoplatelets emitting at 551 nm have a thickness of 5 monolayers. The above protocol gives nanoplatelets of width about 6-10 nm and length 30 to 40 nm, see Fig. 2.14.

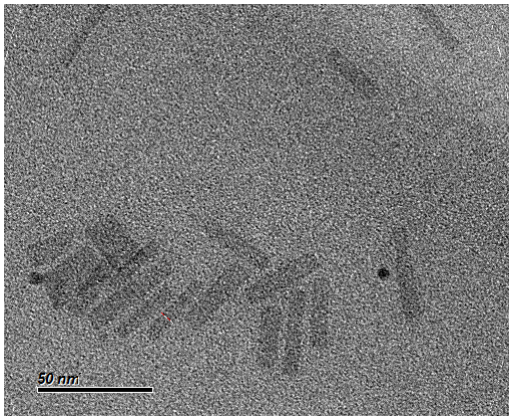

Figure 2.14.: TEM image of nanoplatelets.

2.6. Conclusion

In this research work, we determined the experimental wavelength-size dependence for absorption and emission for CdSe cores for a range extending over the whole strong confinement regime (diameter 2 - 11 nm). These results will be used for modeling of the energy-size dependence in chapter 4. We characterized two secondary emission peaks which show up in the spectra of the used protocol for the CdSe cores. We also hypothesized, on the hand of TEM imaging and synthesis conditions, that they are related to the formation of nanocrystals of different dimensional confinement: nanoplatelets for the peak stagnating at 510 nm and nanorods for the red-shifted peak.

We could reproduce the syntheses of robust quasi non-blinking thick shell CdSe/CdS quantum dots, developed in the group [125, 122]. The luminescence properties of these bipyramidal polytypic core-shell QDs make them ideal objects for optical and TEM colocalisation experiments, which will be described in the next chapter.

3. Time-resolved spectroscopy of semiconductor nanocrystals

An experiment is a question which we ask of Nature, who is always ready to give a correct answer, provided we ask properly, that is, provided we arrange a proper experiment.

Charles V. Boys

3.1. Luminescence decay in ensemble of quantum dots

3.1.1. Experimental setup

Ensemble measurements have been performed with the Edinburgh Instruments FSP-920 spectrometer, described in sec. 1.7.1. A SuperK Extreme EXB-4 supercontinuum white laser source of NKT Photonics has been used for lifetime measurements at room temperature for an ensemble of QDs. Excitation wavelength selection is performed with the SuperK Varia filter module based on linear variable filters. The usable range spreads from 430 to 700 nm. The detection is performed with a Hamamatsu R928-P photomultiplier or with a multi-channel plate detector.

Great care is required in order to compare lifetime measurements with excitations at different wavelengths with a continuum laser. Constant power over the whole spectrum is hard to achieve and needs readjustment with the absorption cross section of the QDs at the given wavelength. For any photoluminescence (PL) experiment, we would prefer constant photon flux.

3.1.2. Results

We have performed series of measurements on solutions of core shell CdSe/CdS QDs at room temperature with the continuum laser at different wavelengths, at constant power, with repetition rate 2 MHz. It appears that the average PL decay lifetime of the QDs is shorter if the excitation is performed at an energy lower

than the absorption onset of the CdS shell (about 2.35 eV, wavelength 530 nm), see the compared fluorescence decay curves in Fig. 3.1 with fitted values for three exponentials in Tab. 3.1. The p_i are expressed as percentages $p_i = a_i\tau_i / \sum a_j\tau_j$, where the a_i are the amplitudes of the fitting exponentials. This shortening of the lifetime at energies lower than the CdS absorption onset is enhanced for thicker shells, i.e. when the proportion of absorbing CdSe per dot is smaller. This suggests that excitons formed in the CdSe core decay more rapidly than those formed in the CdS shell.

	Excitation	τ_1 in ns (with proportion)	τ_2 in ns (with proportion)	τ_3 in ns (with proportion)
"thin" shell CdSe/CdS QDs	460 nm	91 (32%)	37 (62%)	9 (6%)
	500 nm	92 (32%)	37 (63%)	8.5 (5%)
	540 nm	76 (39%)	32 (58%)	5.6 (3%)
"thick" shell CdSe/CdS QDs	460 nm	115 (72%)	32 (25%)	5.8 (3%)
	500 nm	114 (71%)	32 (26%)	5.7 (3%)
	540 nm	92 (76%)	18 (21%)	1.4 (4%)

Table 3.1.: Parameter values for a three exponential fit of fluorescence decay curves of a solution of core-shell CdSe/CdS quantum dots sample, excited at different wavelengths. The proportions p_i are expressed as percentages $p_i = a_i\tau_i / \sum a_j\tau_j$, where the a_i are the amplitudes of the fit exponentials.

This suggestion should be taken with care however. On Fig. 3.1, the decay curves for excitation at 540 nm have a long lifetime slope similar to that for excitation at smaller wavelengths. The shortening of the lifetime may thus be caused by multi-excitons that would occur more frequently in ensemble measurements with excitation in the core [126]. We also remark that the absorption of the QDs is completely different between the different excitation wavelengths.

One can also observe a small narrowing of the emission peak at the higher energy side, which is probably due to spectral size selection.

3.2. Confocal fluorescence spectroscopy

3.2.1. Experimental setup

The idea of fluorescence lifetime scanning microscopy is to direct an excitation laser beam on a single nanoparticle and to record the fluorescence photons pertaining to that single nanoparticle. This can be done through confocal optics, where the laser beam is directed through the objective onto the sample and the emission photons follow the same optical path back through the objective. Because the excitation energy is not the same as the luminescence energy, the emission photons can be

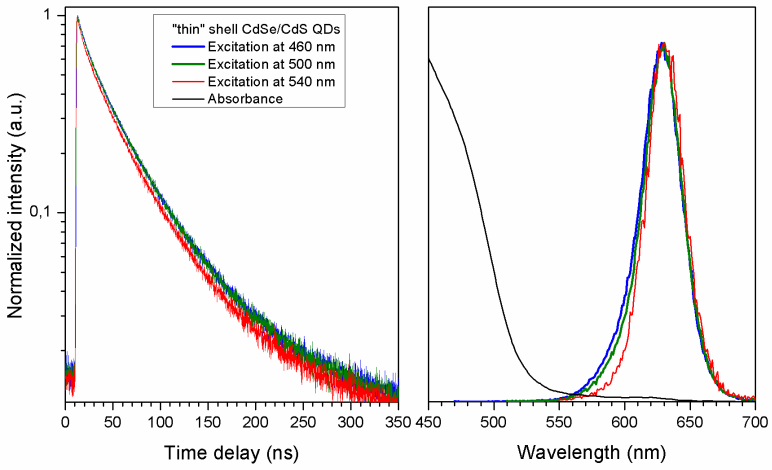

(a) "Thin" shell CdSe/CdS quantum dots (core diameter 3.5 nm, total size 13-16 nm)

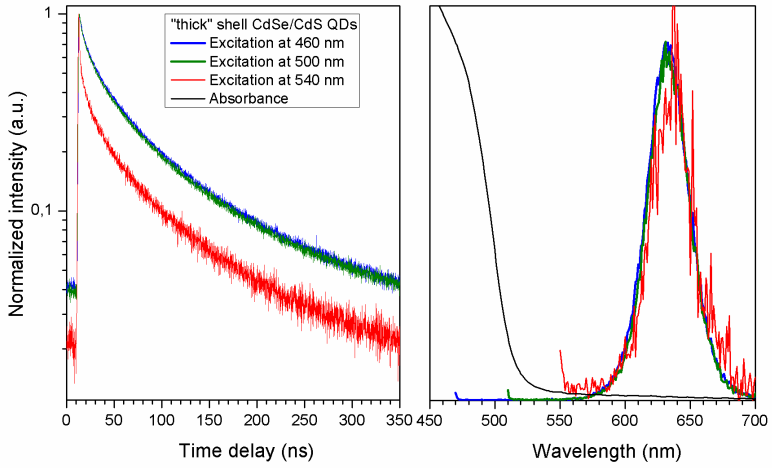

(b) "Thick" shell CdSe/CdS quantum dots (core diameter 3.5 nm, total size 22-28 nm).

Figure 3.1.: Ensemble fluorescence decay curves, excited at different wavelengths (excitation window 4 nm) with corresponding emission and absorption spectra.

separated from the laser beam with suitable filters. Fig. 3.2 shows a scheme of the FLSM setup. The core of this setup is the MicroTime 200 Fluorescence Microscope of PicoQuant GmbH [127].

The confocal Fluorescence Lifetime Imaging System is built around the MicroTime 200 solution. This setup is completed with some add-ons. The complete setup

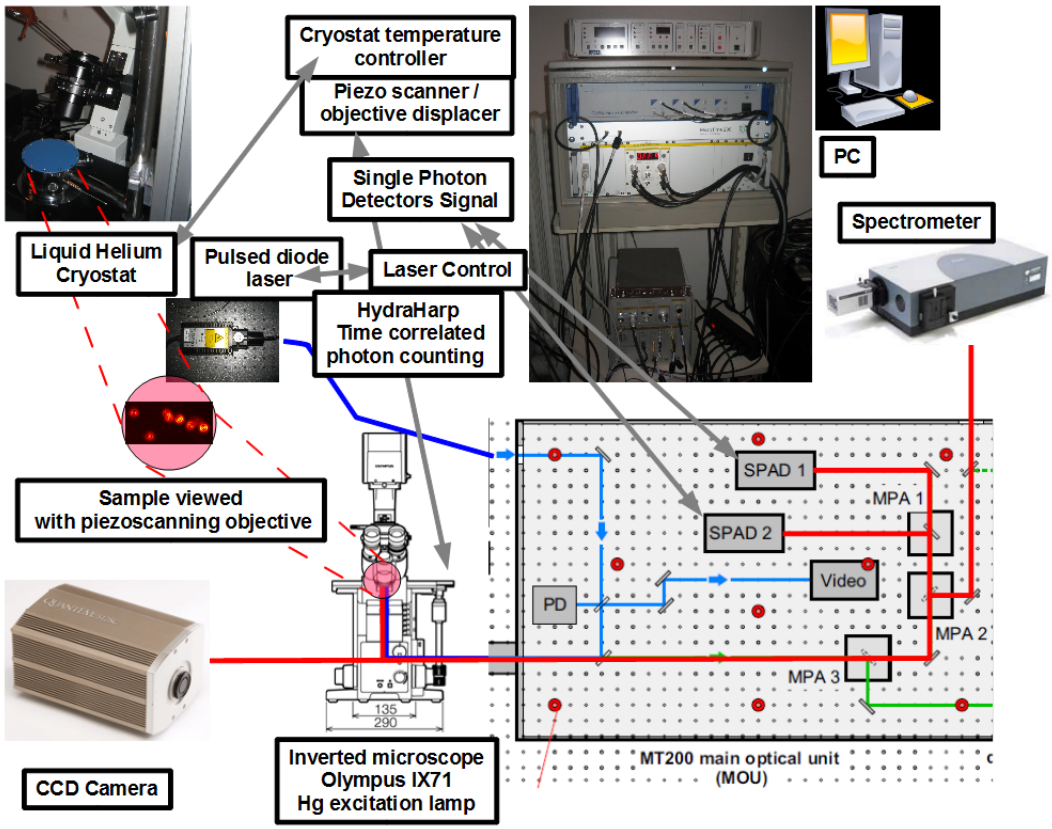

Figure 3.2.: Scheme of the complemented MicroTime 200 experimental setup.

includes the following components:

- Laser excitation subsystem, with a pulsed diode laser driver, a fiber coupling unit with the 402 nm diode laser head, and a polarization maintaining single mode optical fiber. The laser used for the excitation is a laser diode manufactured by PicoQuant (product LDH-D-C-405) with Peltier temperature stabilization set at 20°C. The emission wavelength is $\lambda = 402$ nm. The laser driver has two master frequencies 80 MHz and 1 MHz with binary dividers 1 to 32, which allows pulse repetition rates ranging from 31.25 kHz to 80 MHz. It is also possible to use the laser in a continuous mode. An intensity knob allows to change the laser intensity, however in order to have best pulse shape, one should use a laser intensity just above threshold. Intensity can also be adjusted with the help of an optical attenuator at the exit of the laser (micrometer-driven slit). The FWHM measured for a single pulse with the avalanche detectors without impulse response deconvolution is 150-200 ps depending on the intensity and chosen divider. The laser beam enters a single mode polarization maintaining fiber of length ~3m and its polarization is horizontal when it enters the confocal unit. A second fiber entry is used for the NKT Photonics supercontinuum laser, which we described earlier.

- Main optical confocal unit with an inverted Olympus IX71 microscope. This confocal unit directs the laser beam on a diffraction limited focal spot of the sample. The useful fluorescent photons take the return path through the microscope objective and pass through a dichroic filter towards the single photon avalanche detectors. Lenses and a 30 – 150 μm pinhole collimate the fluorescent photons on the detectors. On its path, 10% of the laser beam is directed towards an intensity measuring photodiode in order to monitor the intensity. On its back reflected path, the laser beam is also directed towards a video, which allows to control the focus in the plane of the sample. The position of the objective of the microscope is displaced horizontally (x-y direction) with a piezo scanner controlled by the software. The maximum useful area is 80*80 μm for 150*150 pixels. A vertical piezo positioner (z-direction) facilitates fine-tuning of the focus.
- Detection subsystem, with two single photon avalanche detectors (SPADs). The two SPADs of manufacturer Micro Photon Devices allow detection of single photons at picosecond time resolution. The SPADs have a dead time of 80 ns. Acquisition card and software is delivered with a HydraHarp acquisition card which monitors the detection. Two detection modes are available:
  - T2 mode. The absolute arrival times of the detected photons are recorded. This mode is used for determination of antibunching correlations.
  - T3 mode. This mode synchronizes laser pulse and fluorescence photon detection via cycles: Laser pulse → detection time → dead time → laser pulse → detection time → dead time → *etc.* It records each photon's timestamp relative to the preceding pulse and to the absolute start of the measurement. MicroTime 200 is delivered with SymPhoTime software which allows triggering and processing of the spatially and time resolved fluorescence intensity traces.
- PC, control electronics and software (SymphoTime from PicoQuant). I have used additional Matlab software developed by Mickaël Tessier in order to analyze the files recorded in T3 mode.
- A Shemrock 750 spectrometer with 150 l/mm grating and maximal resolution of 0.8 meV with software and CCD camera (Andor Technology).

3.2.2. Time resolved measurements

Single CdSe spherical quantum dots are naturally blinking and rapidly bleaching when submitted to excitation [128]. Their luminescence behaviour is improved when capping the shell with a semiconductor of higher bandgap, like ZnS or CdS. This capping isolates the exciton from the surface traps [64]. The time-resolved measurements were performed on core-shell CdSe/CdS quantum dots. The dynamics of these dots and the role of Auger processes has been described by previous work involving the group [129, 11].

3.2.2.1. Statistical measurements on glass slide

Time traces of single "thick" shell CdSe/CdS quantum dots (core diameter 3.5 nm, total size 22-28 nm, ensemble emission at 633 nm) have been recorded in monoexcitonic condition on a glass slide, with the pulsed diode laser.

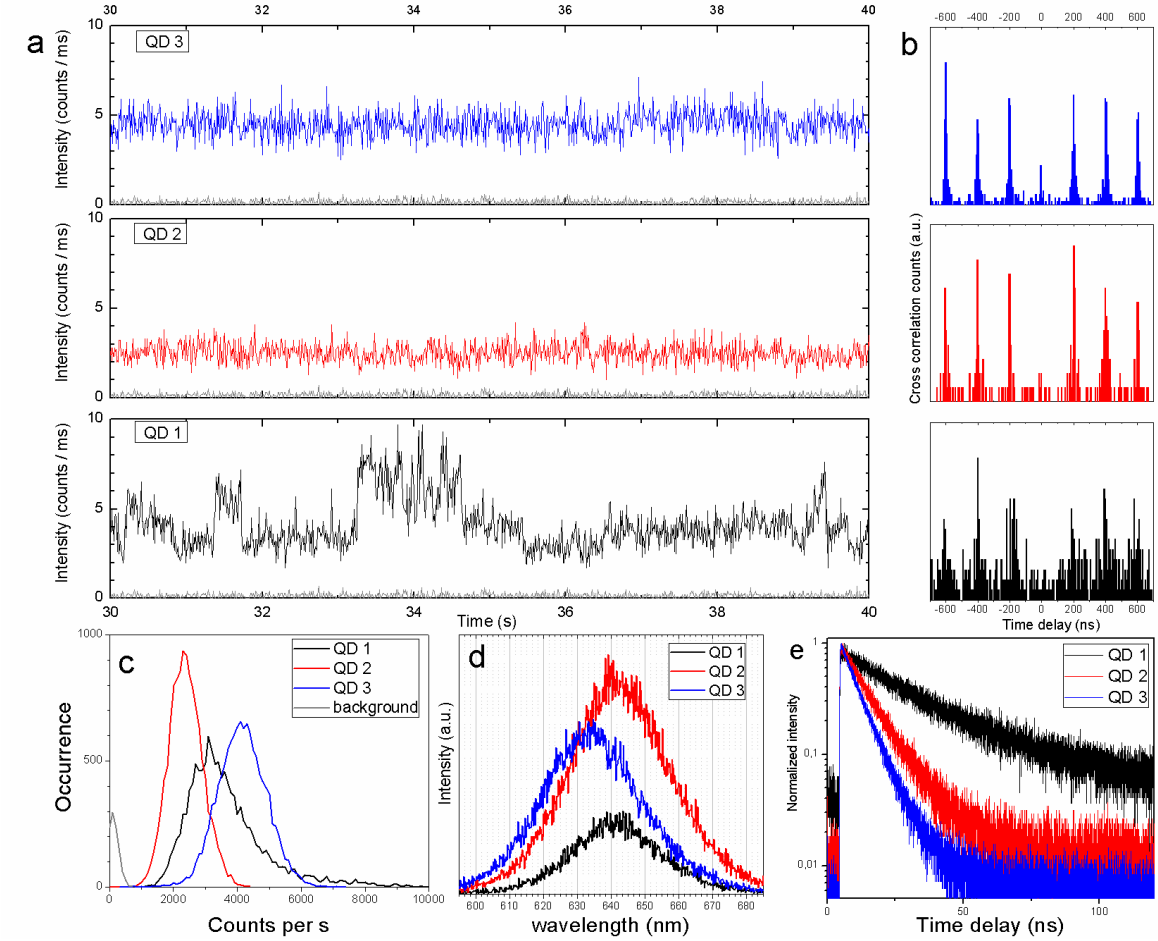

Figure 3.3.: Time resolved and spectral measurements for three typical individual CdSe/CdS core-shell quantum dots excited with a repetition rate 5 MHz at 402 nm, at room temperature. The single photons are collected in 16 ps bins, with a ×100 oil objective, NA=1.4 and a long-pass 590 nm emission filter. (a) 10 s range of the time traces; the grey colored trace is the background noise level. (b) Antibunching graphs. (c) Occurrence graph of the emission intensities for second bins. (d) Emission spectra. (e) Fluorescence decay graphs; the fitted lifetimes related to the charged states are 23 ns (QD 1), 10 ns (QD 2), 7 ns (QD 3).

Fig. 3.3 shows time traces and related antibunching, occurrence, spectral and fluorescence decay graphs of three typical individual QDs excited with constant low intensity. The antibunching graph with a low peak at zero anti-correlation delay indicates with high probability that we have recorded emission from single QDs. Some

show the fluctuating two state emission, with a larger average lifetime, which relates to the alternating neutral (long lifetime ~100 ns) and charged (shorter lifetime ~20 ns) states described in previous work [129, 11] (example of QD 1 in Fig. 3.3). The majority have a very stable lower emission state, which corresponds to the charged state (example of QD 2 and 3 in Fig. 3.3). Overall, the emission peaks of large samples range from 610 to 650 nm, with FWHM of 25-30 nm. Their (charged) fluorescence decay lifetime may vary from 5 to 30 ns without clearly depending on their emission wavelength.

In order to have a better understanding of the cause of these variations, it is required to complete characterization of the individual quantum dots. This requirement was the motivation to start correlated optical fluorescence and electronic microscopy single QD observations, see sec. 3.3.

3.2.2.2. Supercontinuum laser

We have also initiated fluorescence decay measurements on single QDs, varying the excitation wavelength with the supercontinuum laser. We recorded the luminescence of single quantum dots excited at 480 nm, 520 and 540 nm. As the absorption cross section for energies close or lower than the CdS absorption onset is very small, the photoluminescence is hard to record at 540 nm. Fig. 3.4 gives the decay curves for the three excitation wavelengths for a single QD, with the two-exponential fitting parameters listed in Tab. 3.2. Surprisingly, the effect was contrary to the one in ensemble. The lifetime becomes larger as the wavelength of the excitation increased. This may however be due to different charging in the two cases [130]. The time trace of the QDs excited at 540 nm seems to have two fluorescence levels, the higher level accounting for the longer lifetime. These measurements have not been continued and need further investigation.

	Excitation	τ_1 in ns (with proportion)	τ_2 in ns (with proportion)
"thick" shell CdSe/CdS QD	480 nm	29 (82%)	1.4 (18%)
	520 nm	36 (83%)	2.2 (17%)
	540 nm	75 (85%)	4.2 (15%)

Table 3.2.: Parameter values for a two exponential fit of the fluorescence decay curves of core-shell CdSe/CdS quantum dot characterized in Fig. 3.4, excited at different wavelengths. The proportions p_i are expressed as percentages $p_i = a_i\tau_i / \sum a_j\tau_j$, where the a_i are the amplitudes of the fit exponentials.

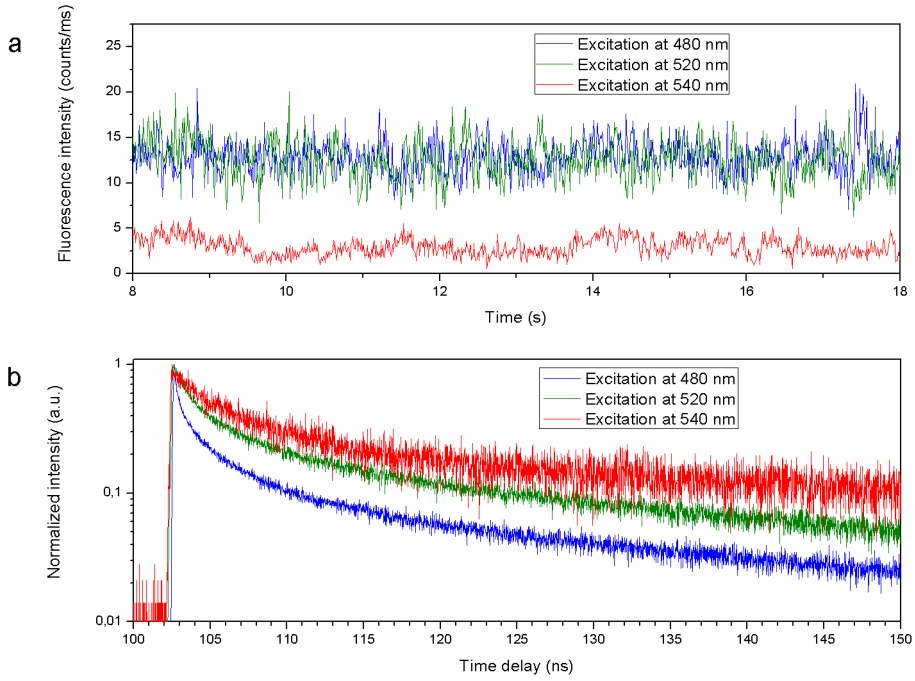

Figure 3.4.: (a) Time trace and (b) fluorescence decay curves of the same single "thick" shell CdSe/CdS quantum dot (core diameter ∼3.5 nm, total size 22-28 nm), excited at different wavelengths (excitation window 4 nm).

3.2.2.3. Comparison air / vacuum

We have performed series of measurements under air and vacuum environment. We drop-casted 10µl of "thick" shell CdSe/CdS quantum dots (core diameter 3.5 nm, total size 22-28 nm) dispersed in a hexane/octane solution (90% hexane, 10% octane) on a sapphire slide. The sapphire slide was fixed in the cryogenic unit (Oxford Instruments, Microstat-HiResII). We recorded time traces for single QDs with a ×60 Olympus objective with numerical aperture (NA) 0.7. We started under ambient air environment. Then we vacuum-pumped the unit at 3.10^{-6} mbar and recorded time traces for the same dots. After that, we stopped the pump and opened the valve in order to perform time traces under air environment again. The excitation source is the 402 nm pulsed laser diode at 10 MHz repetition rate. Due to poor photon collection with the 0.7 NA objective and a high background noise signal, fluorescence of quantum dots with antibunched counts were too weak to be recorded in this setup. Fig. 3.5 gives (a) the time trace, (b) the antibunching graph and (c) the decay curve for a fluorescence spot in the different environments. The spot probably originates from several aggregated dots, as the zero offset antibunching peak has the same intensity as the delay peaks. Tab. 3.3 gives the fitting parameters

for the decay curves. We can remark the very stable, non fluctuating time trace in air as well in vacuum. This may be interpreted as originating from the charged state X* as explained for similar results by Clémentine Javaux [13].

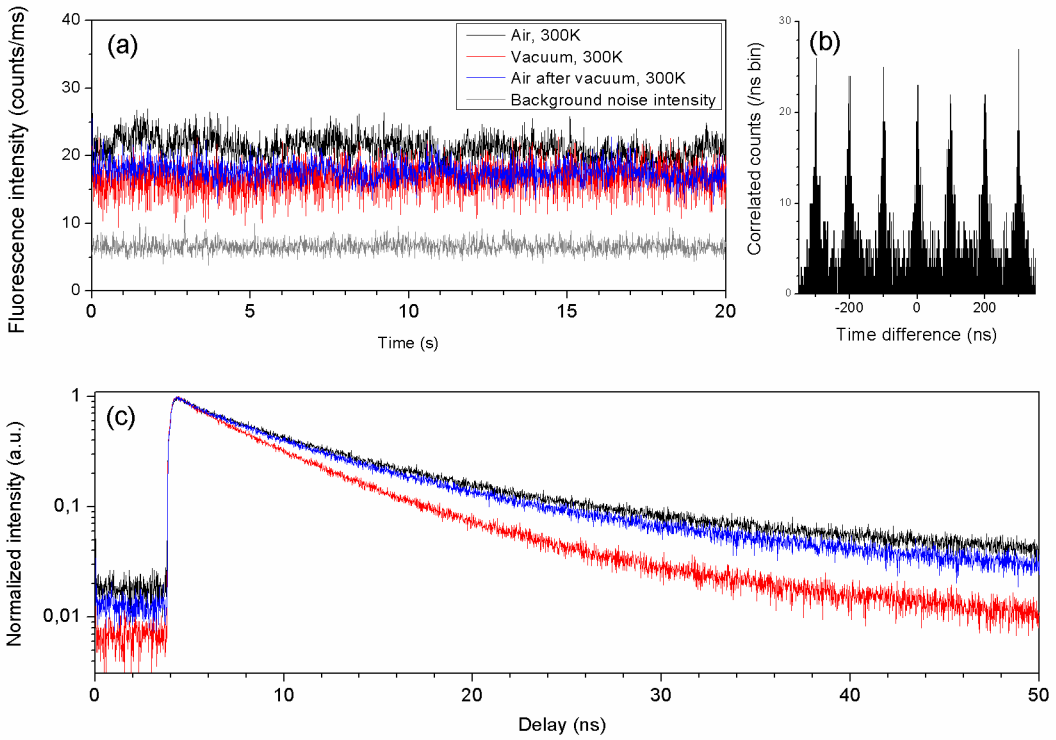

Figure 3.5.: Typical fluorescence decay curves for a core-shell CdSe/CdS quantum dot aggregate on a sapphire slide successively measured at ambient air, at vacuum and back to air.

	τ_1 in ns (with proportion)	τ_2 in ns (with proportion)
Air	19 (57%)	5.2 (43%)
Vacuum	10.5 (48%)	3.9 (52%)
Air after vacuum	16 (58%)	4.6 (42%)

Table 3.3.: Parameter values for a two exponential fit of fluorescence decays of ensemble samples for a core-shell CdSe/CdS quantum dot aggregate on a sapphire slide successively measured at ambient air, at vacuum and back to air. The proportions p_i are expressed as percentages $p_i = a_i\tau_i / \sum a_j\tau_j$, where the a_i are the amplitudes of the fit exponentials.

3.3. Correlating photoluminescence and electron microscopy

Time-resolved single particle fluorescence microscopy often reveals a wide variety of behaviors for single particles from the same batch sample [131], as confirmed by statistical measurements on the CdSe quantum dots synthesized during this research work. Some particles are blinking, some are not, some may even be extinct [132]. The fluorescence lifetimes may vary over large ranges. This diversity is often attributed to specific localization of trapping sites inside or at the surface of the QD, but other characteristics play a role, like shape, structural polytypism, aggregation, quenching due to interaction with a specific environment or capping ligand, positive or negative charging of the quantum dot. Precise investigation of this polydispersity in single particle behavior is difficult to achieve. It is possible to correlate fluorescence microscopy, whose resolution is of the order of the wavelength of the probing light source, to techniques that allow higher resolution, like scanning or transmission electron microscopy (SEM or TEM) [133, 134, 135] or atomic force microscopy (AFM) [132, 135]. Recently, the possibility of optical and electron microscopy colocalisation on a scanning tunneling electron microscope (STEM) with a cathodoluminescence (CL) detector [136] has opened perspectives for comparing photoluminescence and cathodoluminescence on the very same single nanosized objects, which we will report in sec. 3.3.3.3.

TEM is the best tool to investigate the crystallographic arrangement in single quantum dots. We therefore focus on the correlation between optical fluorescence microscopy and transmission electron microscopy. The goal of this work is to give the underlying ins and outs that would facilitate that correlation, to define a standard mode of operation and to apply it to the semiconductor nanocrystals synthesized in the group.

The first issue is to choose a substrate that is adequate for both fluorescence and electron microscopy.

The second issue is to correlate objects observed at scales separated by 3 orders of magnitude. With optical microscopy, high resolution scales are of the order of microns, while in electron microscopy high resolution scales are of the order of nanometers. Observing the same objects with both techniques therefore necessitates sufficient spreading between the different nanocrystals. We also need a technique that facilitates cartographic lecture of the localized objects. Lithographic patterns have been used.

The third issue is to define a relevant mode of operation in order to perform the desired measurements. Photoluminescence experiments must be performed before the electron microscopic observation because the high energy and current of the electron beam may have detrimental effects on the photoluminescence of the nanoobjects. This has been attributed to the detachment of the organic ligands, and not to the structural degradation of the QDs [133].

Further issues deal with experimental results obtained during this doctoral research work

3.3.1. Choosing the appropriate substrate

If we intend to investigate the sample through TEM, the substrate must be transparent to the electrons accelerated from the electron gun towards the specimen holder. All support films in the catalogues of professional TEM grid suppliers are suitable. We can mention carbon, silicon, silicon oxide, silicon nitride, polyvinyl acetal, formal or butyral resins (FormVar®). In order to avoid capacitive charging on the grid that would imply image distortion and therefore difficulties to achieve high resolution, excess charges must be carried away rapidly from the sample holder. Therefore, electron microscopy prefers conductive substrates like carbon.

For optical fluorescence microscopy, the conductivity of the substrate is however a drawback. If the excited electron is carried away before it can recombine with the hole, the fluorescence is quenched. A conductive substrate can sometimes have the opposite effect of fluorescence enhancement [137, 138, 139]. The exact behavior is determined by the electromagnetic or plasmonic coupling between the substrate and the nanocrystal.

Most often, a glass slide (silicon dioxide) is used as substrate for the examination of the PL dynamics of single nanocrystal emitters. For TEM grids, silicon dioxide membranes suitable for HRTEM are however very fragile and break too easily if one applies lithographic patterns in order to facilitate localization.

We have probed the following substrates: carbon, silicon nitride and silicon.

Time-resolved photoluminescence observations have been performed on the confocal setup with core-shell QDs (core diameter 5 nm, total size 22-28 nm, synthesized by Clémentine Javaux [13]) on a copper TEM grid with carbone membrane (5-10 nm in thickness), with air objective ($\times$100, NA=0.9) at repetition rates 1 MHz. Fig. 3.6 illustrates the typical shortening of decay lifetime due to the carbon membrane with respect to a glass slide. These QDs had a long lifetime of 40-60 ns on a glass slide, while on the copper TEM grid with carbon film, this lifetime was reduced to 4-6 ns with a much lower photoluminescence intensity.

Silicon or silicon nitride membranes are better suited for photoluminescence experiments than carbon films. Silicon nitride is a better dielectric than pure silicon and QDs dispersed on it should therefore have a better photoluminescence signal. The measured charged lifetimes of the reference “thick” shell CdSe/CdS quantum dots (core diameter 3.5 nm, total size 22-28 nm, ensemble emission at 633 nm) on silicon nitride are comparable to those measured on glass (10-20 ns), while on silicon the lifetimes are of the order of 5-10 ns.

In order to carry out HRTEM observations, it is important to have TEM grids with a very thin membrane ($<$20 nm).

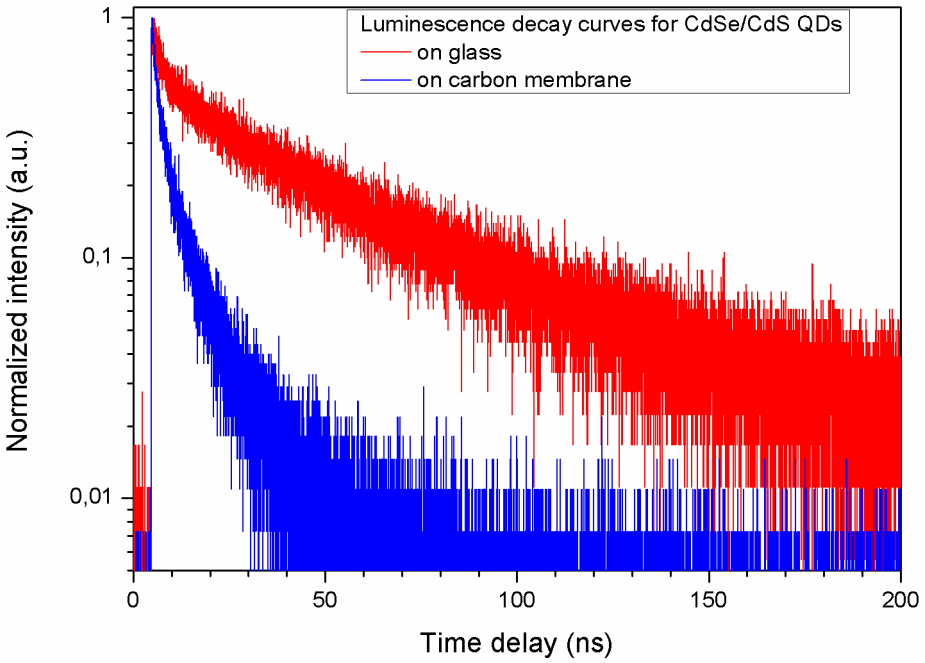

Figure 3.6.: Photoluminescence decay comparison for typical single CdSe/CdS QDs on a glass slide and a TEM grid carbon membrane.

Confocal microscopy on thin membranes suffers from larger photon collection loss. Silicon nitride also suffers from some autofluorescence near the wavelengths of interest (600-650 nm). Higher excitations are needed, with the drawback of exciting multiple excitons. In order to reduce the noise for these measurements, we use a LP590 filter at the detection end.

It has been verified that the substrate has a strong influence on the luminescence dynamics of single nanocrystals [140]. Comparison between carbon, silicon and silicon nitride show that silicon nitride membranes are better suited for joint observations of the same QDs in photoluminescence and TEM. This agrees with the choice for previous correlated PL and TEM observations [133].

3.3.2. Facilitating localization of the nano-objects

Good dropcast or spincoating dispersion of the nanocrystals is important to facilitate colocalization between optical and electronic microscopy. The thickness of the membrane plays also a role in the drying and thus in the dispersion of the droplet, especially when there is a little temperature difference between the droplet and the membrane. We have tried plasma cleaning of the TEM grids before drop-casting

and this didn't seem to have a noticeable effect, with respect to the as received TEM grids.

In order to facilitate localization of the quantum dots in both PL and TEM observations, we have used grids with labeled gold or titanium markers every 5 µm, see Fig. 3.7. These markers can be seen both in optical and electron microscopy. They were prepared by Zackaria Mahfoud using electron beam lithography [141].

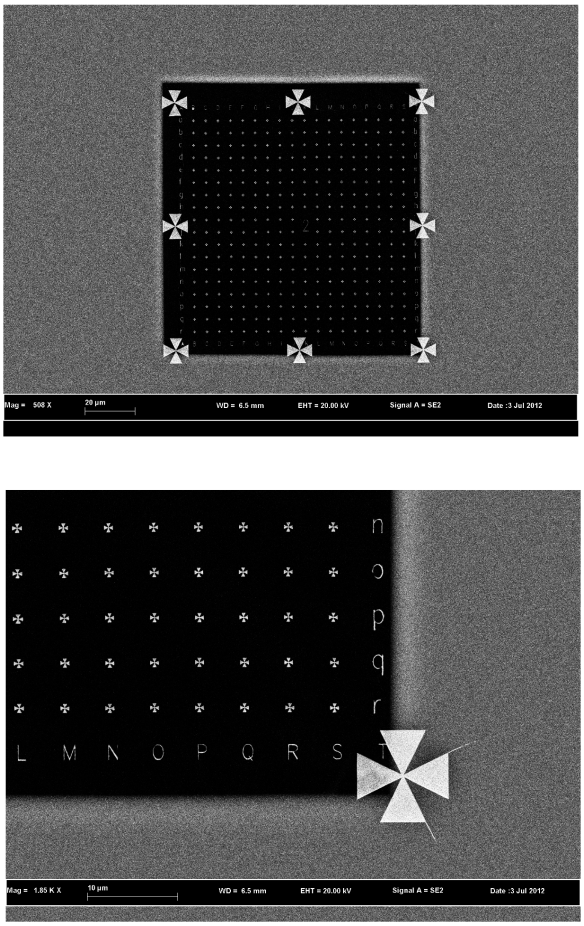

Figure 3.7.: 100×100 µm window of a TEM grid with gold markers every 5 µm. Courtesy of Zackaria Mahfoud.

It should be noted that fluorescence excitation with a laser on nanocrystals that are located too near to the markers will warm up the markers and cause x-y or even z-drift. It is thus easier to work on nanocrystals that are located well in the 5µm×5µm marker delimited field.

3.3.3. Results on quantum dots

3.3.3.1. Aggregates

We started the colocalisation observations on a silicon TEM grid for which the luminescence of single QDs was insufficient to record time traces with the confocal setup. We observed several aggregates first on the optical confocal setup (diode laser 402 nm, repetition rate 10 MHz, constant excitation intensity) in order to obtain their decay curves. After that we imaged them on the JEOL TEM. The results are given in Fig. 3.8 (a). The corresponding TEM images of these aggregates are given in Fig. 3.8 (b), in the order from the shortest to longest decay lifetimes. It can be seen that the field in which these QDs are located is of the order of 300 × 300 nm, which is smaller than the laser spot.

The decay curves do not seem to be related to any obvious features like packing or number of QDs. The number of QDs in the aggregates ranges from 30 to 120 which should be sufficient to average the lifetimes and give nearly identical decay curves. The fact that the decay curves are not similar could suggest that the absorption cross section and thus the regime of multi-excitonic excitation is different from one case to the other, which in turn gives different decays.

After observation on TEM at 200kV, the QDs and aggregates of QDs are generally bleached. We verified the PL of the QDs after observation with the TEM. Of the six aggregates presented in Fig. 3.8, only the one with the longest lifetime gave a processable PL signal after observation in the TEM. The lifetime was shortened by a factor 5, see Fig. 3.9, which can be explained by the fact that the electron beam alters the QD in such a way that non-radiative recombination pathways are favored above PL.

Interestingly, we can also note a clear difference in delay in reaching the maximum of emission after excitation (some hundreds of picoseconds), see the inset of higher time resolution of Fig. 3.9, indicating a longer delay for the carrier dynamics to reach equilibrium.

3.3.3.2. Size Structure

We have performed different observations on single QDs in order to try to find correlations between TEM observed size, shape, structure and PL observed emission wavelength, time trace and lifetime. We have used TEM grids with a silicon nitride membrane of thickness 15 nm.

After treatment of 30 QDs, we haven't noticed any obvious statistical correlation of the TEM-imaged shape and size with the emission related physical features like fluorescence decay, emission states and emission wavelength. This correlation may be easier to detect for QDs with thinner shells.

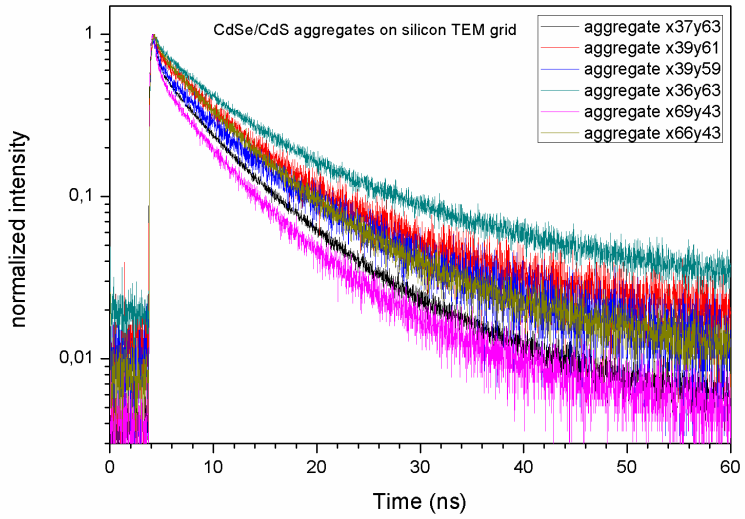

(a) Fluorescence decay curves of CdSe/CdS QD aggregates on silicon TEM grid

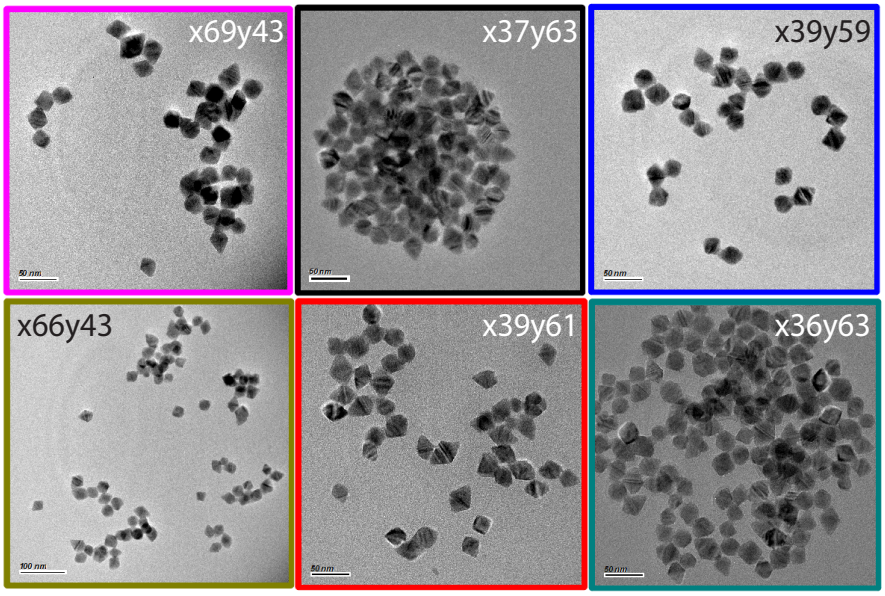

(b) TEM images of corresponding CdSe/CdS aggregates

Figure 3.8.: Colocalisation of aggregates

3.3.3.3. Cathodoluminescence compared with photoluminescence

In the series of correlated single QD observations with optical and electron microscopy means, CL observations have been performed by Zackaria Mahfoud [141].

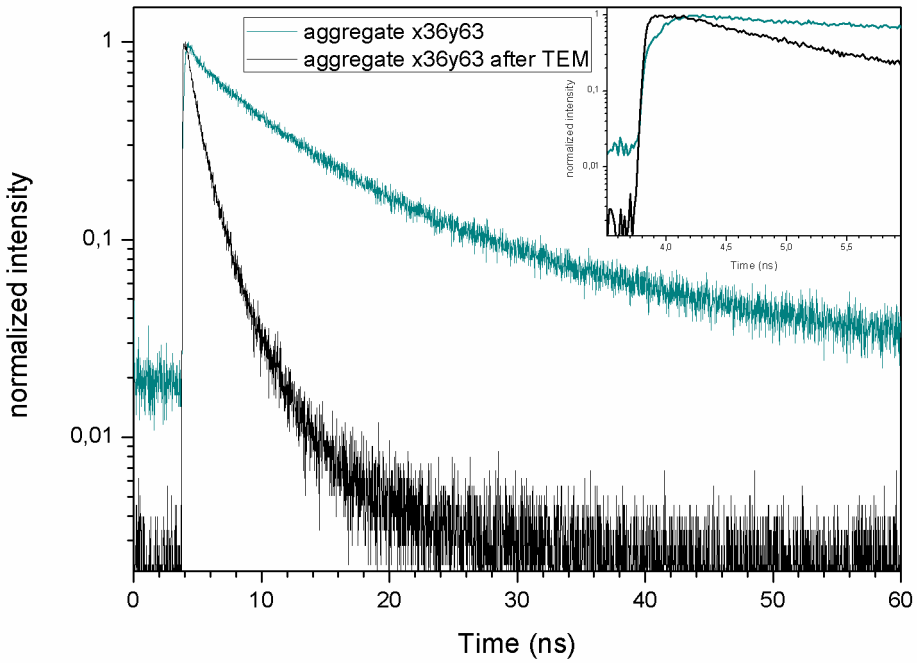

Figure 3.9.: Fluorescence decay curves of a CdSe/CdS QD aggregate on silicon TEM grid, before and after observation with TEM

After measurements of the PL characteristics of single QDs on TEM grids with gold markers at room temperature, cathodoluminescence observations were performed on a Vacuum Generators HB-501 STEM at 150 K, equipped with a nanometer scale cathodoluminescence system, developed specifically to monitor luminescence effects at nanometer scale [136]. Its collection angle is 1.4π srd, covering a great deal of the three spatial directions. In this STEM, when the electron beam is scanned on the sample, high-angle annular dark field (HAADF), bright field and luminescence signals are recorded simultaneously. The scanning resolution (~1 nm) is much better than the quantum dot size. Spectral CL images can thus be recorded for individual QDs, even in packed ensembles. In the experiments of the present research work, however, as we were interested in comparing CL and PL spectra, the QDs were sufficiently separated to ensure that we recorded the signal of the same QD in both setups (more than 2 µm between neighbouring QDs).

As explained earlier, PL measurements have to be performed before the CL measurements, as the higher energy of the electrons may cause bleaching or even some damaging effects on the QDs. For the PL observations, the TEM grid (3 mm diameter) has to be sustained in a sample holder above the air objective. If we used a conductive sample holder, it was noted that the QDs lost their fluorescence after a day. We therefore used non-conductive 3D printed polymer slides with a hole

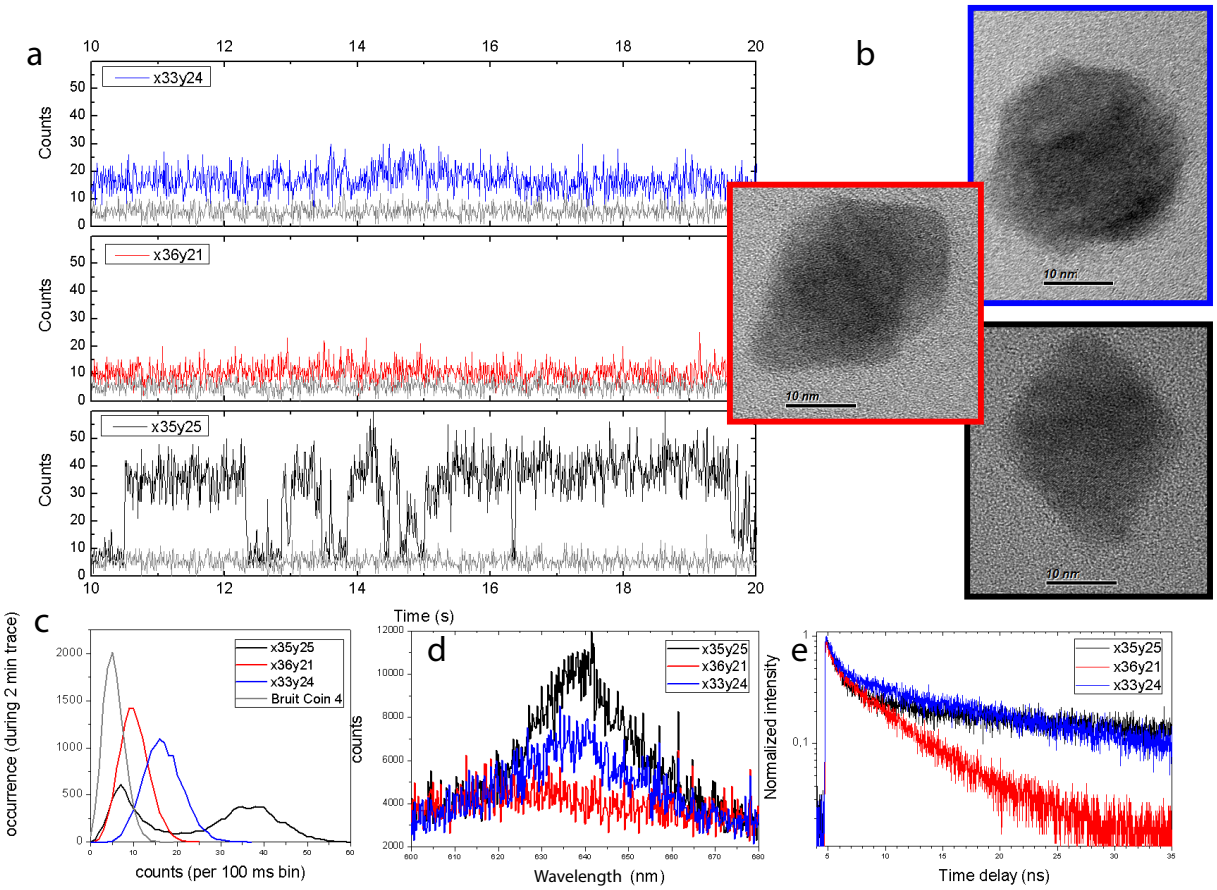

Figure 3.10.: TEM images of three typical individual CdSe/CdS core-shell quantum dots, with their time resolved and spectral measurements. The excitation is at constant intensity, with a repetition rate 5 MHz at 402 nm, at room temperature. The single photons are collected in 16 ps bins, with a ×100 air objective, NA=0.9 and a long-pass 590 nm emission filter. (a) 10 s range of the time traces; the grey colored trace is the background noise level. (b) TEM images. (c) Occurrence graph of the emission intensities for second bins. (d) Emission spectra. (e) Fluorescence decay graphs.

slightly smaller than 3 mm, which could sandwich the TEM grid. Manipulation of the grids needs great care and in order to avoid aging of the QDs (and thus loss of luminescence), CL observation needs to be performed within a week after the PL observation.

We have observed some 30 QDs jointly with PL and CL. In the first experiments, due to a problem of calibration for the PL observations, the spectra could not be compared. In latter experiments, three QDs gave usable signals. Fig. 3.11 (a) illustrates the result for one of them. We remark that the CL spectrum is blue-shifted by 10-16 nm with respect to the PL spectrum. Due to the temperature

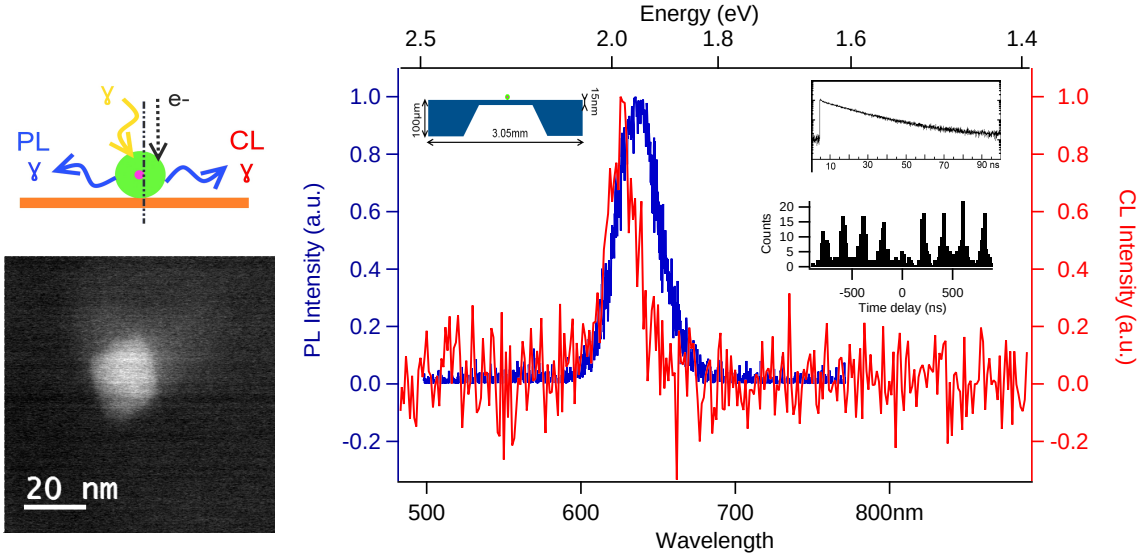

(a)

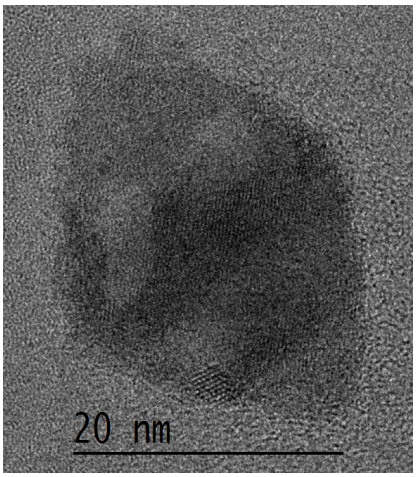

(b)

Figure 3.11.: (a) Photoluminescence and cathodoluminescence of the same quantum dot, courtesy of Zackaria Mahfoud [141]. On the left, the HAADF image of the studied QD, with its characteristic bipyramidal shape. The photoluminescence decay curve (lifetime 17 ns) and anticorrelation graph are given as insets of the spectral graph. (b) High magnification TEM image of the studied QD after the CL observation.

dependence of the emission wavelength, the expected blue-shift is 14 nm [142], thus explaining this difference. We also remark a smaller FWHM for CL (14±5nm). It should be noted that the integration time for the CL spectrum is 50 ms, while for the PL spectrum, it is 60 s. The difference in FWHM is therefore probably caused by spectral diffusion [143].

It is essential to investigate in more detail the amount of damage caused by electron beams on individual QDs. Is the loss of luminescence due to a degradation of the capping ligands, or is it due to structural damages? And is it possible to reduce those degradations by tuning electron beam current and voltage? This investigation is required if one wants to substitute PL characterization of individual QDs by higher resolution CL characterization in reusable devices.

In order to feed these further investigations, we report some observations on the QDs after having performed the CL experiments.

Firstly, most of the CL-observed QDs could not be observed afterwards when we mounted the sample on the confocal setup. Some few single QDs showed a shortening of the decay lifetime, as was already reported in sec. 3.3.3.1 for the aggregated QDs after passing under the 200kV beam of the JEOL TEM.

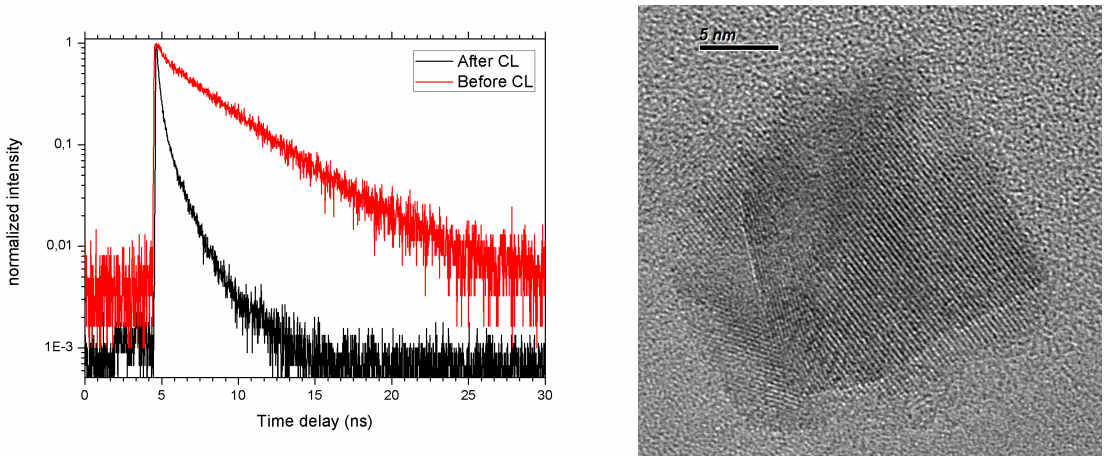

Figure 3.12.: (left) Fluorescence decay curves of a single CdSe/CdS QD on silicon TEM grid, before and after observation of CL in the STEM. The lifetime is reduced by a factor 7-8. (right) HRTEM image of the QD taken after the CL observation.

In Fig. 3.12, we have represented the PL decay curve of a single CdSe/CdS QD, before and after observation of CL in the STEM. As can be read from the scale, the lifetime is reduced by a factor 7-8 due to the CL experiment. It should be noted that no CL signal has been detected for this QD. On the right, the QD is shown at high resolution after the CL observation. We remark some sharp unusual contrasted lines which suggest structural damage and which has been observed on other QDs after the CL observation.

Fig. 3.13 shows other TEM images taken after the CL observation. Little unusual fragments of same contrast as the QD can be seen in the neighbourhood, but often very close as in Fig. 3.13 (a), generally nearer than 500 nm. The last effect we have observed is a suggested crystalline annealing of the QD, which will produce a smooth surface or a melting or separation of two QDs, examples given in Fig. 3.13 (b). These

damaging effects could be related to long observation times in the STEM, especially in order to perform multiple scans of the same area.

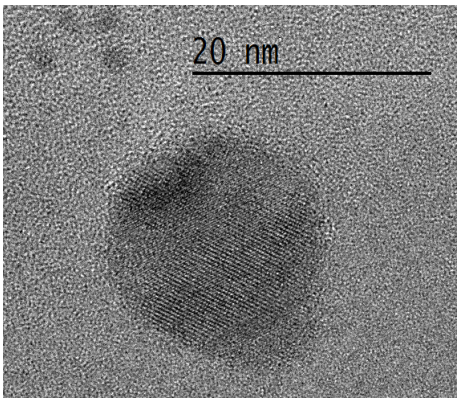

(a)

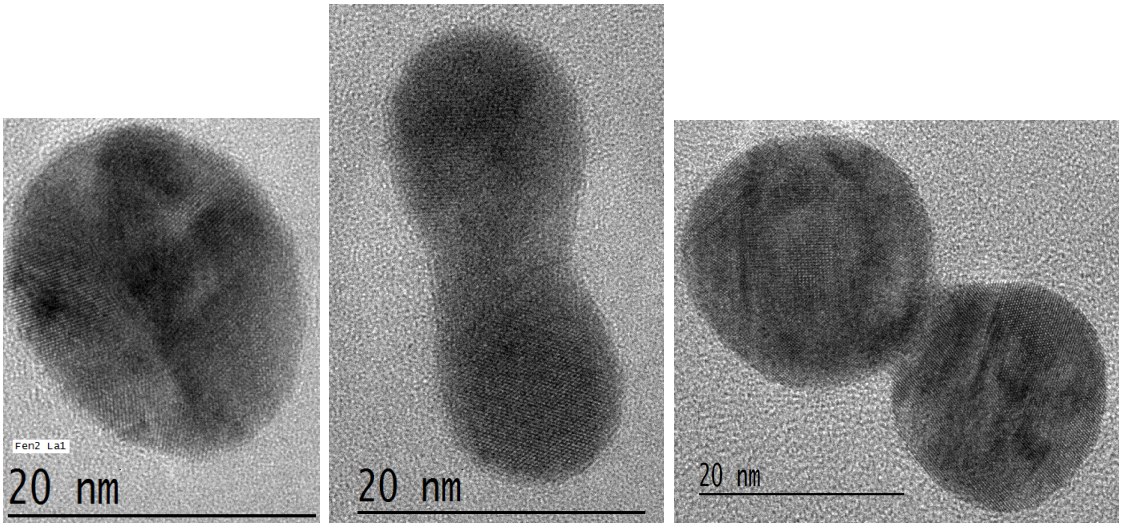

(b)

Figure 3.13.: Suggested damages induced by electron beam during CL experiments. (a) fragments exploded from the top of a pyramid of the QD. (b) structural annealing of the quantum dot with smoothing of the surface and separation in two separate QDs or melting of two in one.

3.3.4. Results on nanoplatelets

As it has been difficult to find correlations between optically observed PL characteristics (spectrum, lifetime, time trace) and TEM observed shape, size or structure, we have considered a system with a thinner shell: the core-shell nanoplatelets.

Core-shell CdSe/CdZnS nanoplatelets have been synthesized by Brice Nadal using a protocol developed in the group [144]. The core nanoplatelets are 4 monolayers thick

and emit around 510 nm. When a 2 nm CdZnS shell is grown on these nanoplatelets, they emit around 620 nm with reduced blinking. Upon lateral extension of the nanoplatelets, the emission wavelength slightly shifts towards lower energies, an effect we will later discuss in sec. 4.2.2.2. As the core-shell nanoplatelets have good emission properties at room temperature, it is possible to study this lateral extension redshift with correlated PL and TEM observations.

We have dispersed the nanoplatelets on a silicon nitride TEM grid prepared with titanium markers every 5 µm. We then have performed PL observations and subsequently observed the spots at which a PL signal has been recorded with the JEOL TEM. Six nanoplatelets gave a usable signal correlated with TEM images of unambiguously related nanoplatelets. Fig. 3.14 (a) shows results for one of the nanoplatelets with a 10 s range of the time trace, the 618 nm centered spectrum and the related TEM image with the measured width and length. The time trace shows the blinking behaviour of the nanoplatelet.

Fig. 3.14 (b) gives graphs of the emission wavelength with respect to the length (upper graph) and the width (lower graph). We have verified on the small set of measurements that larger nanoplatelets emit at lower energies, an effect that can be explained with the confinement effect that is reduced due to their lateral extension. This confinement trend can be better seen on the graph with respect to the length.

It should be noted that there was a delay of 6 months between the synthesis of the core-shell nanoplatelets and the correlated PL and TEM observations. The photoluminescence intensity of the nanoplatelets may have suffered from this aging and the excitation intensity needed to be adapted in each case. This leaves some room for optimization for this study of the effect of lateral extension on the emission spectrum of single nanoplatelets.

3.4. Conclusion

We have investigated some aspects of the spectroscopy of CdSe/CdS core-shell QDs at room temperature. During this study, we have noticed that the excitonic recombination in these QDs occurs differently whether the excitation occurs in the core or in the shell. A more detailed investigation is required to disentangle collective and individual effects.

We have also succeeded in reproducing correlated PL and TEM observations on the same individual QDs and paved the way for further investigations, especially for core-shell nanocrystals with thin shell. For thin shell nanocrystals, it should be easier to relate their PL features to the size, shape or structure of the single nanocrystal. Improve the experimental aptitude towards better collection of luminescence signal and better HRTEM imaging should result in establishing new experimental results.

In collaboration with Zackaria Mahfoud, we have also succeeded in performing the first combined cathodoluminescence and photoluminescence experiments on the

same individual QDs. We verified that CL and PL occur at the same wavelength for individual QDs. This success opens promising perspectives, because it improves the spatial resolution in single QD spectral characterization by a factor 1000. Issues that need further investigation in this field are a better comprehension of the dynamical excitonic behaviour after cathodic excitation: energy relaxation, decay curve, lifetime, bleaching, possible structural modifications...

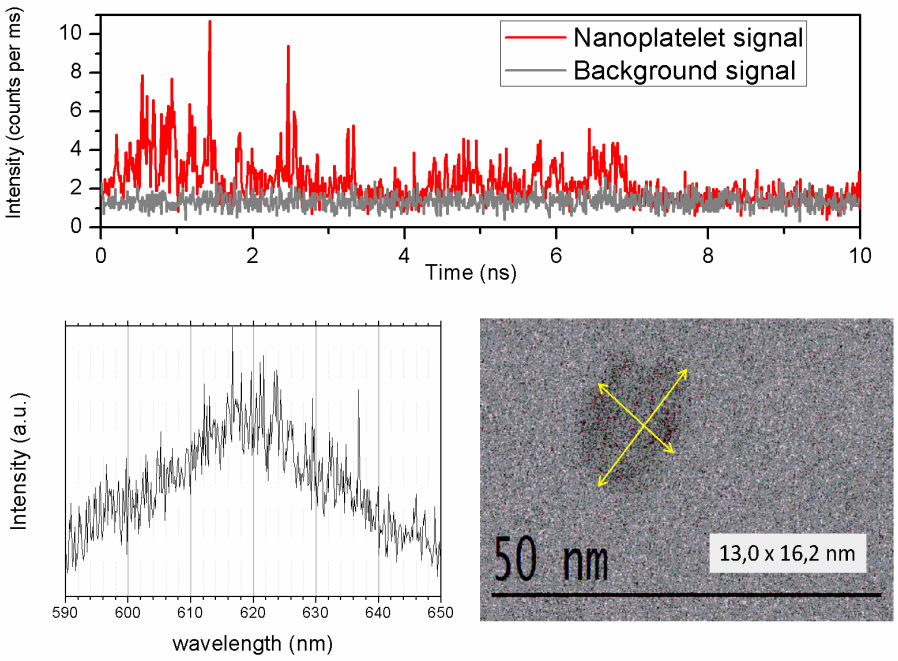

(a)

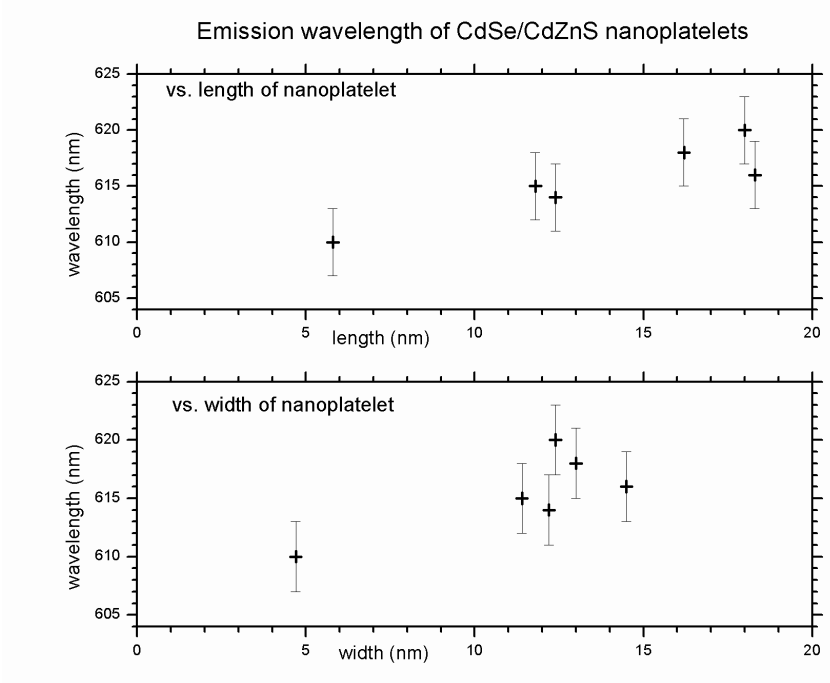

(b)

Figure 3.14.: Time- and spatially-resolved spectral characterization of the lateral extension of single nanoplatelets. (a) PL time trace and spectrum of a single core-shell nanoplatelet. The pertaining TEM image allows the determination of its size and shape. (b) Emission wavelength of the single nanoplatelets as a function of their width and length.

4. Modeling the excitonic transitions in semiconductor nanocrystals

The theorist may conclude that perhaps we should not try to force-fit existing theories to model excitations in nanostructures as they often carry with them assumptions that we have forgotten, or that we erroneously ignore. Nanoscale materials thus provide both a testbed and an inspiration for new quantum mechanical approaches to the calculation of electronic properties of large systems.

Gregory Scholes[145]

In the introduction (sec. 1.6), we have given a brief enumeration of theoretical approaches which describe the confining effect of a quantum potential (or a combination of quantum potentials) on the wavefunction of the electron and the hole in a semiconductor nanocrystal. The precise prediction of the energy size dependence of transitions requires refinements which complexify all these approaches. In the following, we present an alternative approach which aims to simplification, without loosing in precision.

When we describe the behaviour of quantum particles, we hold in mind the fundamental principles of quantum mechanics. These principles may be subject to different formulations and interpretations that are equally valid at the fundamental level [146]. This complicates the task of the physicist, because, in the chain of deductions leading to the description and predictions of experimental facts, branching points with differences in predictions occur. In this chapter, we will place ourselves at such a branching point and investigate an alternative descriptive pathway that takes advantage of a path integral approach similar to the one presented by Richard Feynman in his public lectures [147].

4.1. Phase jump approach

4.1.1. Presentation

The essential results of this presentation can be found in a modified form in the paper "Accurate Energy-Size Dependence of Excitonic Transitions in Semiconductor Nanocrystals and Nanoplatelets Using a Phase Jump Approach" [148] which has been submitted for publication.

4.1.1.1. Introduction

A growing appreciation of the exceptional physical properties of colloidal semiconductor nanocrystals has motivated extensive study of these materials since their discovery in the early 1980s [149, 57, 150]. Technological know-how, optimized colloidal syntheses, new experimental data and theoretical modeling steadily increased our understanding of the effects of the confinement of charge carriers in colloidal semiconductor nanocrystals, also called quantum dots (QDs) [151]. They constitute without doubt a very promising research field for the design of innovative materials. Several theoretical approaches have been used to describe the physics of the excitonic transitions in QDs. They include essentially EMA [73], tight-binding (TB) [152, 153, 90] and empirical pseudo-potential [106, 154, 155] approaches. These different approaches have led to a much better understanding of the confinement effect in the QDs, but in the case of the excitonic transition dependence upon the nanocrystal size, their predictions remain limited. For example, in the case of EMA for spherical quantum dots in the strong confinement, the following expression, already presented in equation 1.6, holds for transition energies [73]:

$$E_n = E_g + \hbar^2 k_n^2(a)/2m_e^* + \hbar^2 k_n^2(a)/2m_h^* - 1.8e^2/\kappa a \tag{4.1}$$

where E_g is the bulk band-gap, m_e^* and m_h^* are the electron and hole effective masses. k_n is the nth order wave-number that satisfies the boundary conditions and contains a $1/a^2$ dependence on the QD radius a.

Different corrections can be applied to this idealized treatment, including finite barrier, inter-band coupling, exchange interaction or size dependence of the dielectric constant. Adding these corrections generally results in non-analytic expressions for the energy-size dependence which can be numerically adapted to experimental data, in order to determine the appropriate parameters. But even with these refinements, a discrepancy between theoretical prediction and experimental data is observed, which is also designated as *"the problem swept under the rug"* [156]. For practical applications, the size of QDs is deduced from their absorption spectra using an empirical polynomial fit [114, 115].

Here we present an alternative way to investigate the carrier dynamics in semiconductor nanocrystals in the strong confinement regime, which leads to simple expressions for the energy-size dependence of excitonic transitions. It takes advantage of first principles in Feynman's rotating vectors [147] and includes a phase jump term in the solutions of the Schrödinger equation. The model is probed against high quality experimental data of CdSe and InAs QDs of the literature and shows good agreement in the strong confinement range. It is further verified and specified on semiconductor nanoplatelets, which provide a good benchmark for the comparison with different approaches.

4.1.1.2. Theoretical basis

We propose the following size-dependent expression for the energy of the i^{th} excitonic transition:

$$E^i(a) = E_0^i \frac{a + \gamma_\phi^i}{a + \gamma_t^i} \tag{4.2}$$

where E_0^i is a constant reference energy gap for the i^{th} excitonic transition and γ_ϕ^i and γ_t^i are respectively metric phase and time delay parameters for the same transition. Their physical interpretation will be discussed later.

Fig. 4.1 shows the fit with equation 4.2 of the high quality experimental data of the first excitonic transition of CdSe QDs published by Norris et al. [62]. The fit is very good (coefficient of determination $R = 0.9997$) and suggests that equation 4.2 could be used for size determination, equivalently to empirical polynomial fitting formulas of higher order [114, 115]. Equation 4.2 can also be used to fit the higher energy transitions of CdSe (see Fig. 4.2). For each transition, the set of parameters has to be adjusted, but the fit with the experimental data is strikingly good. Equation 4.2 can also be used to fit the InAs excitonic transitions reported by Banin *et al.* [63] with an accuracy equivalent to that of CdSe (see Fig. 4.3). This suggests that equation 4.2 can be used with success for various materials. In the following section we provide a framework that explains how we obtained equation 4.2.

4.1.1.3. Phase jump approach

Let us represent an electron by a spinning arrow or rod, which can be seen as the 3D analogue of a "phasor" or a "quantum stopwatch" [157, 158]. The rod spins around its geometrical center, with 2 degrees of freedom for self-rotation and a phase $\phi(t)$. The orientation of these self-rotations determines the polarization of the rod. The rod's instantaneous angular velocity $\omega(t) = d\phi/dt$ determines its energy $E(t) = \hbar\omega(t)$ (see the annex sec. A.3 for details). When this rod moves in

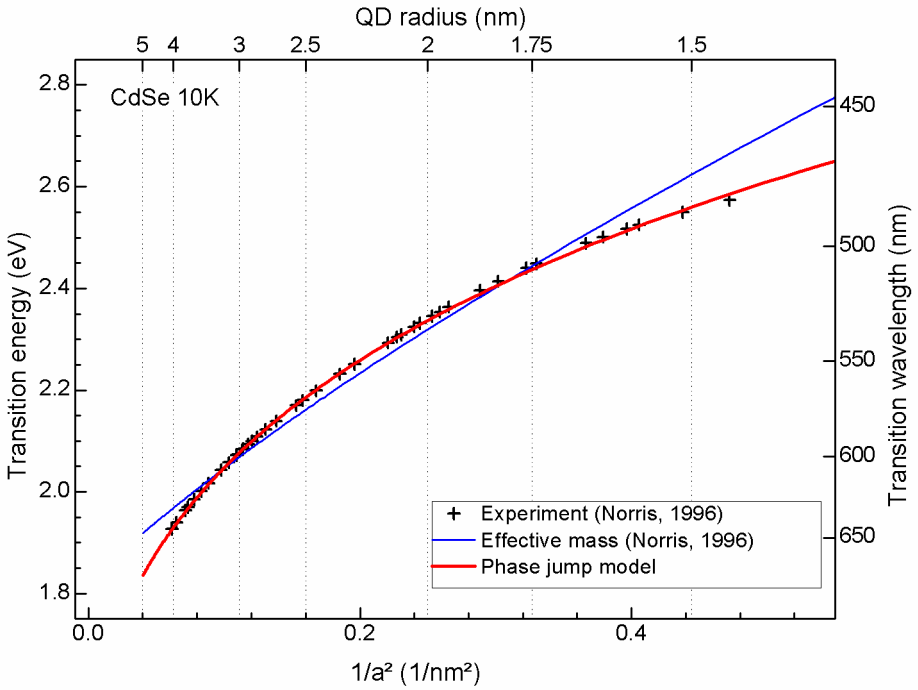

Figure 4.1.: Energy from the first excited state in spherical CdSe nanocrystals as a function of $1/a^2$. Equation 4.2 is fitted with a coefficient of determination 0.9997 for parameters E_0=1.40 eV, γ_ϕ= 2.34 nm, γ_t= 0.60 nm. (Experimental data and effective mass approximation from Ref. [62], courtesy of D. J. Norris).

Transition	E_0 (eV)	γ_ϕ (nm)	γ_t (nm)	R^2
(a)	1.40	2.34	0.60	0.9997
(b)	1.38	2.26	0.37	0.9993
(c)	1.41	2.46	0.42	0.9999
(d)	1.16	4.76	0.83	0.998
(e)	1.51	2.40	0.30	0.995
(f)	0.20	58.0	1.97	0.996
(g)	1.08	13.8	1.42	0.997
(h)	1.25	9.90	0.70	0.995
(i)	1.16	12.2	0.70	0.990
(j)	2.34	-2.63	-3.81	0.989

Table 4.1.: Fitting parameters for CdSe Quantum Dots of Fig. 4.2

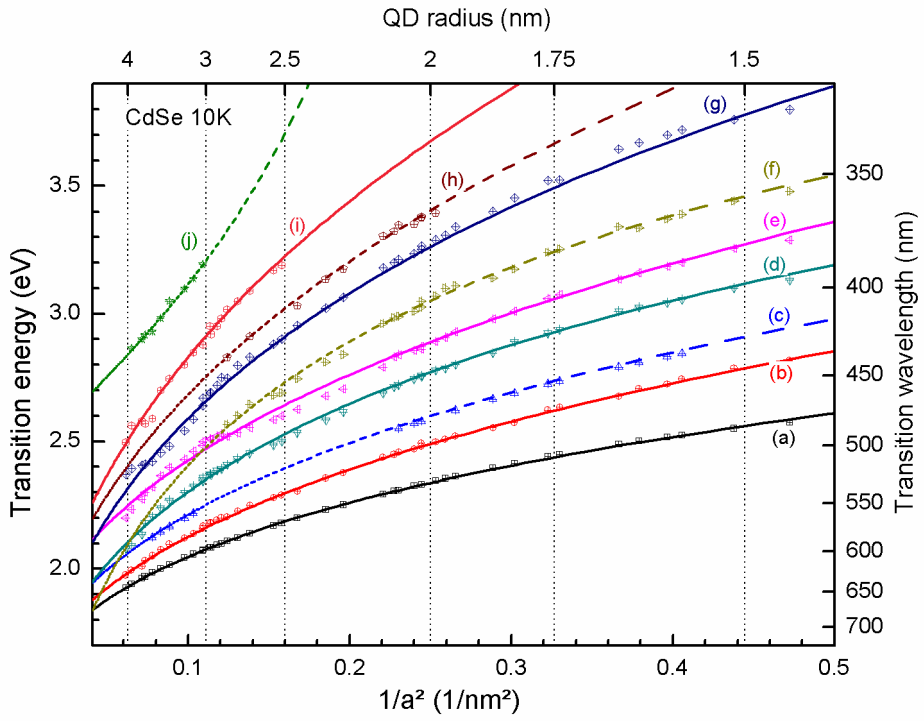

Figure 4.2.: Energy from excitonic transitions (a) to (j) of Ref. [62], versus $1/a^2$, with best fit functions determined from equation 4.2. The output values for parameters E_0 (eV), γ_ϕ (nm), γ_t (nm) and the coefficient of determination R^2 are mentioned in Tab. 4.1. Dotted lines denote weak transitions. (Experimental data, courtesy of D. J. Norris).

Transition	E_0 (eV)	γ_ϕ (nm)	γ_t (nm)	R^2
E1	-0.55	-16.0	4.16	0.999
E2	-0.84	-12.1	4.36	0.998
E3	-0.80	-12.4	3.88	0.998
E4	-0.28	-24.4	2.23	0.999
E5	-0.80	-14.6	4.12	0.999
E6	-1.13	-12.0	4.37	0.998
E7	-7.58	-7.69	21.0	0.997
E8	-31.0	-6.86	70.1	0.996

Table 4.2.: Fitting parameters for InAs Quantum Dots of Fig. 4.3

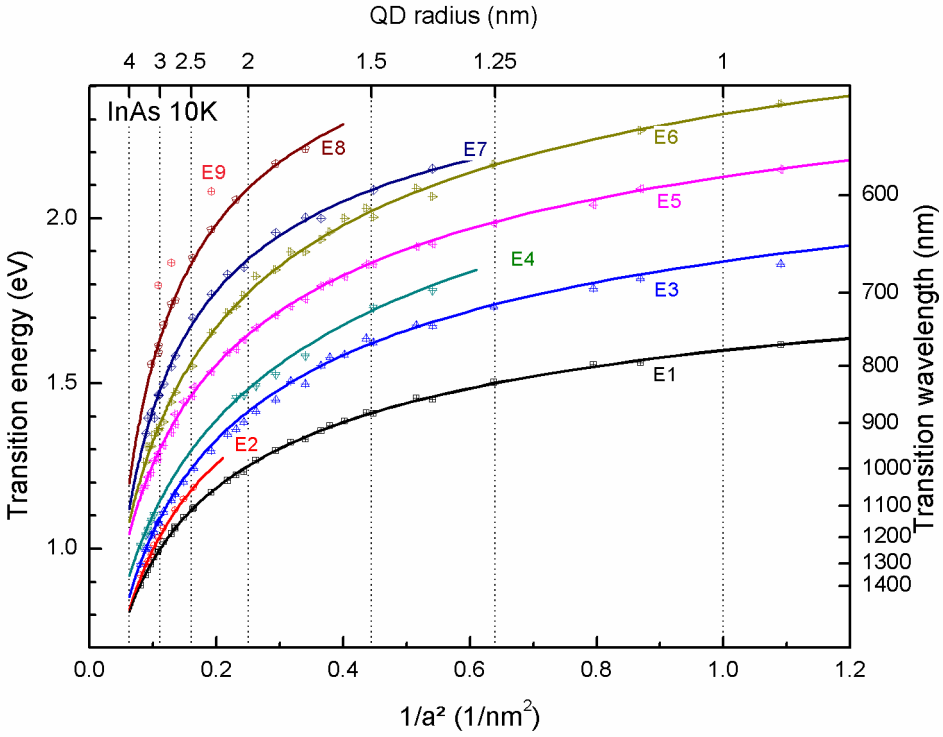

Figure 4.3.: Energy from excitonic transitions E1 to E9 of InAs, plotted as a function of $1/a^2$, with best fit functions determined from equation 4.2. The output values for parameters E_0 (eV), γ_ϕ (nm), γ_t (nm) and the coefficient of determination R^2 are mentioned in Tab. 4.2. (Experimental data for $a > 1.3$nm from Ref. [63], for $a < 1.3$nm, courtesy of U. Banin).

a crystalline structure, it follows a "classical" path: it travels in a right line from atom to atom. In a steady state, $\phi(t) = \omega_a t$, and the action A advances linearly with time at a rate equal to the energy E_a of the electron (see Fig. 4.4) :

$$E_a = \frac{A(t_2) - A(t_1)}{t_2 - t_1} = \frac{\hbar \Delta\phi}{\Delta t} = \hbar\omega_a \tag{4.3}$$

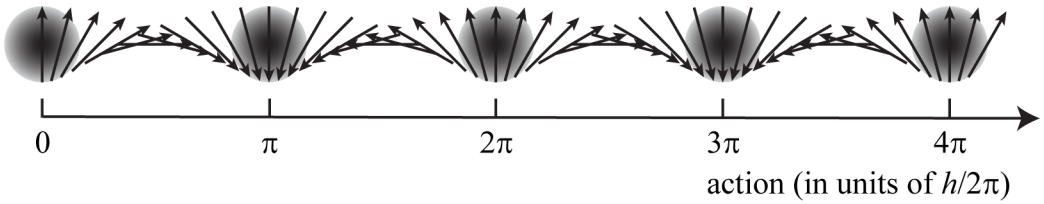

Figure 4.4.: Action carried out by an electron. The electron is represented by a rotating vector (rod) travelling on its path from atom to atom. For simplicity, only one rotational freedom is represented, but its spinning motion must be thought of having two degrees of freedom.

One can think of the rod as a Feynmanian rotating vector or phasor with an energy proportional to its rotation rate [147]. Since the spinning rod associated with the electron moves from atom to atom, equation 4.3 can also be written as $E_a = \frac{\hbar\phi_a}{t_a}$, where ϕ_a is the rod's phase shift and t_a is the delay needed to travel over a distance x_a between two consecutive identical atoms.

The advantage of this heuristic modeling of the electron as a mechanical rod is that it facilitates a visual representation of the particle-wave duality, in a way similar to Maxwell's way of visualizing the electromagnetic lines of force as molecular vortices [159]. It should be seen as a macroscopic analogy which helps to deduce similar laws in another domain. A spinning rod will necessarily evolve in phase with other spinning rods (representing the environing electrons and photons). This phase matching also happens in other mechanistic analogues of quantum mechanics [160]. One could speak of phase matching between a pilot wave and a guided quantum particle [161, 162]. In order to stay in phase with its environment, the guided rod must continuously adapt its spinning velocity. Fig. 4.4 schematically illustrates this progression for a travelling conduction electron in the ideal case, that is an infinite crystalline structure without defects and potential perturbations.

We now analyze the influence of an abrupt interface. When the electron reaches an interface, it may bounce or reflect on it, if not trapped. Upon this reflection, the spinning rod that represents the electron must readapt its phase in order to match phases with the standing wave profile in the new direction, see Fig. 4.5, while its path energy remains the same. This phase jump ϕ_s, performed during a time interval t_s, translates as an increase of the energy of the electron each time it bounces on a surface. In a nanoparticle with small dimensions, the electron bounces with high

frequencies on the nanoparticle surface, which produces phase jumps, and thus an increase of the electron energy, classically seen as quantum confinement.

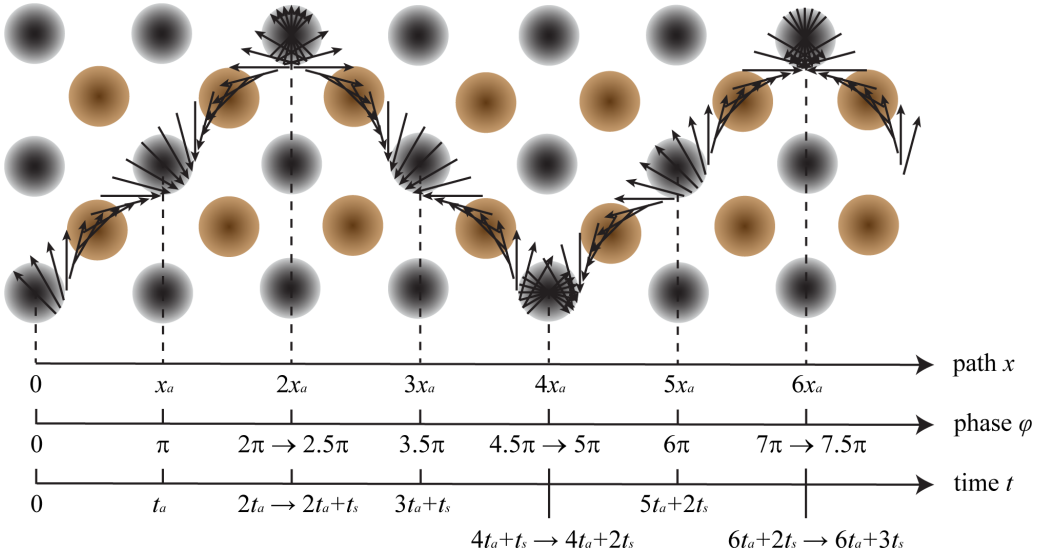

Figure 4.5.: Rotating vector (rod) on its path in a periodical structure. After each traveled path x_a and time interval t_a, a phase jump $\pi/2$ of duration t_s occurs at each reflection.

In a steady state, the rod's angular velocity oscillates between two values: the steady-state bulk value $\omega_a = \phi_a/t_a$ and the quasi instantaneous phase jump value $\omega_s = \phi_s/t_s$ at the surface. The action carried out by an electron that progressed over a distance nx_a along nearest identical atoms and bounced on p interfaces is:

$$A = (n\phi_a + p\phi_s)\hbar \tag{4.4}$$

and the energy associated to this path is:

$$E(n,p) = \frac{n\phi_a + p\phi_s}{nt_a + pt_s}\hbar \tag{4.5}$$

If this phase jump is periodical, such that in between two consecutive bounces on interfaces, the rod travels over a distance nx_a , the average energy is:

$$E(n) = E_a\frac{n+\rho_\phi}{n+\rho_t} \tag{4.6}$$

where $\rho_\phi = \phi_s/\phi_a$ and $\rho_t = t_s/t_a$ are the phase jump and time delay ratios of the rotating vector at the surface with respect to the regular phase and time progression between two nearest identical atoms. Equation 4.6 and 4.2 are mathematically equivalent. In equation 4.6, the number n of atomic distances over which the electron progresses in between two reflections is proportional to the dimension of the nanoparticles.

Equation 4.6 can thus be interpreted as a formula describing the shift in energy of charge carriers due to acceleration or deceleration in the rotation rate of the rotating vector at periodical singularities. In this model of strong confinement, we suppose that the excitonic transitions of both electrons and holes can be described with equation 4.6, and that both charge carriers have the same time delay ratio ρ_t. It results that the electron and hole contributions can be summed up and equation 4.6 can be used for all excitonic transitions under strong confinement. This assumption holds if the masses of the charge carriers cancel out in the ratio ρ_t.

4.1.1.4. Discussion of the parameters

Equation 4.6 has three parameters that we now discuss.

E_a in equation 4.6 corresponds to the energy of the transitions for $n \to \infty$, *i.e.* for the bulk material, including a kinetic energy of the travelling carriers. For the first excitonic transition, this should correspond to the energy gap E_g. However, the fitted reference energies E_0^i obtained by fits of equation 4.2 are considerably smaller than the bulk band-gap energy E_g (except for transition (j)). This discrepancy indicates that the phase jump model can not be extrapolated to the bulk.

The two other parameters in equation 4.6 are related to the phase jump both at the interfaces and between atoms, as well as the time required for these phase jumps. If this approach is valid, these parameters should be identical in identically structured materials whatever the shape of the nanocrystal, provided that the effect of surface chemistry on the phase jumps is identical. We tested this effect with CdSe nanoparticles of different shapes.

Fortunately, CdSe nanocrystals have been synthesized in different shapes including the spheres [61, 112] and more recently the nanoplatelets [123]. The advantage of the nanoplatelets is that they have been shown to be atomically flat with a thickness that is controlled with atomic precision [123]. The crystal structure as well as the crystal orientation of the nanoplatelet facets have been documented, and they have been shown to have pure 1D confinement. They are thus a very interesting object to test this phase jump approach without different fitting parameters.

We hypothesize that the spinning rod associated to a charge carrier bounces back and forth between the two extended (001) surfaces of the nanoplatelet, experiencing a phase jump at each reflection, in analogy to a photon in a Fabry-Perot resonator, as presented in Fig. 4.6. The path we propose is the shortest path for a spinning

rod moving from Cd atom to Cd atom using the nearest atom at each jump. If we transpose this path to a spherical QD, the charge carriers should circle inside the sphere, bouncing 4 times for a complete cycle, see Fig. 4.7.

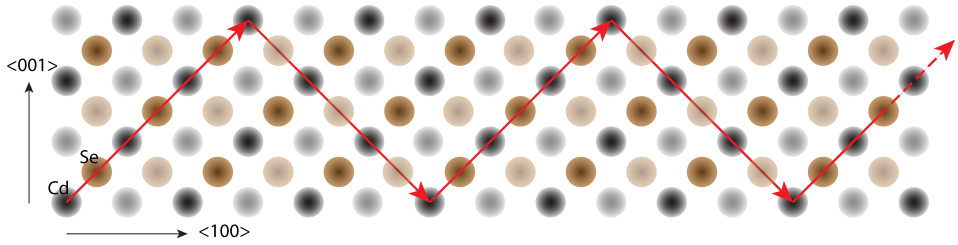

Figure 4.6.: Schematic side view of a zincblende CdSe 3 monolayer nanoplatelet. The excited electron starts along <101> direction. After a phase progression $3\phi_a$, it reflects at the (001) upper surface with phase jump ϕ_s, continues along <1,0,-1> direction, reflects again, *etc.*

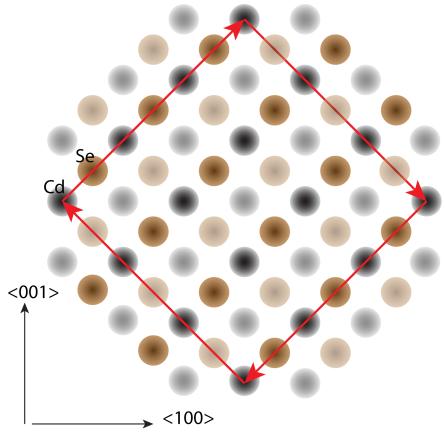

Figure 4.7.: Schematic side view of a zincblende CdSe 3 monolayer radius QD. Electron starts along <101> direction. After a phase progression $3\phi_a$, it reflects at (001) upper surface with phase jump ϕ_s, continues along <1,0,-1> direction, reflects again, continues along <-1,0,-1> direction, reflects again, *etc.*

If such a path holds for spherical QDs, a nanoplatelet with a thickness of n monolayers should have the same transition as a spherical QD with a radius of n monolayers, provided that the two systems have the same nearest neighbor distance, the same composition (and thus the same ϕ_a) and similar surface chemistry (and thus the same ϕ_s).

In Fig. 4.8, we plot the experimental room temperature energy of the first excitonic CdSe transition for nanoplatelets *vs.* their thickness in monolayers [10] and for QDs *vs.* their radius in shell monolayers [112]. The results coincide very well with the

experimental nanoplatelet measurements using HRTEM [144]. The experimental observation that a nanoplatelet with a thickness of n monolayers has its first absorption feature at the same wavelength as a spherical quantum dot with a radius corresponding to n CdSe monolayers is thus confirming the phase jump approach. Such agreement could not be obtained with effective mass approximation.

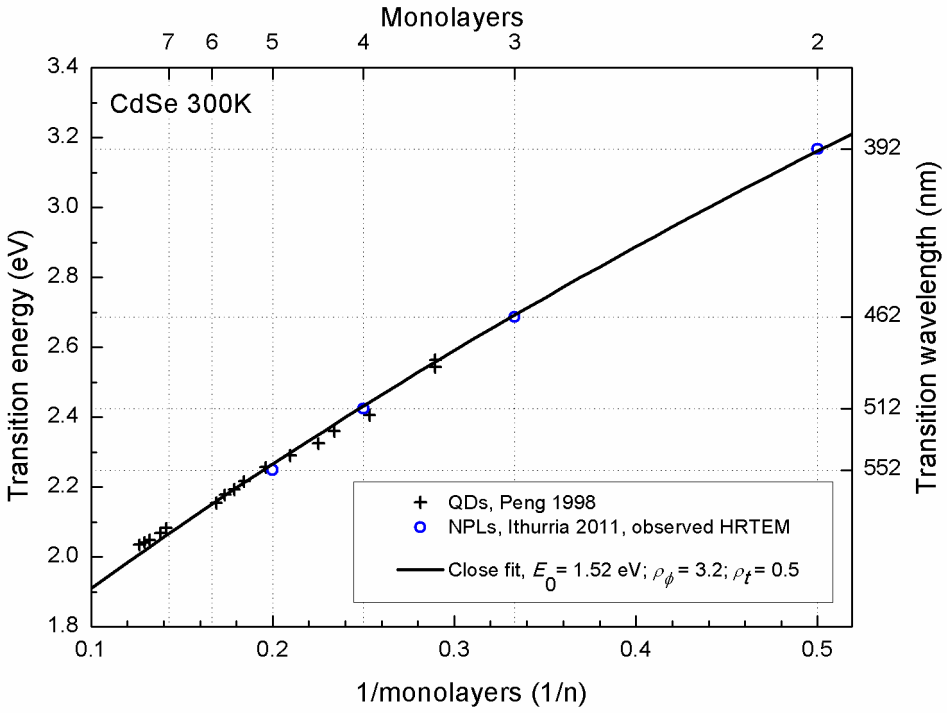

Figure 4.8.: Comparison between first absorption peak of CdSe QDs (crosses) [112] respectively CdSe nanoplatelets (NPLs) (open figures) [10] *vs.* their radii respectively thicknesses expressed in terms of monolayers (the QD literature sizes in nm are divided by 0.304, which corresponds to one monolayer in the zincblende <001> direction). The solid line represents a close fit with $E_a = 1.52$eV, $\rho_\phi = 3.2$, $\rho_t = 0.5$.

We have also compared the energy of the first transition of CdTe spherical QDs [114] with CdTe nanoplatelets [10]. As for CdSe, we first fit the CdTe QDs size dependence using Equation 4.6. We then use their parameters without any change to deduce the thicknesses of CdTe nanoplatelets. The results are reported in Fig. 4.9. While the exact thicknesses of CdTe nanoplatelets have not been obtained by HRTEM yet, we observe a difference of 3 monolayers in thickness estimation compared to EM approximation. Interestingly, the fitting of Equation 4.6 for the first transition of CdSe and CdTe QDs shows that ρ_ϕ and ρ_t are identical for the two materials. Only E_a^1 is different.

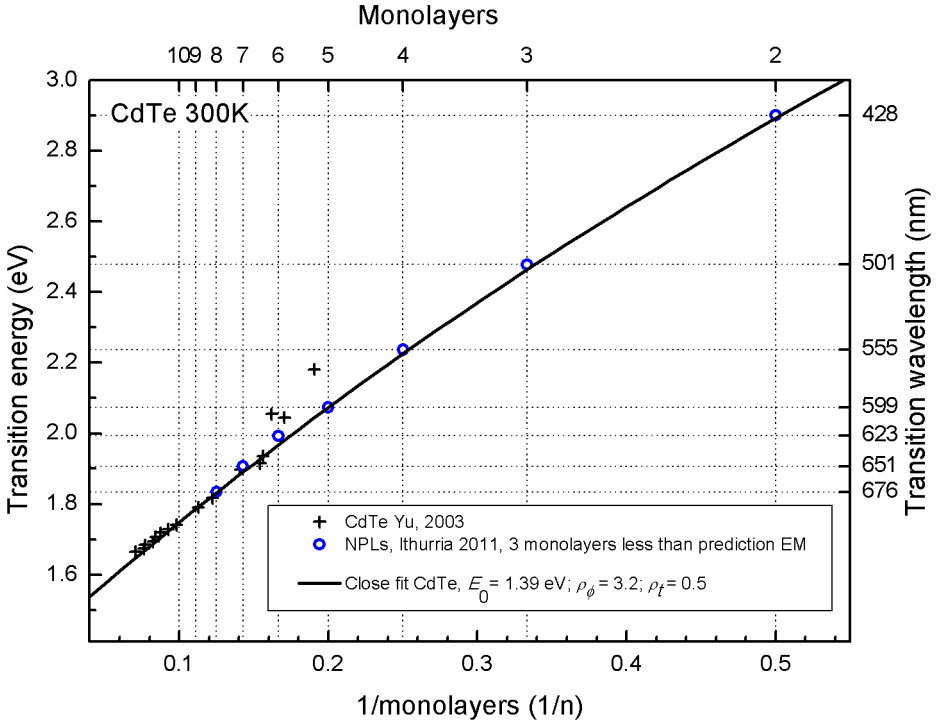

Figure 4.9.: Comparison between first absorption peak of CdTe QDs (crosses) [114] respectively CdSe nanoplatelets (NPLs) (open figures) [10] *vs.* their radii respectively thicknesses expressed in terms of monolayers (the QD literature sizes in nm are divided by 0.324, which corresponds to one monolayer in the zincblende <001> direction). The solid line represents a close fit with $E_a = 1.39$eV, $\rho_\phi = 3.2$, $\rho_t = 0.5$.

4.1.1.5. Intermediate conclusion

We have proposed a simple expression that relates the electronic transitions of semiconductor nanocrystals with their size. This expression has three parameters that are used to fit with a very good accuracy all the excitonic transitions of CdSe, and InAs spherical nanocrystals as well as the excitonic transitions of atomically flat CdSe and CdTe nanoplatelets. We show that this simple expression can be deduced from a phasor representation of the charge carriers in the nanocrystal travelling from atoms to atoms and bouncing on the crystal facets. This simple phase jump model, although semi-empirical, provides a very precise relationship between the size of a nanocrystal and its electronic transitions. It provides a very simple description of all the electronic transitions of the nanocrystals we have investigated, that seems to be accurate at least in the strong confinement regime.

Although this approach is different from classical theoretical description of nanocrystals and is in its very early stages, it can be used to predict successfully the transitions of some nanocrystals. For example, we show that the parameters used to fit the excitonic transitions of spherical CdSe nanocrystals can be used without adjustment to fit the excitonic transitions of CdSe nanoplatelets in the pure 1D confinement regime, as expected in the model.

In the following, we will confront the phase jump approach with other experimental data and discuss the differences with conventional approaches.

4.2. Probing with experimental data

One of the advantages of the presented phase jump approach is the simplicity of the sizing curve formula 4.6. For CdSe nanocrystals, it can be used instead of the empirical formulas 2.1 - 2.5, while maintaining similar values of parameters when we apply it to CdTe nanocrystals. We will now apply the formula to a wider array of nanosystems, in order to discover other invariants.

4.2.1. Quantum dots

4.2.1.1. CdSe spherical quantum dots

When we reported about the synthesis of CdSe cores of different sizes, we represented their first excitonic transition in Fig. 2.6, along with the empirical sizing curves 2.1 - 2.5. We now have an additional sizing curve formula, derived from the phase jump approach. In order to compare the phase jump formula 4.6 to the other empirical sizing curves, we include them all in a new graph together with the experimental data for the synthesized CdSe QDs. As parameter values, we take the ones previously obtained: $E_a = 1.52$eV, $\rho_\phi = 3.2$, $\rho_t = 0.5$. The result is given in Fig. 4.10.

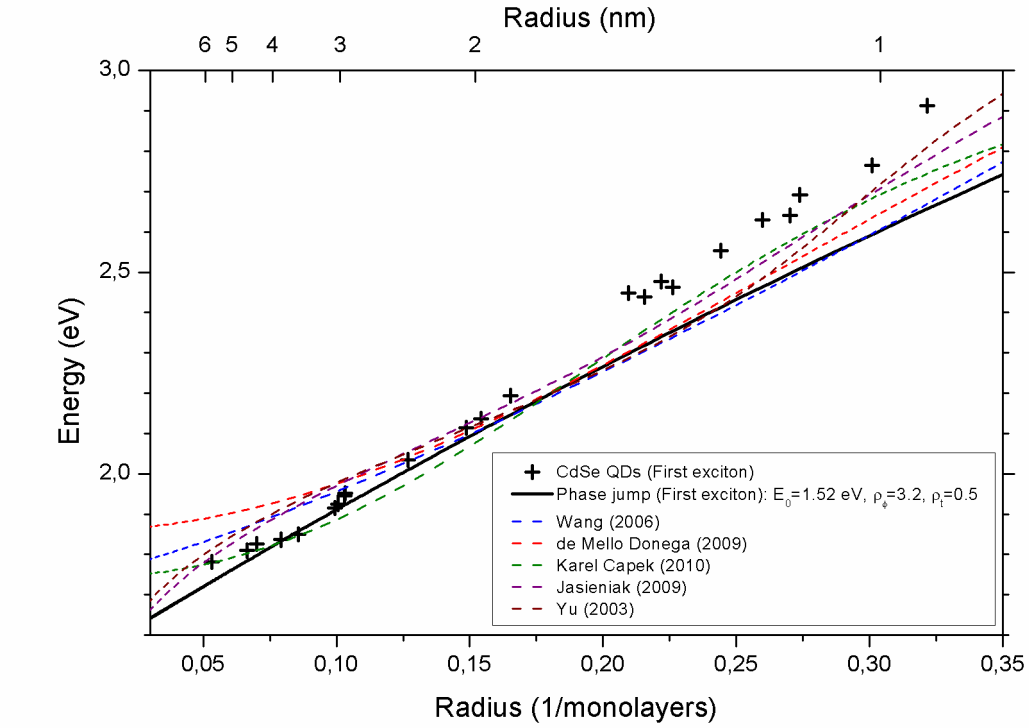

Figure 4.10.: Energy-size dependence of the first excitonic transition of the CdSe quantum dots synthesized in this work, obtained from absorption spectra at room temperature. The phase jump formula 4.6 with previously obtained parameters ($E_a = 1.52$eV, $\rho_\phi = 3.2$, $\rho_t = 0.5$) is drawn in solid line. The fitting expressions 2.1 to 2.5 are drawn in dashed lines for comparison.

Although the phase jump formula 4.6 with the parameters found in the previous section follows the same general trend as the empirical formulas, we observe that it does not fit correctly with the first transition of CdSe QDs synthesized in this research work. The transition energy is systematically underestimated, especially for the smallest QDs. The overall trend of the experimental data is however close to linear, which means that the slope of the phase jump formula can be adjusted to fit to these QDs.

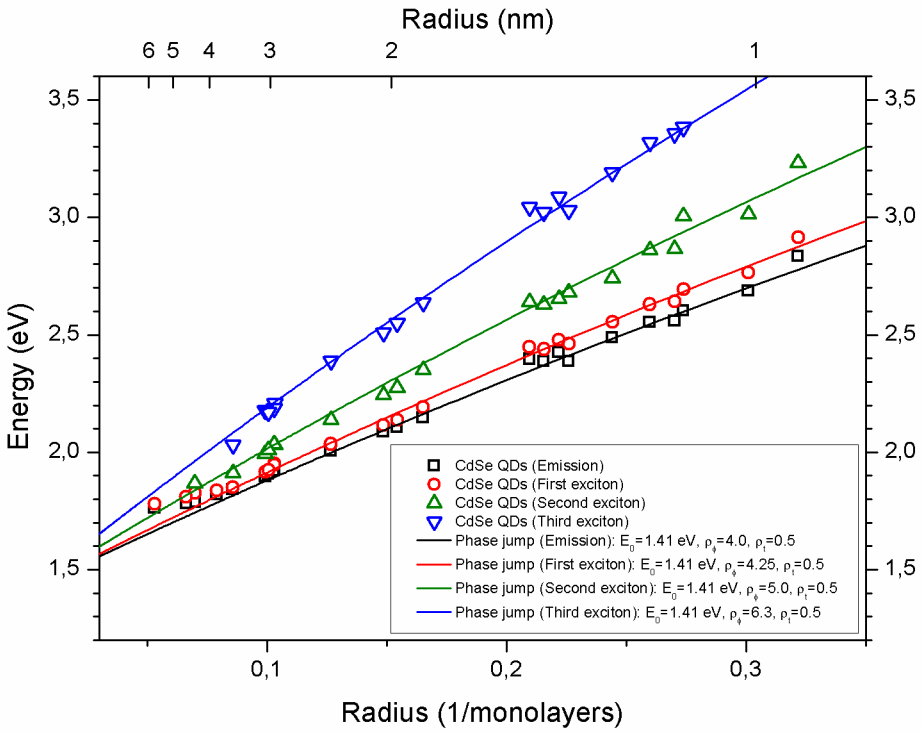

Figure 4.11.: Energy-size dependence of the first excitonic transition of the synthesized CdSe quantum dots at room temperature obtained from emission and absorption spectra. Close fits of the phase jump formula 4.6 are drawn where the reference energy and time delay ratio are kept invariant ($E_a = 1.41\text{eV}$, $\rho_t = 0.5$), while the phase jump ratio varies for each transition (emission $\rho_\phi = 4$, first absorption peak $\rho_\phi = 4.25$, second absorption peak $\rho_\phi = 5$, third absorption peak $\rho_\phi = 6.3$).

In Fig. 4.11, we plot the result of the adjustment. Additional transitions of the QDs are added, with close fits of the phase jump formula. We have adjusted the parameters in order to obtain maximum invariance for the 4 transitions. In that case, we obtain a time delay ratio $\rho_t = 0.5$ and a reference energy $E_a = 1.41\text{eV}$. The fact that the time delay ratio ρ_t can be kept constant with value 0.5 suggests the physical interpretation that the time passed at the surface by the reflecting charge carrier is related to the half cadmium monolayer which coats the QDs at the surface.

In this framework, the three absorption transitions correspond each to a different phase jump of the phasor at the surface.

We also remark in Fig. 4.11 that the phase jump fits are valid only for QD radius smaller than the exciton Bohr radius (~5nm), *i.e.* in the strong confinement range. At radius larger than the exciton Bohr radius, the experimental points are situated at a higher energy.

4.2.1.2. Quantum dots other than CdSe

We have further investigated the excitonic transitions of other II-VI and III-V QDs at room temperature, on the hand of the phase jump equation 4.6, without claim of exhaustivity. Fig. 4.12 and Tab. 4.3 represent the results for transitions of CdS, ZnSe, PbSe, HgTe, InP and InAs. The energy is plotted as a function of inverse radius monolayers. The experimental data are taken from the literature (see sec. A.2 for details).

Material	Monolayer thickness (nm)	Transition	E_a (eV)	ρ_ϕ	ρ_t	E_s(eV)
CdS	0.291	First	2.15	3.2	0.5	0
		Second	2.15	4.7	0.5	0
		Third	2.15	6.2	0.5	0
ZnSe	0.2835	First	1.52	3.2	0.5	1.05
		Second	1.52	3.2	0.5	1.52
HgTe	0.323	First	2.02	3.2	0.5	-2.02
PbSe	0.306	First	2.55	3.2	0.5	-2.55
InP	0.293	Emission	1.01	5.3	0.5	0
		First	1.01	6.4	0.5	0
		Second	1.01	8.7	0.5	0
		Third	1.01	11	0.5	0
InAs	0.303	Emission	0.51	44	8.2	-0.62
		First	0.51	45.4	8.2	-0.62

Table 4.3.: Monolayer thickness and parameter values for the fits of Fig. 4.12.

We have tried to preserve phase delay and time delay ratios $\rho_\phi = 3.2$ and $\rho_t = 0.5$ in all cases. In the strong confinement ranges, this has been possible for the investigated II-VI transitions, under the condition that the phase jump equation 4.6 should be completed with a relative energy shift E_s, giving the following modified phase jump sizing curve:

$$E(n) = E_a \frac{n + \rho_\phi}{n + \rho_t} + E_s \tag{4.7}$$

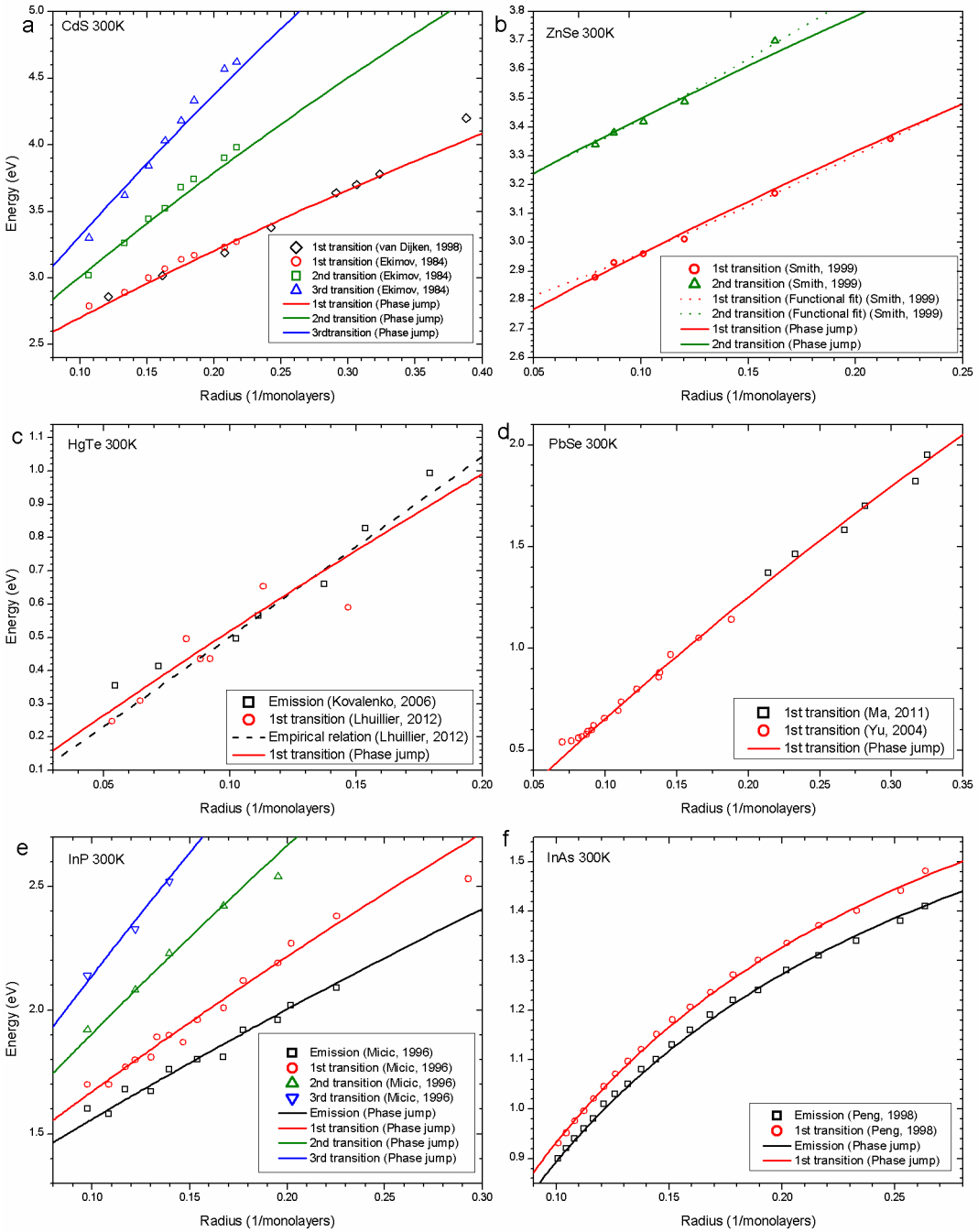

Figure 4.12.: Energy-size dependence of the various transitions for various QDs, taken from the literature. Close fits of phase jump formula 4.7 are drawn in solid lines. The number of radius monolayers is calculated as half the zincblende lattice constant. From left to right and from top to bottom: (a) CdS [163, 164]. (b) ZnSe [165]. (c) HgTe [166, 167]. (d) PbSe [168, 169]. (e) InP [170]. (f) InAs [112]. Monolayer thicknesses and parameter values are mentioned in Tab. 4.3. Experimental values are detailed in sec. A.2.

This extra energy shift adds an extra degree of liberty to the procedure of curve fitting, although we have not succeeded in giving a clear physical meaning in the framework of the phasor approach. The obtained parameter values should thus be taken with care. The degree of confidence of the fits also depends on the experimental conditions in which the data have been obtained. These vary for each material and experiment.

For CdS, the data from Ekimov *et al.* have been obtained on QDs in a glass matrix [163]. The QDs from Van Dijken *et al.* [164] result from photo-etching of QDs that have initially the same size. The energy values of the first absorption transition in both cases is taken at the absorption edge, whereas the values for the second and third exciton are taken at the maximum of oscillation. This lowers the confidence of the obtained parameter values. Nonetheless, as a curiosity, we remark that $\rho_\phi^{(2)} \approx \frac{3}{2}\rho_\phi^{(1)}$ and $\rho_\phi^{(3)} = 2\rho_\phi^{(1)}$.

For ZnSe, the phase jump fits of the first and second absorption transition closely follow the functional fits determined by Smith *et al.* [165] in the experimental range. Extra experimental data are needed to test both approaches. We remark that the constraint $\rho_\phi = 3.2$ and $\rho_t = 0.5$ requires a non-zero energy shift E_s in the completed phase jump equation 4.7 and yields a reference energy E_a identical to the one obtained for CdSe QDs and nanoplatelets.

For the low bandgap material HgTe, experimental determination of the excitonic transitions is more difficult and this adds more uncertainty in the experimental data. Applied to data of Kovalenko *et al.* [166] and Lhuillier *et al.* [167], for the constraint $\rho_\phi = 3.2$ and $\rho_t = 0.5$, a negative energy shift E_s is required. The phase jump approach gives an equation that, in the experimental range, closely follows the equation determined by Lhuillier *et al.* that was based on the $k.p$ relation for the heavy-hole and conduction band term.

For PbSe, like for HgTe, applied to data of Yu *et al.* [168] and Ma *et al.* [169], the constraint $\rho_\phi = 3.2$ and $\rho_t = 0.5$ requires a negative energy shift E_s which has the same absolute value as the reference energy E_a . The phase jump approach only fits experimental data in the range of stronger confinement. Departure from experiment takes place for radii greater than 15 monolayers radius (about 5 nm), long before it reaches the exciton Bohr radius, which is about 45 nm.

For the first excitonic transition of the III-V InP QDs of Micic *et al.* [170], we could not retrieve a close fit with $\rho_\phi = 3.2$ and $\rho_t = 0.5$. Yet constraining $\rho_t = 0.5$, we obtain a phase shift ratio twice the value obtained for the II-VI materials, *i.e.* $\rho_\phi = 6.4$. The other transitions then require an adjustment of the phase shift ratio.

For the transitions of InAs QDs of Peng *et al.* [112], it is not possible to obtain a close fit with one of the constraints $\rho_\phi = 3.2$ or $\rho_t = 0.5$ or even $E_s = 0$. Freeing these constraints gives numerous possible sets of parameter values. In Fig. 4.12 and Tab. 4.3, we have represented the values for the smallest time delay ratio.

Overall, we have shown, through the application of the phase jump equation 4.7,

that this approach leads to reusable QD sizing curve formulas, which need only small parameter adjustments for a wide array of materials.

4.2.2. Nanoplatelets

4.2.2.1. Comparing CdS, CdSe and CdTe nanoplatelets

In sec. 4.1.1.4, we noticed that the first excitonic energy levels of CdSe and CdTe QDs of radius n monolayers are nearly equal to the equivalent levels of CdSe and CdTe nanoplatelets of thickness n monolayers. Surprisingly, the same numerical values for the phase jump and time delay ratios ($\rho_\phi = 3.2$ and $\rho_t = 0.5$) can apply to QDs and nanoplatelets.

If we fit equation 4.6 to the CdS nanoplatelet data with the same constraints ($\rho_\phi = 3.2$ and $\rho_t = 0.5$), we obtain a close fit with $E_a = 2.02$eV, see Fig. 4.13 (a) in which we have also drawn the results for CdSe and CdTe nanoplatelets. The number of predicted CdS monolayers is reduced by 1 with respect to previous EMA predictions [10].

The fit with the experimental data is however not as good as for CdSe and CdTe. This could be accounted by the fact that the experimental values have been obtained for CdS nanoplatelets with small lateral extension. HRTEM imaging is required to verify the thickness predictions for CdS. Overall, straightforward application of the phase jump model predicts a smaller thickness than EMA (of 1, 2 and 3 monolayers respectively for CdS, CdSe and CdTe nanoplatelets).

Another feature which distinguishes EMA from the phase jump approach is that the sizing curves for the first absorption peak of CdSe and CdTe cross each other in EMA, while they remain distinct in the phase jump model. In Fig. 4.13 (b), we have plotted EMA size predictions for CdS, CdSe and CdTe. We notice the crossing of the sizing curves for CdSe and CdTe at 7 monolayers.

4.2.2.2. Lateral extension of nanoplatelets

Except for the thickness, the width and length of nanoplatelets also play a role in the confinement energy of the first excitonic absorption peak. Experimentally, this has been verified in the group. Some of the data presented by Ithurria et al. in Ref [10] refer to small nanoplatelets. When they are grown in width and length to extents which may reach several hundreds of nm, the peak energies differ by some meV from those of the smaller nanoplatelets and tend to a limit value.

We will first deduce the shift in energy due to lateral extension in the framework of the phase jump interpretation. We will then put to the test the predicted shift using experimental data obtained at room temperature from absorption spectra for 5 monolayer CdSe nanoplatelets, by Mickaël Tessier [171].

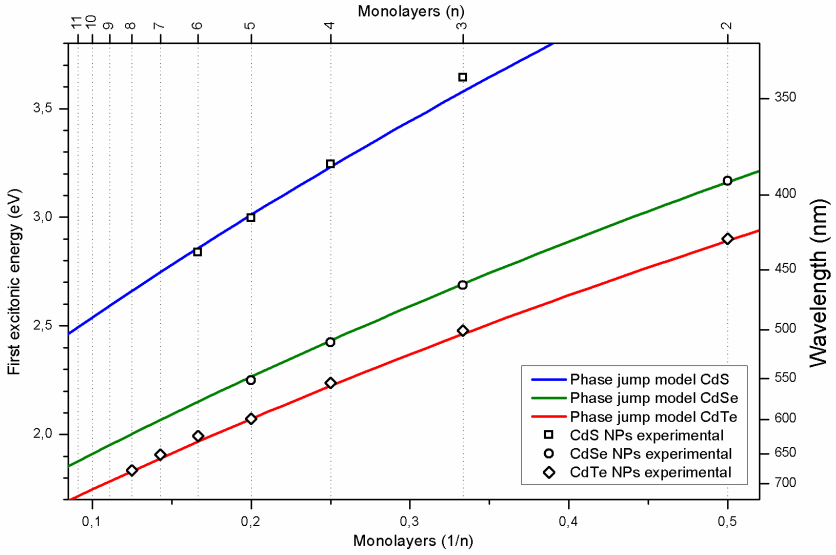

(a)

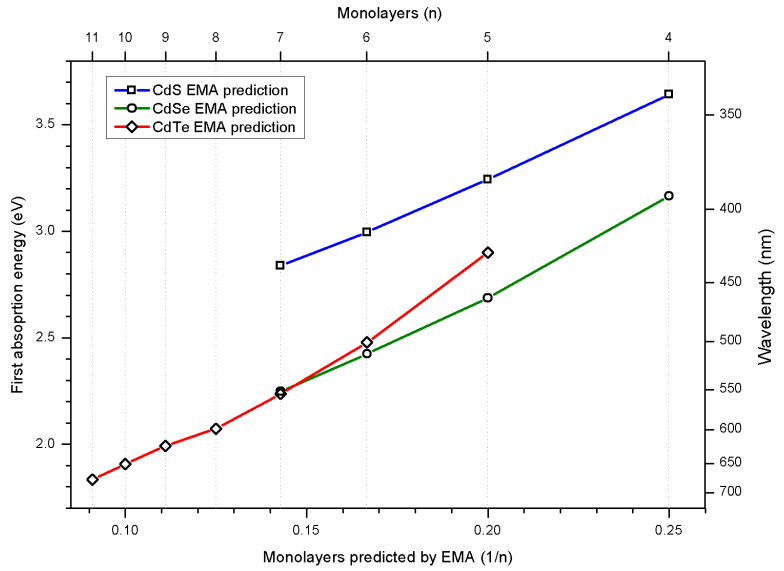

(b)

Figure 4.13.: First excitonic peak energy of CdS, CdSe and CdTe nanoplatelets plotted as a function of the inverse number of monolayers: (a) with size predicted by the phase jump model, where the phase jump and time delay ratios are equal for the three materials ($\rho_\phi = 3.2$ and $\rho_t = 0.5$) and E_a is respectively 2.02, 1.52 and 1.39 eV. (b) with size predicted by effective mass approximation [10] (lines are plotted as a visual guide).

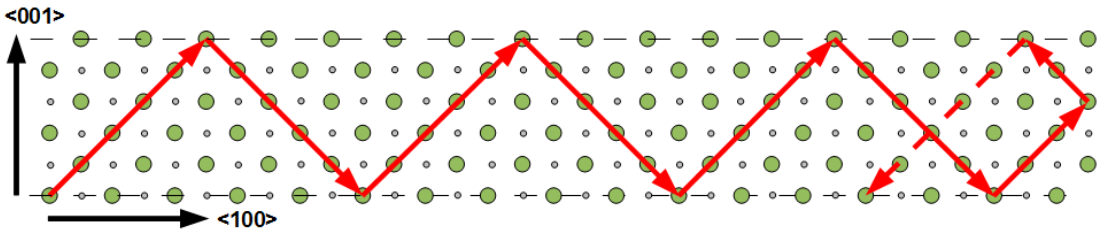

Figure 4.14.: Schematic representation of a 5 monolayer nanoplatelet of length 33 monolayers. The continuous zig-zagging arrow indicates the bouncing path of an electron in the conduction band.

In sec. 4.1.1.4, we have seen that when we apply the phase jump model to the zincblende CdSe and CdTe nanoplatelets, the lowest absorption energy results from the charge carriers bouncing back and forth on the (001) extended surfaces. Because the oscillation strength in the thickness direction largely overshadows the oscillation strength in the width and length directions, the direction of motion is assumed to be along the <101> and equivalent <-101>, <011>, <0,-1,1> following the nearest cation-cation directions. The paths of the charge carriers along <110> and equivalent directions perpendicular to the thickness direction require a much higher action due to the dominant perpendicular oscillations. However, when the charge carriers reach a lateral facet on their path, they will undergo an additional reflection on that (100) or (010) facet, see Fig. 4.14. This means that the number of reflections p in equation 4.5 must take into account this extra reflection. Let us detail this process formally.

Upon absorption of a photon, we assume that the electron will be set in motion with equal probability in the length or width direction, as the nanoplatelet is randomly oriented in the solution or on the substrate. We may write this process in terms of state vectors (ignoring the hole for the case of simplicity). We start with an initial state composed of an incoming photon and an electron in the valence band:

$$|\Psi_i\rangle = |1\rangle\,|e_v\rangle \tag{4.8}$$

The excited state may be written as an absorbed photon and an electron in the conduction band which, while it is bouncing between the lower and upper surfaces is either travelling in the length x-direction or in the width y-direction:

$$|\Psi_e\rangle = |0\rangle\,(a_c^x\,|e_c^x\rangle + a_c^y\,|e_c^y\rangle) \tag{4.9}$$

The a_c's denote the complex amplitudes of the travelling electron and include an exponential $e^{i\omega t}$ representing the angular velocity of the phasor. On average, the

phasor of the electron travelling in the length direction has a smaller angular velocity as the one for the electron travelling in the width direction, because it undergoes less phase jumps. The lowest energy peak of the absorption spectrum will thus result from electrons travelling in the length direction, while electrons travelling in the width direction will contribute to a peak at higher energy.

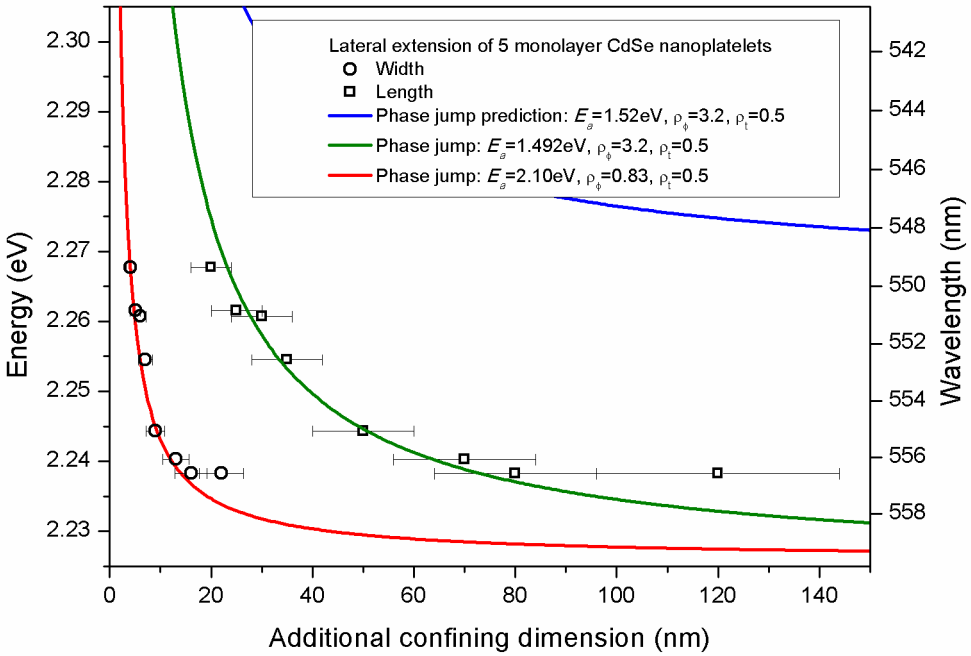

Figure 4.15.: Energy of the first absorption peak of 5 monolayers CdSe nanoplatelets upon lateral extension. The blue line represents the phase jump prediction without any adjustment of parameters ($E_a = 1.492$eV, $\rho_\phi = 3.2$, $\rho_t = 0.5$). The green line represents the phase jump close fit for the length direction with slight adjustment of the reference energy ($E_a = 1.52$eV), while the phase jump and time delay ratio are constrained to $\rho_\phi = 3.2$ and $\rho_t = 0.5$. The red line represents the phase jump close fit for the width direction with adjustment of all parameters ($E_a = 2.10$eV, $\rho_\phi = 0.83$ and $\rho_t = 0$). The number of monolayers has been multiplied by 0.304, which in nm corresponds to one monolayer in the zincblende <100> direction. Experimental data for room temperature first absorption energies have been communicated personally, courtesy of Mickaël Tessier [171].

Let us denote n_t and n_l the number of monolayers in the thickness and length direction of the nanoplatelet. From one side to the other in the length direction of the nanoplatelet, while travelling over a distance of n_l cadmium-cadmium distances, the charge carrier bounces $(1 + \frac{n_l}{n_t})$ times. Equation 4.5 should thus be adapted in

the following way:

$$E(n_t, n_l) = E_a \frac{n_l + (1 + \frac{n_l}{n_t})\rho_\phi}{n_l + (1 + \frac{n_l}{n_t})\rho_t} \tag{4.10}$$

Fig. 4.15 represents the experimental data for width and length of the nanoplatelets and compares it to the phase jump prediction with $E_a = 1.52$eV, $\rho_\phi = 3.2$ and $\rho_t = 0.5$ (blue curve). We remark that this prediction doesn't fit neither for the width nor for the length of the observed nanoplatelets. In order to fit the experimental data with the phase jump equation 4.10. Under the constraint $\rho_\phi = 3.2$ and $\rho_t = 0.5$, it is possible to adjust slightly the reference energy to a value $E_a = 1.492$eV for the experimental lengths of the nanoplatelets (green curve), while this is impossible for the widths. Fitting to the width is only possible with an adjustment of two parameters. For example, under the constraint $\rho_t = 0.5$, we retrieve a close fit with the parameters $E_a = 2.1$eV and $\rho_\phi = 0.83$ (red curve). For a complementary verification of the phase jump approach applied to the lateral extension of nanoplatelets, experimental data for nanoplatelets of different thickness or material are required.

We remark that for nanoplatelets whose width×length dimensions are larger than 16×80 nm, the energy remains constant. A possible explanation in the framework of the phase jump approach is that above this length, quantum coherence is lost over the whole nanoplatelet and the carriers will thus undergo additional reflections, because they hardly never travel in the straight length direction.

We could not compare the phase jump predictions to EMA predictions, which is in a preliminary stage.

4.2.3. Nano-objects with 2D confinement

Any quantum confinement theory should give good predictions not only for 3D and 1D confined objects but also for 2D confined objects like nanorods and nanowires. A nanowire is the ideal 2D confined object, the nanorod being intermediate between the nanowire and the QD.

We can think of a nanorod as a set of quantum dots aggregated along one direction, see Fig. 4.16. For fully grown nanorods, the diameter is of course smoothly constant over the whole length. Most of the nanorods and nanowires are grown in the hexagonal wurtzite structure, because the <001> c-axis favors anisotropic growth along its axis. However, some nanowires have also been reported in zincblende phase [172, 173, 174]. For the sake of simplicity, the figure considers the zincblende cubic structure. When a carrier travels in the length direction along the nanorod, it will undergo a reflection every n cation, where n is the number of equivalent monolayers in diameter until it reaches the end of the nanorod. At that end, it undergoes an extra reflection, as for incompletely extended nanoplatelets. The relevant spatial

periods for the travelling carriers in the nanorods are thus the diameter and the length.

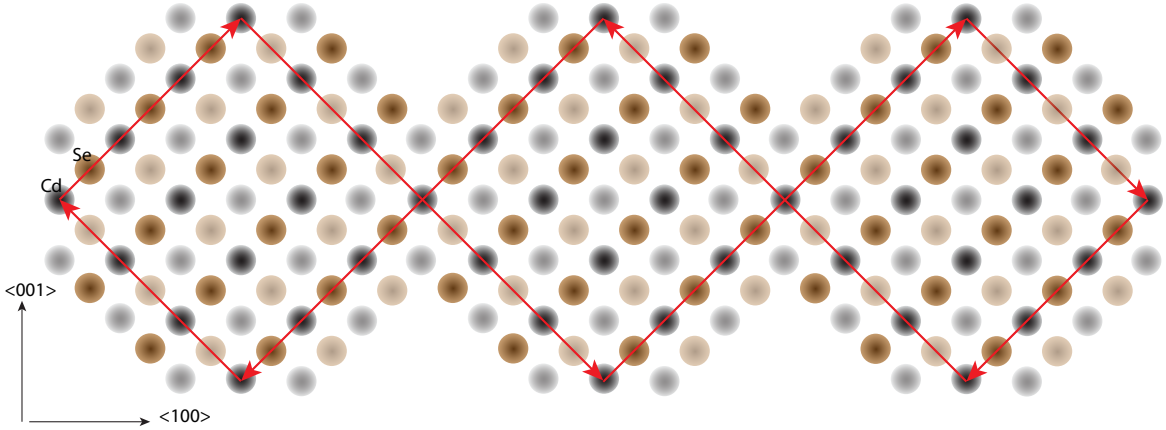

Figure 4.16.: Nanorod of aspect ratio $A = 3$ represented as aggregated quantum dots. The continuous zig-zagging arrow indicates the bouncing path of an electron in the conduction band.

We notice here that this phase jump interpretation runs into trouble, because the straightforward prediction would be that a nanorod with diameter d has the same excitonic first transition as a nanoplatelet with same thickness. This is however not the case experimentally [175]. We will continue in order to see if the phase jump approach could be applied with a minor adjustment in parameters. Similarly to the derivation of equation 4.5 for incompletely extended nanoplatelets, and charge carriers bouncing with an angle of 45° on the surface, the phase jump formula for nanorods can be stated in the following way:

$$E(n_d, A) = E_a \frac{A.n_d + (1 + A)\rho_\phi}{A.n_d + (1 + A)\rho_t} \tag{4.11}$$

where n_d is the number of diameter monolayers and A is the aspect ratio of the nanorod.

4.2.3.1. Nanowires

We will begin to confront equation 4.11 to experimental data of nanowires. With high aspect ratio, we have $A \approx 1 + A$, and the aspect ratio cancels out, retrieving equation 4.6 for nanowires. The dependence of the emission transition on the diameter of CdSe nanowires has been investigated by Yu *et al.* [176]. We present the experimental data in Fig. 4.17 along with a close fit of the phase jump formula with the usual constraints on the phase jump and time delay ratio ($\rho_\phi = 3.2$, $\rho_t = 0.5$).

The reference energy E_a required an adjustment to 1.67 eV. The least squares best fit of Yu *et al.* with formula $E = 1.74 + 1.76/d^{1.36}$ is also drawn for comparison. The phase jump fit departs from the experimental values and from the least squares fit with exponent 1.36 for nanowires of radius larger than the exciton Bohr radius. The agreement of the phase jump equation, although within the limits of the experimental uncertainty for a diameter smaller than 10 nm, is not as good as the least squares best fit. It would be of interest to have more experimental data.

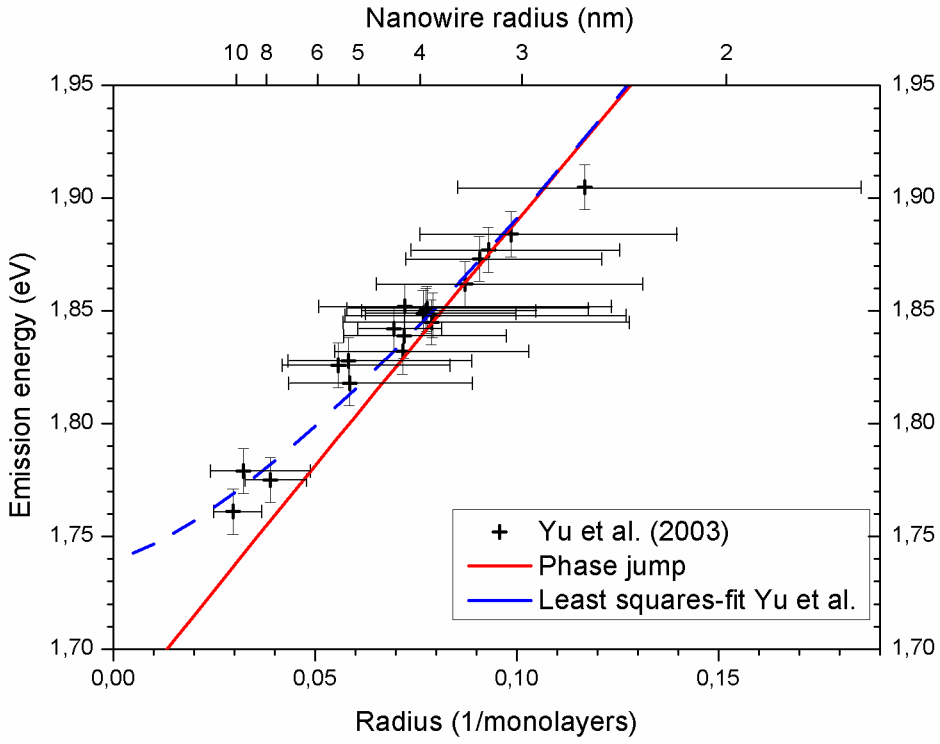

Figure 4.17.: Energy of the emission peak of CdSe nanowires as a function of the radius. The number of monolayers has been obtained dividing the radius in nm by 0.304, which corresponds to one monolayer in the zincblende <100> direction. The solid line represents equation 4.11 with $E_a = 1.67$eV, $\rho_\phi = 3.2$, $\rho_t = 0.5$. The experimental data and least squares best fit $E = 1.74 + 1.76/d^{1.36}$ are taken from Ref. [176].

4.2.3.2. Nanorods

The dependence of the emission transition on the diameter and length of CdSe nanorods has been investigated by Li *et al.* [177]. In Fig. 4.18, we confront the experimental data of Li *et al.* to the prediction of equation 4.11 instantiated with the parameters value $E_a = 1.67$eV, $\rho_\phi = 3.2$ and $\rho_t = 0.5$ obtained for the nanowires. While the polynomial best fit standard deviation obtained by Li *et al.* is ~30 meV,

the standard deviation for the phase jump adjustment is 40.9 meV, which is a reasonable value for a linear fit. We may thus assume that equation 4.11 correctly takes into account the influence of the aspect ratio for nanorods.

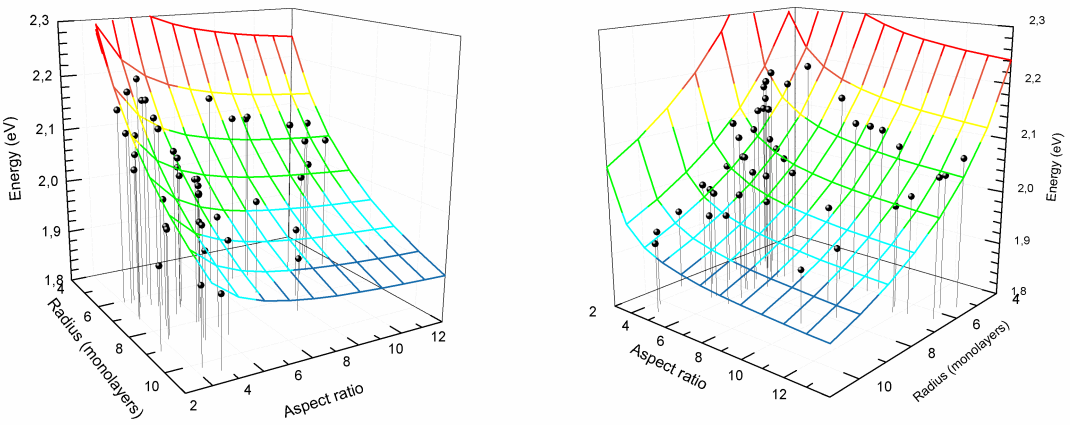

Figure 4.18.: Energy of the emission peak of CdSe nanorods as a function of both radius and aspect ratio viewed from two different angles. The number of monolayers has been obtained dividing the radius in nm by 0.304, which corresponds to one monolayer in the zincblende <100> direction. The plotted mesh represents equation 4.11 with $E_a = 1.67$eV, $\rho_\phi = 3.2$, $\rho_t = 0.5$. The experimental data are taken from Ref. [177].

4.2.3.3. Aggregated quantum dots

In sec. 2.3.3.3, we suggested that the oriented attachment of aggregated QDs forming small nanorods of aspect ratio 2 - 5 accounted for a secondary emission peak at the low energy side of the QD emission peak. We will now verify this suggestion on the hand of the phase jump model.

For the CdSe QDs synthesized in this work, we have determined the wavelengths of the primary and secondary emission peaks through pointing at the maximum intensity values in the emission spectra. The values are given in Tab. A.4 in sec. A.1. With the energy value E_m of the emission peak, we determine the QD radius with the size-energy dependence based on the phase jump equation 4.6:

$$n = E_a \frac{\rho_\phi - \rho_t}{E_m - E_a} - \rho_t \tag{4.12}$$

We use the parameter values obtained through the fitting of Fig. 4.11: $E_a = 1.41$eV, $\rho_\phi = 4.0$, $\rho_t = 0.5$. The resulting sizing curve with both emission peaks are represented in Fig. 4.19, together with the phase jump model predictions for the emission

peak of nanorods of aspect ratio 2 and 5, for the same parameters values. We remark that the secondary emission peak is situated between the predicted nanorod emission peaks for aspect ratio 2 and 5, although the trends followed by the energy shifts are not the same. Further investigation is needed to determine if this secondary peak is related to nanorods or simply spherical aggregates of QDs.

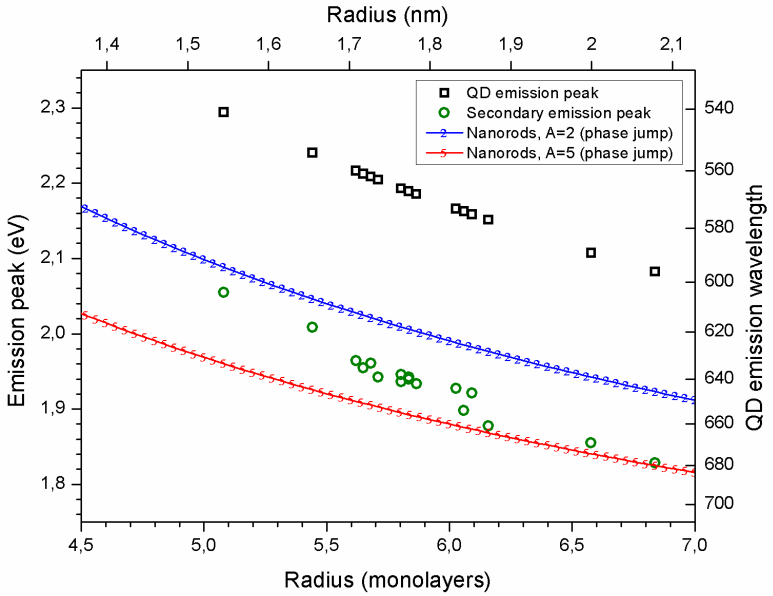

Figure 4.19.: Energy of the primary and secondary emission peak of the solution of CdSe QDs synthesized in this research work. The sizes are estimated through application of the phase jump equation 4.12. The phase jump prediction for nanorods of aspect ratio 2 and 5 formed through aggregation of QDs is indicated for comparison. The number of monolayers has been obtained dividing the radius in nm by 0.304, which corresponds to one monolayer in the zincblende <100> direction.

4.2.4. Cathodoluminescence of semiconductor nanocrystals

The effect of quantum confinement on the luminescence spectrum is usually investigated with photoluminescence spectrometry. In sec. 3.3.3.3, we have reported that the cathodoluminescence emission peak of core-shell CdSe/CdS QDs has the same energy as the photoluminescence emission peak. Combined with TEM imaging, cathodoluminescence spectroscopy has the advantage of giving access to the luminescence spectrum while spatially resolving the size and shape of single nano-objects. This enables determination of the energy-size dependence of the confined transitions at nanometer spatial resolution, without being disturbed by the size dispersion in ensembles of nanocrystals.

The first cathodoluminescence experimental study of the effect of quantum confinement at spatial monolayer precision has been reported by Zagonel *et al.* [136]. They measured the emission energy of tightly packed Si-doped GaN quantum disks separated by AlN quantum disks along nanowires that were grown by molecular beam epitaxy. The thickness of the quantum disks has been determined at monolayer precision with HRTEM.

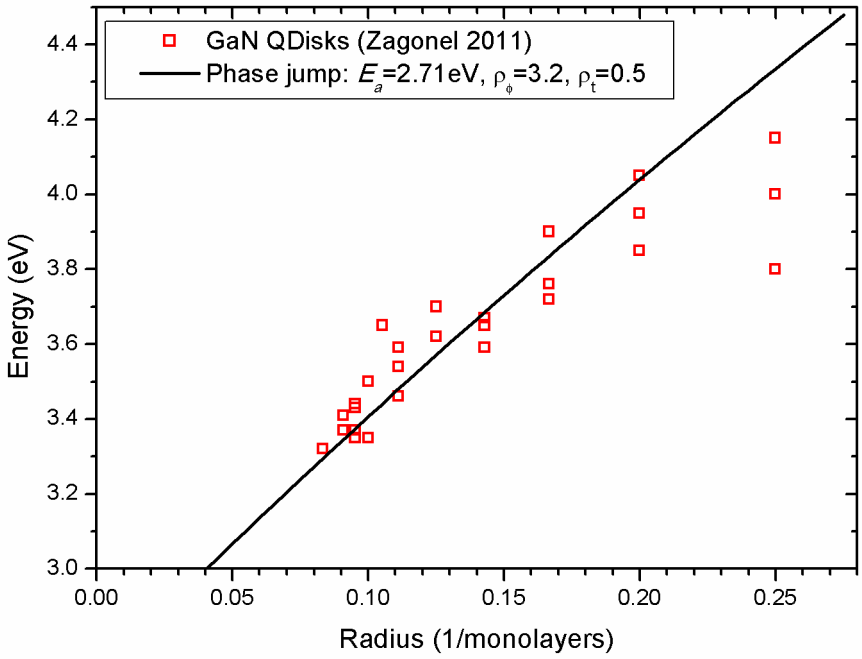

Figure 4.20.: Energy of the cathodoluminescence peak of GaN quantum disks embedded in a GaN/AlN nanowire as a function of the thickness. The solid line represents equation 4.6 with $E_a = 2.71$eV, $\rho_\phi = 3.2$, $\rho_t = 0.5$. The experimental data are taken from Ref. [136].

Fitting of the experimental energy-size dependence to the phase jump equation 4.6 under the constraints $\rho_\phi = 3.2$, $\rho_t = 0.5$ gives a reasonable result for $E_a = 2.71$eV. This result is presented in Fig. 4.20. We remark a departure from the phase jump equation for the thinnest disks. This could however be related to the dispersion in energy values due to non constant diameter of the quantum disks along the nanowire or to different compressive strains by the AlN shell, as indicated in the experimental report [136].

As a last application of the phase jump approach, we consider cathodoluminescence experiments performed by Chen *et al.* on ZnO nanorods outside of the strong confinement regime [178]. The nanorods have been grown through H_2 post-treatment of ZnO films on a Si substrate. They have a radius ranging from 25 to 90 nm, which is

far larger than the exciton Bohr radius of ZnO ($\approx$ 5nm) and they have a high aspect ratio. The cathodoluminescence energy is observed to shift to higher values upon decrease of the nanorod diameter. This shift is attributed to a surface effect due to increased surface to volume ratio and a $\triangle E_g = 1/d$ relationship of the bandgap shift upon diameter has been established. Fitting of the experimental energy-size dependence to the phase jump equation 4.6 under the constraints $\rho_\phi = 3.2$, $\rho_t = 0.5$ gives a very good result for $E_a = 3.28$eV, see blue line presented in Fig. 4.21.

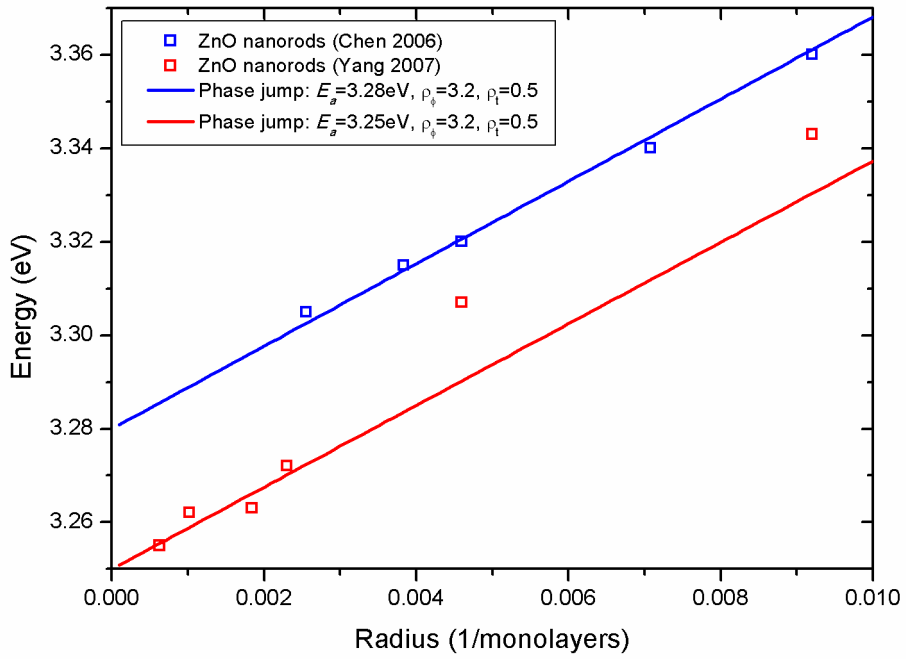

Figure 4.21.: Experimental values of the cathodoluminescence peak for ZnO nanorods [178] and along a ZnO nanowire [179] as a function of the radius. The blue line represents equation 4.6 with $E_a = 3.28$eV, $\rho_\phi = 3.2$, $\rho_t = 0.5$. The red line represents equation 4.6 with $E_a = 3.25$eV, $\rho_\phi = 3.2$, $\rho_t = 0.5$.

Additional investigation was performed by Yang *et al.* [179] on a single pencil-like ZnO nanowire whose radius gradually decreased from 365 to 50 nm along its length direction. They confirmed the shift in energy and attributed it to the Burstein-Moss effect, which consists in increase of the bandgap due to high electron concentration at the surface. The phase jump approach under the constraints $\rho_\phi = 3.2$, $\rho_t = 0.5$ cannot fit the experimental data of Yang *et al.* over the whole range. Nevertheless, comparison with the data of Chen *et al.* suggests that upon different experimental conditions (electric field, carrier concentration), an adjustment of the reference energy E_a is required, see Fig. 4.21. For the four experimental points pertaining to larger diameter, $E_a = 3.25$eV gives a good fit.

These experiments show that cathodoluminescence experiments provide an interesting testbed for the phase jump approach, even outside of the confinement regime. It is suggested that high carrier concentrations may increase the spatial range of quantum coherence.

4.3. Discussion

4.3.1. Generalized sizing curve equation

We have tested the phase jump approach for a wide variety of II-VI and III-V semiconductor nanocrystals. A most general form of the energy-size dependence for excitonic transitions is emerging, if we extrapolate its applicability to nanorods of the same materials. It can be stated under the following form:

$$E(n, A) = E_a \frac{A.n + (1 + A)\rho_\phi}{A.n + (1 + A)\rho_t} + E_s \tag{4.13}$$

In this generalized form, the parameters are as follows:

- E is the energy of any excitonic transition in absorption and emission spectra.
- n is the size of the confining dimension in number of monolayers.
- E_a is the reference energy pertaining to the given transition.
- $\rho_\phi = \phi_s/\phi_a$ is the phase jump ratio where ϕ_s is the phase jump at the reflecting surface and ϕ_a is the phase progression of the charge carrier between two nearest identical atoms on its path.
- $\rho_t = \phi_s/\phi_a$ is the time delay ratio where t_s is the time delay required to accomplish the phase jump ϕ_s and t_a is the time delay required to progress by a phase ϕ_a between two nearest identical atoms on the charge carrier's path.
- A is the aspect ratio of the object (smallest dimension divided by largest dimension).
- E_s is an energy shift.

We remark that the aspect ratio $A = 1$ for quantum dots. The relevant size n for the quantum dots in this generalized phase jump equation 4.13 is the diameter, as it is for the nanorods. The relevant size n for the nanoplatelets is the thickness.

In Tab. 4.4, we reproduce as a synopsis the relevant parameters values for all nanocrystals whose room temperature transitions have been probed with the phase jump equation.

We distinguish different invariants, the most constant being that the time delay ratio can always been tuned to 0.5, except for the indium arsenide nanocrystals. We have

Material	Monolayer thickness (nm)	Objects	Transition	E_a (eV)	ρ_ϕ	ρ_t	E_s (eV)
CdS	0.2910	QDs (Ekimov 1984, van Dijken 1998)	First	2.15	3.20	0.50	0.00
			Second	2.15	4.70	0.50	0.00
			Third	2.15	6.20	0.50	0.00
		NPLs (Ithurria 2011)	First	2.02	3.20	0.50	0.00
CdSe	0.3040	QDs (this work)	Emission	1.41	4.00	0.50	0.00
			First	1.41	4.25	0.50	0.00
			Second	1.41	5.00	0.50	0.00
			Third	1.41	6.30	0.50	0.00
		QDs (Peng 1998)	First	1.52	3.20	0.50	0.00
		NPLs (Ithurria 2011)	First	1.52	3.20	0.50	0.00
		NPLs (lat. ext., Tessier 2013)	First	1.492	3.20	0.50	0.00
		NWires (Yu 2003)	Emission	1.67	3.20	0.50	0.00
		NRods (Li 2001)	Emission	1.67	3.20	0.50	0.00
CdTe	0.3240	QDs (Yu 2003)	First	1.39	3.20	0.50	0.00
		NPLs (Ithurria 2011)	First	1.39	3.20	0.50	0.00
ZnO	0.2300	NRods (Chen 2006)	CL Emission	3.28	3.20	0.50	0.00
		NWires (Yang 2007)	CL Emission	3.25	3.20	0.50	0.00
ZnSe	0.2835	QDs (Smith 1999)	First	1.52	3.20	0.50	1.05
			Second	1.52	3.20	0.50	1.52
HgTe	0.3230	QDs (Kovalenko 2006, Lhuillier 2012)	First	2.02	3.20	0.50	-2.02
PbSe	0.3060	QDs (Yu 2004, Ma 2011)	First	2.55	3.20	0.50	-2.55
GaN	0.2600	NRods (Zagonel 2011)	CL Emission	2.71	3.20	0.50	0.00
InP	0.2930	QDs (Micic 1996)	Emission	1.01	5.30	0.50	0.00
			First	1.01	6.40	0.50	0.00
			Second	1.01	8.70	0.50	0.00
			Third	1.01	11.00	0.50	0.00
InAs	0.3030	QDs (Peng 1998)	Emission	0.51	44.00	8.20	-0.62
			First	0.51	45.40	8.20	-0.62

Table 4.4.: Synopsis of the phase jump parameters and monolayer sizes for the nanocrystals whose energy-size dependence was studied with respect to monolayer size.

suggested a correspondence of this time delay ratio to the capping half monolayer on the path of the charge carrier. In cadmium chalcogenide nanocrystals, the dangling bonds of cadmium favor its attachment to the capping ligands.

The fact that under the constraint $\rho_t = 0.5$, the outcome for the phase jump ratio of the emission and first absorption transition is often 3.2 for the studied nanocrystals of the literature is intriguing. The best determination of this value resulted from the best fits for CdSe and CdTe nanoplatelets and we chose to continue our study with a precision of two digits. The closeness to π, and the fact that wave reflections at interfaces are known to undergo phase shifts of π rad, suggests that the phase jump ratio must contain a term π. A thorough investigation for all materials with this preciser value is worthwhile.

4.3.2. Form of the sizing curve equation

The proposed phase jump equation has a linear energy size dependence. The fact that such a linear equation is accurate for a wide array of nanocrystals is surprising, as we have seen that conventional approaches are generally based on polynomials or fractional exponents.

More generally, an efficient curve fitting procedure is to make use of a Padé approximant, *i.e.* a ratio of polynomials [180, 181], which provides very accurate fits for energy levels, already at the second degree. Here we propose a form where a Padé approximant surprisingly gives good fit at the first degree.

4.3.3. Comparison with conventional approaches

The proposed phase jump approach implies that the angular velocity ω_a of the charge carriers' phasor on its path is constant whatever the size of the nanocrystal in the strong confinement range. This angular velocity must match the quantum coherent environment which sets the pace for the allowed energy levels. The mass of the charge carriers doesn't play a role in the phase jump approach. It is nominally absent from the phase jump equations. In conventional terms, we could correlate this to the domain where the dispersion relation between the wave vector and energy is linear.

Conventional treatments for the determination of energy eigenvalues in semiconductor nanocrystals also include phase shifts at the surface. For example, the WKB method includes a specific treatment at the turning points, *i.e.* at the nanocrystal surface. Other treatments invoke the Maslov index in order to quantify quantified phase shifts at caustics surfaces [182]. For conventional approaches, the shift in energy upon confinement results from a global quantum confinement potential and the lowest energy solution is the one related to the standing wave with the least possible nodes, whatever the size of the nanocrystal.

In the phase jump approach, the nodes are defined by the allowed angular phasor velocities of the pertaining orbital. The wavelength of the charge carrier stays constant for a given transition whatever the size of the nanocrystal. The lowest energy solution between multiple allowed paths is the one with the smallest total phase progression on its path. This is another way of stating the least action principle.

This difference in determination of the energy eigenvalues results in a difference in the energy-size relation for excitonic transitions. The overall good fitting results of the phase jump approach in the strong confinement domain suggests that it could give a good description of the behaviour of the charge carriers in that domain.

4.3.4. Experimental perspectives

The present research work is only a first exploration of the phase jump approach applied to semiconductor nanocrystals. Several investigations are required to have a better insight of its applicability.

The phase jump approach suggests that the charge carriers in colloidal nanocrystals may have a behaviour which shows similarities with the electrons in graphene. In order to test this experimentally, two experiments are suggested. Angle resolved photoemission spectroscopy (ARPES) could detail the conduction and valence band dispersion [183]. At colloidal nanocrystal size, this becomes achievable for extended nanoplatelets. The other suggested experiment is the investigation of the zero Landau level splitting in high magnetic fields. If the energy bands have a linear dispersion, like in graphene, the degenerate energy level should scale with magnetic field as $\sqrt{B}$ [184, 185, 186].

It is also of interest to investigate the applicability of the phase jump approach to core-shell systems. For the study of these heterostructures, additional difficulties emerge. The preferred path (*i.e.* path of least action) of the electron becomes less obvious. For instance, for a CdSe/CdS core shell QD, we need to determine the angular phasor velocity in CdSe relative to the one in CdS. The lattice mismatch also complicates the study. In order to continue this study, we suggest to gather good quality experimental data about core-shell nanoplatelets whose hetero-composition is known to the precision of one monolayer.

A change in capping ligands or in the dielectric environment inside and outside the QD generally results in a shift of the transition peaks [187, 188]. On the one side, as this modifies the electronic environment at the surface, it is expected that it also influences the value of the phase shift or time delay at the surface. In the light of this expectation, it is quite surprising that the phase shift and time delay ratios of a wide array of differently capped nanocrystals were found to be identical ($\rho_\phi = 3.2$, $\rho_t = 0.5$.). Experimental data that quantify the phase shift for different ligand exchanges are required to investigate this effect in more detail.

Different crystalline structures also influence the energy values of the transition peak, for example the relative peak position for the first and second transition is different

for CdSe QDs, between wurtzite and zincblende structures [62, 189, 190, 125]. This effect can also investigated with the phase jump approach.

4.4. Conclusion

We have introduced a simple relation that describes the energy-size dependence of excitonic transitions for a wide variety of II-VI and III-V semiconductor nanocrystals. The terms of the equation are deduced as phase shift and time delay values of charge carriers travelling on least action paths in the nanocrystal. The phasor angular velocities in the volume and at the surface of the nanocrystal are constrained by phase matching with the coherent standing wave solutions. This yields sets of invariant parameter values that can be reused or readjusted with slight modification for different materials and different dimensional confinements.

We have only given a rough outline, which we tested through curve fitting on experiment results of different materials (II-VI and III-V nanocrystals, QDs, nanoplatelets, quantum disks, nanorods, nanowires, colloidal as well as epitaxially grown nanocrystals) and phenomena (photoluminescence, cathodoluminescence, quantum confinement, Burstein-Moss effect). It is of interest to continue a thorough exploration of its applicability.

5. General conclusion and perspectives

During the three years' duration of this research work, we have studied the excitonic transitions of semiconductor nanocrystals. The work has started with the colloidal synthesis of CdSe/CdS core-shell QDs, continued with their spectral and structural characterization, and concluded with the development of a model that attempts to describe the dependence of the excitonic transitions on the characteristic dimensions of the nanocrystal.

In the first part, we have explored the different steps of colloidal syntheses of core/"thick shell" CdSe/CdS QDs which were optimized for non-blinking behaviour earlier in the same group. We have determined the different excitonic transitions in the wavelength range from 350-700 nm for ensemble samples of spherical CdSe QDs and characterized their sizes with TEM and SAXS from 2 to 11 nm diameter. We have coated these CdSe "cores" with a higher bandgap CdS shell and we have obtained stable and robust QDs suited for correlated PL and TEM characterization.

In the second part, we have characterized the time-resolved dynamics of individual core/"thick shell" CdSe/CdS QDs using confocal microscopy correlated with TEM techniques. We have investigated the influence of the excitation energy on their photoluminescence decay behaviour. For the very same QDs of size 20-30 nm, we could localize and characterize them independently bridging the gap between confocal photoluminescence microscopy and TEM. We have participated in the demonstration that the cathodoluminescence emission transition of these QDs and the photoluminescence transition have same energies. As the cathodoluminescence characterization has a spatial resolution 1000 times better than confocal photoluminescence optics, this work opens new perspectives in characterizing the luminescence properties of closely packed QDs.

In the third part, we outlined an original theoretical approach which offers the possibility to formulate an accurate energy-size dependence of the excitonic transitions in the strong confinement range for a wide variety of II-VI and III-V semiconductors, transposable from quantum dots to nanoplatelets and nanorods and from photoluminescence to cathodoluminescence. This approach considers the different paths on which localized charge carriers may travel in the nanocrystallites. The localized charge carriers are represented by phasors or arrows, whose angular spinning velocity determines the energy. At singularities like surfaces, the phasor undergoes a

phase jump. Fitting of the energy-size equation yields invariant values for parameter values that suggests that the phase jump includes a dependence on π and that the time delay needed for that phase jump is related to the extra half monolayer of nanocrystals whose cations coat the surface. This gives good results for various dimensional confinements.

A. Appendices

A.1. Experimental data of CdSe QDs

A.1.1. QD sizes and transitions

23 CdSe QDs samples have been characterized.

The emission transitions have been determined through pointing at the maximum intensity of the peaks. For the determination of the absorption and PLE transitions, the diffusive and continuous background absorbance A_b has first been subtracted from the absorption spectra through a cubic power function $A_b = a(E - E_0)^3 + b$, with E the energy variable. The resultant energy spectra have then been fitted with the Gaussian multi peak curve fitting procedure of Origin 8 from OriginLab Corporation. The resultant peak positions have been determined by picking at maximum. Uncertainty in picking is 10 meV

The sizes have been determined with the help of TEM images, on a number of QDs varying from 50 to 100 QDs, through pointing the smallest and longest size of the QD and taking the average of both as the characteristic size of the QD. Uncertainty in picking is 0.2 nm, to which one has to add the uncertainty in surface determination through contrast in the TEM image.

Some QD sizes have been cross-checked with SAXS as described in sec. 1.7.7.

Transitions and QD sizes are given in Tab. A.1. Size distribution histograms are given in Tab. A.2 and Tab. A.3.

Reference	TEM radius	number	SAXS radius	Deep trap	Emission	Abs 1st	Abs 2nd	Abs 3rd	Abs 4th	Abs 5th	Abs 6th	Abs 7th	PLE 1st	PLE 2nd	PLE 3rd	PLE 4th	PLE 5th	PLE 6th
A702 130207_02	0.945	40		1.99	2.83	2.91	3.23	3.38										
A703 130207_03	1.010	100		1.93	2.69	2.76	3.01	3.42					2.77	3.05	3.59	3.94		
A704 130207_04	1.110	100		1.86	2.60	2.69	3.01	3.38					2.68	2.95	3.36	3.77		
AD01 110527_01	1.125	100		1.78	2.56	2.64	2.87	3.35										
A705 130207_05	1.170	100		1.77	2.55	2.63	2.86	3.32					2.63	2.88	3.34	3.84		
A706 130207_06	1.245	100			2.49	2.55	2.74	3.19	3.74				2.55	2.80	3.18	3.40		
AD02 110601_02	1.345	100		1.69	2.39	2.46	2.68	3.03										
A707 130207_07	1.370	100			2.42	2.48	2.65	3.09					2.48	2.72	3.09	3.36		
A709 130207_09	1.410	100			2.39	2.44	2.63	3.02	3.43				2.44	2.66	2.98	3.25		
A708 130207_08	1.450	100			2.40	2.45	2.64	3.04	3.46				2.45	2.67	3.00	3.29		
AD03 110623_03	1.840	100	1.87		2.15	2.19	2.35	2.64	3.16	3.43			2.19	2.34	2.63	2.97	3.32	
AD05 110606_02	1.970	100	2.05		2.11	2.14	2.27	2.55		3.45	3.65							
AD06 110524_03	2.045	100			2.09	2.11	2.24	2.51	2.95	3.42	3.62		2.11	2.23	2.50	2.94	3.36	
AD07 110524_04	2.400	50	2.32		2.01	2.03	2.14	2.39	2.81	3.35	3.61		2.03	2.13	2.51	2.96	3.30	
AD08 110616_04	2.945	50	3.07		1.93	1.95	2.03	2.21	2.37	2.75	3.28	3.60	1.95	2.03	2.26	2.66	3.24	
AD09 110524_05	2.950	50	2.83		1.92	1.95	2.03	2.19	2.39	2.72	3.21	3.53	1.95	2.03	2.23	2.67	3.26	
AD11 110527_07	3.020	50	3.30		1.90	1.92	1.99	2.18	2.35	2.61	3.15	3.47						
AD10 110617_04	3.090	50	3.34		1.91	1.92	2.01	2.17	2.35	2.62	3.20		1.93	2.02	2.17	2.35	2.58	3.16
AD12 110601_05	3.545	50	3.33		1.84	1.85	1.91	2.03	2.19	2.38	2.75							
AD13 110606_06	3.845	50	4.29		1.82	1.84												
A101217	4.345	100			1.79	1.83	1.87											
AD14 110623_06	4.580	100	4.87		1.78	1.81												
AD15 110705_04	5.715	50	5.66		1.76	1.78												

Table A.1.: Radius (in nm) and transition energies (in eV) of the CdSe QDs

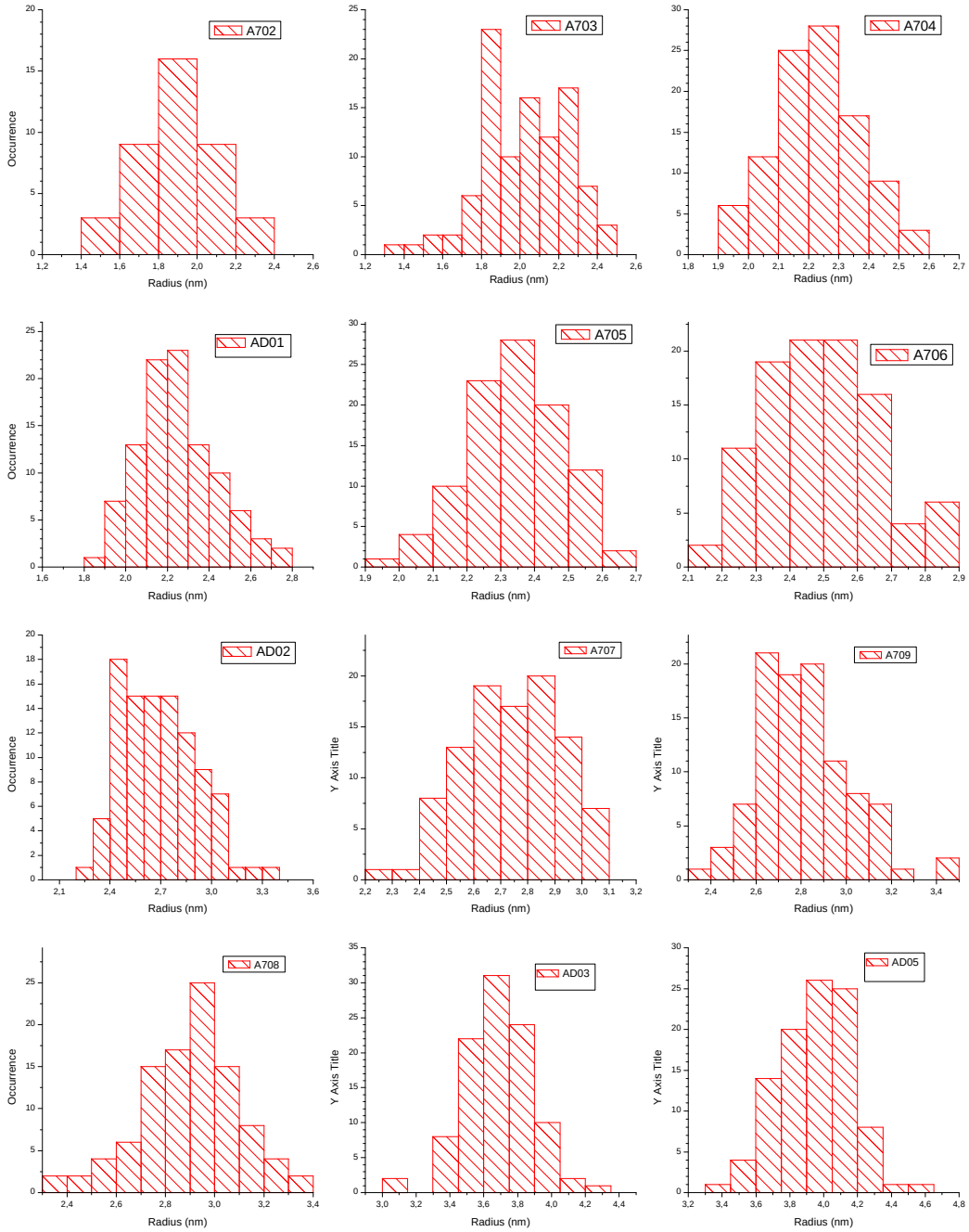

Table A.2.: Dispersion in sizes determined by TEM for CdSe QDs for samples A702 to AD05

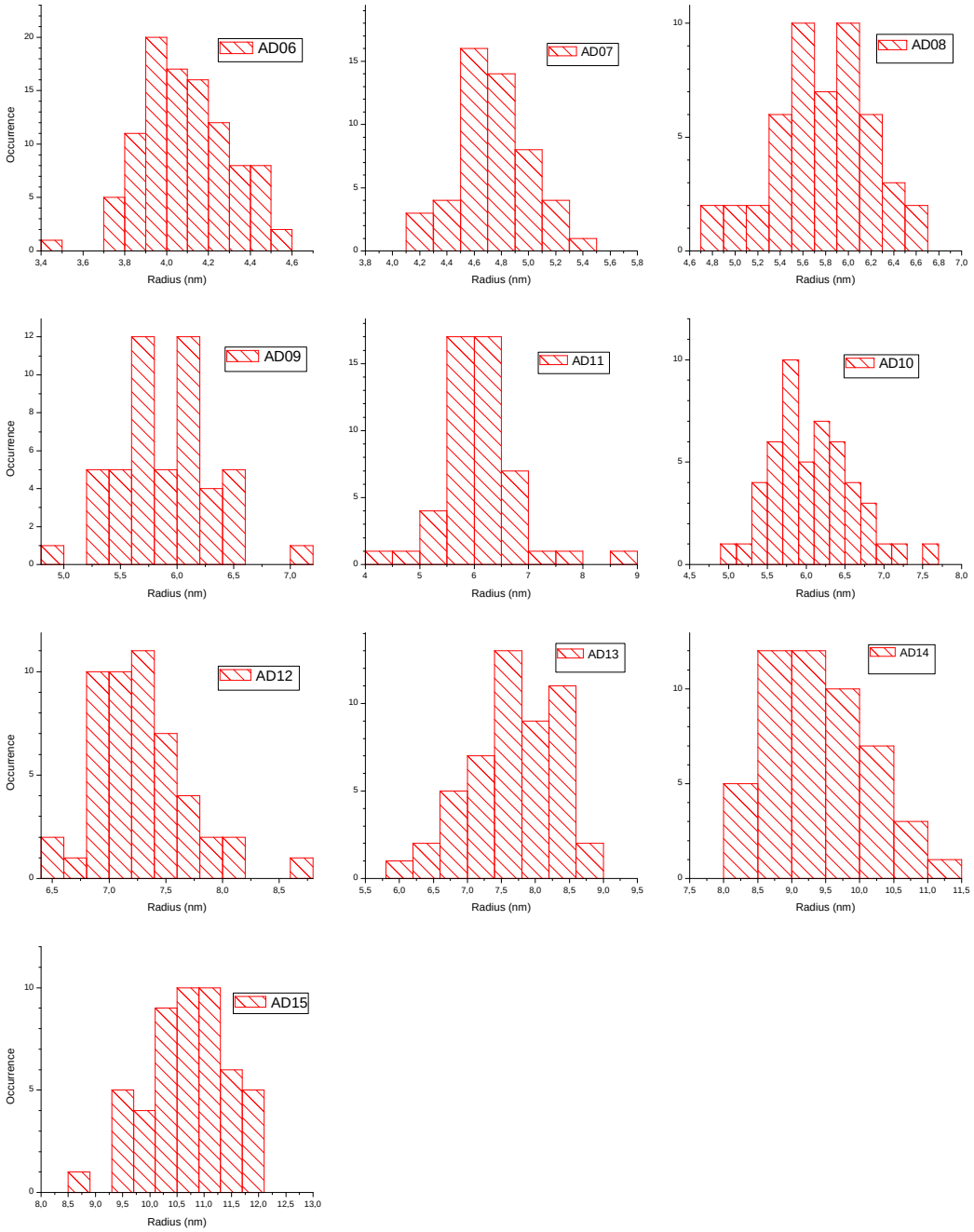

Table A.3.: Dispersion in sizes determined by TEM for CdSe QDs for samples AD06 to AD15

A.1.2. Secondary peak

In sec. 2.3.3.3, we reported the existence of a secondary emission peaks in the emission spectra of CdSe QDs. The evolution of its energy with respect to the wavelength of the primary peak was investigated in sec. 4.2.3.3. Tab. A.4 gives the measured wavelength of both primary and secondary peak for the emission spectra of aliquots taken during the syntheses. The wavelength was determined by pointing at the maximum of intensity..

Sample reference	QD Emission peak (nm)	Secondary emission peak (nm)
110114_05	554	618
110114_06	562	633
110114_07	560	632
110114_08	566	638
110114_09	567	640
110114_10	567	639
110114_11	568	642
110114_12	573	644
110114_13	575	646
110505_02	589	669
110505_03	596	679
110511_04	577	661
110511_03	574	654
110630_01	566	641
110420_01	541	604
110420_02	561	635
110420_03	563	639

Table A.4.: CdSe QD and secondary emission peak values

A.2. Transition energies of literature

For the practical determination of the parameter values of the phase jump equation, it is required to handle spectral experimental data and the respective sizes of nanocrystals. In some cases, the data are given ready to be handled in the literature. In other cases, the data are not ready for use. The solution is then either to request directly the original data from the corresponding author, if one need precise data, or to infer them from the graphs by pointing and reading the values on the axes, if a rapid less precise verification is sufficient. For a number of our verifications of the phase jump equation, we have used experimental data read from graphs of the literature. In order to facilitate the reuse and possible corrections by the original data, we report in Tab. A.5 and Tab. A.6 the experimental data read from graphs, which we emphasize may differ slightly from the original data. Radius is given in nm. Energies are given in eV.

CdS (Ekimov 1984)			
radius	1st	2nd	3rd
2.72166	2.79	3.02	3.3
2.18218	2.89	3.26	3.62
1.9245	3	3.44	3.84
1.78174	3.07	3.52	4.03
1.65748	3.14	3.68	4.18
1.57135	3.17	3.74	4.33
1.40028	3.23	3.9	4.57
1.34231	3.27	3.98	4.62

ZnSe (Smith 1999)		
radius	1st	2nd
1.31	3.36	
1.745	3.17	3.7
2.355	3.01	3.49
2.8	2.96	3.42
3.245	2.93	3.38
3.6	2.88	3.34

HgTe (Kovalenko 2006)	
radius	PL
1.8	0.993
2.1	0.8275
2.35	0.66024
2.9	0.5642
3.15	0.4965
4.5	0.41375
5.9	0.35464

HgTe (Lhuillier 2012)	
radius	1st
2.2	0.59107
2.85	0.65329
3.5	0.43553
3.65	0.43553
3.9	0.4965
5	0.31031
6.05	0.24825

PbSe (Yu 2004)	
radius	1st
1.625	1.1419
1.85	1.05191
2.1	0.96973
2.215	0.88157
2.225	0.859
2.505	0.79926
2.75	0.73796
2.8	0.69344
3.075	0.65675
3.325	0.62031
3.375	0.59964
3.475	0.59305
3.525	0.57706
3.65	0.56678
3.76	0.56038
4.01	0.5456
4.375	0.53897

PbSe (Ma 2011)	
radius	1st
0.555	2.26
0.77	2.04
0.94	1.95
0.965	1.82
1.085	1.7
1.145	1.58
1.315	1.46
1.43	1.37

Table A.5.: Data read from graphs of the literature (first part) [163, 165, 166, 167, 191, 169]. Radius is given in nm, energy in eV.

InP (Micic 1996)				
radius	PL	1st	2nd	3rd
1		2.53		
1.3	2.09	2.38		
1.45	2.02	2.27		
1.5	1.96	2.19	2.54	
1.65	1.92	2.12		
1.75	1.81	2.01	2.42	
1.9	1.8	1.96		
2		1.87		
2.1	1.76	1.9	2.23	2.52
2.2		1.89		
2.25	1.67	1.81		
2.4		1.8	2.08	2.33
2.5	1.68	1.77		
2.7	1.58	1.7		
3	1.6	1.7	1.92	2.14

ZnO (Chen 2006)	
radius	CL
25	3.36
32.5	3.34
50	3.32
60	3.315
90	3.305

ZnO (Yang 2007)	
radius	CL
25	3.343
50	3.307
100	3.272
125	3.263
225	3.262
365	3.255

GaN (Zagonel 2011)	
radius	CL
4	4.17
4	4.15
4	4
4	3.8
5	4.05
5	3.95
5	3.85
6	3.9
6	3.76
6	3.72
7	3.67
7	3.65
7	3.59
8	3.7
8	3.62
9	3.59
9	3.54
9	3.46
9.5	3.65
10	3.5
10	3.35
10.5	3.44
10.5	3.43
10.5	3.37
10.5	3.35
11	3.41
11	3.37
12	3.32

Table A.6.: Data read from graphs of the literature (second part) [170, 136, 178, 179]. Radius is given in nm, energy in eV.

A.3. Quantum particle modelized as a rotating vector

All we do is draw little arrows on a piece of paper — that's all!

Richard P. Feynman

Any elementary quantum object (neutrino, photon, electron, muon, tauon, quark...) is described by a state vector in a complex vector space. Collections of these particles are also described by a state vector. In order to facilitate the visual representation of the state vector, Richard Feynman presented a diagrammatic method of following its multiple possible evolution histories on a piece of paper, so called Feynman diagrams [192]. He later presented the state vector as an arrow which physicists draw on a piece of paper [147]. In the present research work, we take advantage of this practical set of tools and transpose the state vector arrows to 3D space arrows (equivalently rods or needles).

This visual and mechanical analogy, although it has to be handled with care in order to avoid false deductions, facilitates the presentation of some fundamental quantum principles and postulates. As an example, Fig. A.1 presents the derivation of a Schrödinger-like equation for a spinning arrow in 3D-space. We detail the steps as they appear in the figure.

Step 1. Vector difference between two successive states of the spinning arrow

Let the unit vector $|\psi(t = t_0)\rangle$ represent a spinning arrow of unit length in 3D space at time t_0 and spinning at angular velocity ω. At timestamp $t_0 + \mathrm{d}t$, the orientation of the arrow has changed by an infinitesimal angle $\mathrm{d}\phi = \omega \mathrm{d}t$. The vector difference $\mathrm{d}\,|\psi(t)\rangle = |\psi(t + \mathrm{d}t)\rangle - |\psi(t)\rangle$ is a vector of infinitesimal length whose orientation in 3D space is always perpendicular to $|\psi(t)\rangle$.

Step 2. Multiplication of the vector by a complex exponential $e^{i\frac{\pi}{2}}\omega \mathrm{d}t$

We now detail another operation that allows to retrieve $\mathrm{d}\,|\psi(t)\rangle$. We first multiply the vector $|\psi(t)\rangle$ by the imaginary unit $i = e^{i\frac{\pi}{2}}$. This gives a vector $i\,|\psi(t)\rangle$ that is perpendicular to $|\psi(t)\rangle$, we then multiply its length by $\omega \mathrm{d}t$, giving the vector $i\,|\psi(t)\rangle\,\omega \mathrm{d}t$ of infinitesimal length.

Step 3. Schrödinger-like equation

The infinitesimal vectors $i\,|\psi(t)\rangle\,\omega \mathrm{d}t$ and $\mathrm{d}\,|\psi(t)\rangle$ are equal. Writing their equality results in the Schrödinger-like equation:

$$-i\frac{\mathrm{d}\,|\psi(t)\rangle}{\mathrm{d}t} = \omega\,|\psi(t)\rangle \tag{A.1}$$

If we transpose this analogy to elementary particles like photons, electrons or quarks, the angular velocity ω determines the energy of the particle in units $\hbar$. The operator $-i\frac{\mathrm{d}}{\mathrm{d}t}$ is called the Hamiltonian of the quantum system. It describes how the state vector evolves.

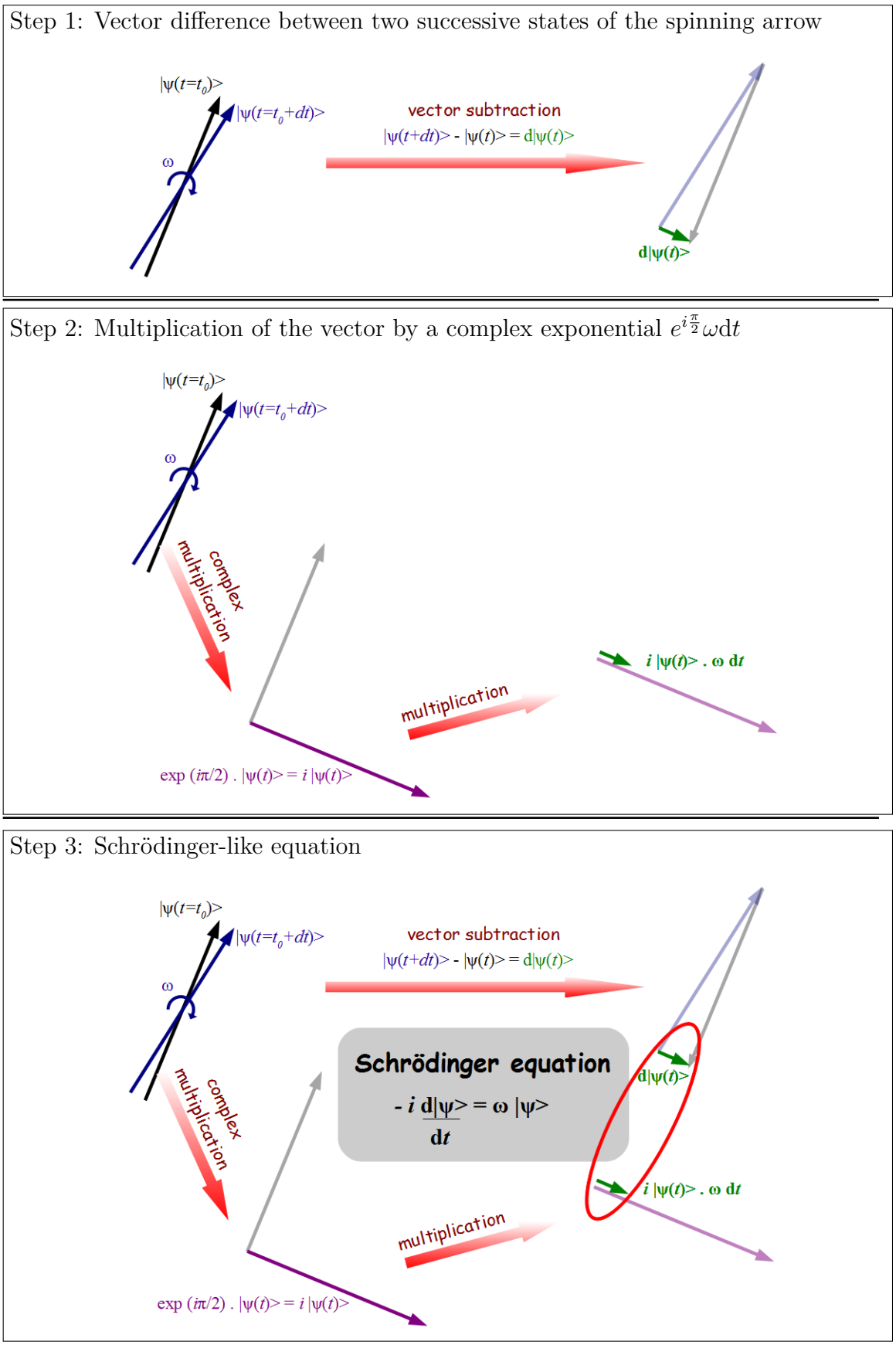

Figure A.1.: Schrödinger equation presented as the equation describing the evolution of spinning arrows. Steps of the derivation are presented in the text.

B. Résumé substantiel de thèse

B.1. Introduction

Les boîtes quantiques colloïdales, aussi appelées “quantum dots”, sont des nanocristaux semiconducteurs cristallins dont la taille est de quelques nanomètres. Des ligands de surface assurent la stabilité en solution colloïdale. En tant que semiconducteurs, les quantum dots absorbent et émettent de la lumière dont l'énergie dépend de l'écart entre les différents niveaux d'énergie. La particularité des quantum dots est que cet écart peut être ajusté en fonction de la taille et/ou de la forme du nanocristal.

On peut mentionner de nombreuses applications des quantum dots. Comme absorbeurs de photons, ils sont utilisés dans le photovoltaïque. Comme émetteurs, ils sont utilisés dans l'imagerie biomédicale ou dans les composants électroniques et opto-électroniques tels qu'écrans plats, nanolasers ou diodes électroluminescentes.

Le changement de couleur de fluorescence en fonction de la taille peut être suivi lors d'une synthèse colloïdale en prélevant de petites quantités de la solution à différents moments de la synthèse et en mesurant leurs spectres d'absorption et d'émission. Pour le matériau prototype de séléniure de cadmium (CdSe), lorsque le nanocristal quasi-sphérique grandit de 2 à 6 nm, la fluorescence vire du bleu au rouge, en passant par le vert, le jaune et l'orange. Le spectre d'absorption se compose d'un premier pic décalé de quelques dizaines de meV par rapport au pic d'émission, le décalage de Stokes. Deux autres pics d'absorption se distinguent clairement à plus haute énergie. Tous ces pics se décalent vers des énergies plus basses à mesure que le nanocristal grandit. L'étude de la dépendance entre l'énergie et la taille du quantum dot est un des sujets de cette thèse.

Pour étudier cette dépendance énergie/taille, il faut disposer d'échantillons dont la dispersité en taille est faible. La synthèse de quantum dots CdSe monodisperses est maîtrisée depuis les synthèses de Chris Murray en 1993 [61]. Au niveau individuel, ces quantum dots ne sont pas très brillants. De plus, ils ont la fâcheuse propriété de photoblanchir rapidement. L'efficacité quantique est nettement améliorée lorsqu'on les revêt d'une coque de matériau dont la largeur de bande interdite est plus grande que celle du coeur. Ainsi, en 1996, Margaret Hines et Philippe Guyot-Sionnest ont annoncé qu'en revêtant les coeurs CdSe d'une coque fine de ZnS, ils obtenaient des quantum dots de résistance bien meilleure au photoblanchiment et d'efficacité quantique de 50% à température ambiante [64]. La suppression quasi-totale du

clignotement a fait l'objet de nombreux efforts de la part des chimistes du domaine. En 2008, en rajoutant une coque épaisse de CdS, Benoît Mahler obtint des quantum dots dont le clignotement est quasiment nul [9]. La synthèse de ce type de quantum dots est décrite dans le chapitre 2 de la thèse.

Ces quantum dots coeur-coque CdSe/CdS sont d'excellents émetteurs de photons uniques. Les détails du mécanisme d'excitation/recombinaison des paires électron/trou - aussi appelés excitons - dans ces quantum dots font encore l'objet de nombreuses études. La recombinaison Auger, où l'électron (ou le trou) excité perd son énergie par collision avec d'autres électrons ou trous, joue un rôle important dans la réduction du rendement quantique et du temps de vie de fluorescence. Afin d'étudier ces effets et leur relation à la structure, la taille ou la forme du quantum dot, nous avons mis en oeuvre une technique d'imagerie corrélative de microscopie optique de fluorescence combinée à la microscopie électronique à transmission. Ces travaux d'imagerie corrélative optique/microscopie électronique ont pu être complétés par des mesures de cathodoluminescence sur quantum dots uniques, grâce à une collaboration avec Zackaria Mahfoud de l'équipe de Mathieu Kociak du Laboratoire de Physique des Solides à Orsay. Ces expériences d'imagerie corrélative sont exposées dans le chapitre 3 de la thèse.

Enfin, nous nous intéressons à la dépendance de l'énergie en fonction des dimensions du nanocristal, pour des nanocristaux de formes différentes, tout particulièrement pour les nanoplaquettes colloïdales de structure zincblende CdS, CdSe et CdTe découvertes par Sandrine Ithurria en 2008 [123]. Ces nanoplaquettes peuvent être synthétisées avec une épaisseur définie à la monocouche près. A partir de leurs énergies de transition, il est difficile de prédire exactement l'épaisseur de ces nanoplaquettes au moyen des théories en cours, telles que l'approche de masse effective ou la combinaison linéaire d'orbitales atomiques. Nous proposons une équation simple qui relie l'énergie d'une transition électronique à la taille du nanocristal. Cette équation est valable en confinement fort 1D, 2D et 3D pour différents matériaux. Elle est présentée dans le chapitre 4 de la thèse.

Cette thèse s'articule donc autour de trois axes de recherche :

- Synthèse colloïdale de quantum dots CdSe de tailles différentes et amélioration de leurs propriétés de fluorescence par la croissance d'une coque CdS (chapitre 2).

- Caractérisation individuelle de ces quantum dots par imagerie corrélative de microscopie de fluorescence confocale et microscopie électronique à transmission (chapitre 3).

- Modélisation des transitions électroniques des quantum dots CdSe avec vérification du modèle sur des nanocristaux de forme et de composition différentes (chapitre 4).

B.2. Synthèse de quantum dots CdSe/CdS à coque épaisse

Pour synthétiser les quantum dots sphériques CdSe en structure zincblende, nous utilisons un protocole de nucléation/croissance dérivé de celui de Yang *et al.* du groupe de Cao [110]. La nucléation/croissance de nanocristaux a été modélisée par LaMer et Dinegar [111]. Il s'agit de déclencher en un temps très court la nucléation de cristaux. En raison de la consommation rapide de précurseurs, leur concentration ne restera que très peu de temps au-dessus du seuil de nucléation. Pendant le temps restant de synthèse, les noyaux vont croître de façon plus ou moins homogène en fonction de l'apport supplémentaire de précurseurs.

Avec ce protocole, où du sélénium élementaire et du myristate de cadmium sont dissous dans de l'octadécène puis chauffés à 240°C dans de l'octadécène, nous avons synthétisé des nanocristaux CdSe sphériques dont le diamètre varie de 2 à 12 nm. Ces échantillons ont servi pour la caractérisation des transitions électroniques d'absorption et d'émission en fonction de la taille. La taille des nanocristaux a été déterminée par microscopie électronique à transmission (TEM), ainsi que par diffusion de rayons aux petits angles (SAXS). Toutes les transitions se décalent vers les basses énergies lorsque les nanocristaux croissent. En fonction de la concentration des précurseurs et de l'apport de ligands (acide oléique, oléylamine), des pics secondaires peuvent apparaître. Ces pics indiquent la présence d'objets autres que les quantum dots (aggrégats, nanobâtonnets, nanoplaquettes).

Dans un deuxième temps, nous avons utilisé un protocole d'injection par goutte à goutte développé dans le groupe pour faire croître une coque épaisse CdS sur les coeurs zincblende de CdSe sphériques. La solution injectée est un mélange stoechiométrique d'oléate de cadmium et de soufre dissous dans de l'octadécène. Nous avons varié la température de la solution de 280°C à 310°C et les vitesses d'injection goutte à goutte mais la difficulté à reproduire la synthèse en conditions identiques ne nous a pas permis d'établir un protocole optimal. Lors de la croissance de la coque, le pic d'émission du CdSe subit un décalage supplémentaire, alors que les pics d'absorption CdSe disparaissent en faveur d'une large bande d'absorption spécifique au CdS, dont le seuil est situé vers 2,3 eV.

Sur les images de TEM, ces quantum dots à coque épaisse ont une forme de losange, avec petit axe environ 20 nm et grand axe environ 30 nm, voir Figure 2.11a. On distingue pour chacun des quantum dots individuels des contrastes différents pour des plans perpendiculaires au grand axe. En imagerie à haute définition, ces contrastes résultent de polytypismes wurtzite/zincblende de la coque.

Malgré ou à cause de ce polytypisme, ces quantum dots ont une luminescence très stable sans clignotement apparent lorsqu'on les enregistre en film à 30 images par seconde. Au bout de 10s, moins de 5% de ces quantum dots ont clignoté.

Ces échantillons de nanocristaux coeur-coque CdSe/CdS ont servi ultérieurement

pour une caractérisation en microscopie confocale de fluorescence et en cathodoluminescence sur quantum dots uniques.

Au cours des différentes synthèses, nous avons également abordé la synthèse de nanoplaquettes, nanocristaux bi-dimensionnels dont l'épaisseur est définie à la monocouche atomique près et dont la largeur à mi-hauteur de la transition électronique émissive dans le spectre visible est d'environ 10 nm au lieu de 25 nm pour les quantum dots sphériques [123]. Ses transitions sont modélisées dans le chapitre correspondant.

B.3. Imagerie corrélative en microscopie de fluorescence et en microscopie électronique

Les expériences de microscopie à fluorescence sur nanocristaux uniques ont permis d'enregistrer des traces résolues en temps de l'émission des quantum dots coeur-coque en unique, d'enregistrer leur spectre, leur profil d'antibunching, leur courbe de décroissance de temps de vie. Ces mesures ont été effectuées sur un montage confocal MicroTime 200 (Picoquant) à deux détecteurs à photons uniques et à laser diode pulsé 402 nm. Ce montage est complété d'un spectromètre et d'un laser à spectre continu dont la longueur d'onde peut être accordée entre 430 et 650 nm.

Un des objectifs de la thèse était de pouvoir disperser des nanocristaux sur un substrat et de les caractériser en unique en microscopie confocale optique puis de déterminer la taille et structure de ces mêmes objets uniques en microscopie électronique. Les nanocristaux coeur-coque CdSe/CdS, de par leur taille et comportement non-clignotant se prêtent bien à cet exercice. Nous avons utilisé le microscope électronique à transmission à effet de champ JEOL 2010 de l'ESPCI. La cathodoluminescence a pu être observée sur les mêmes objets uniques sur un microscope électronique à transmission et à balayage (STEM) du Laboratoire de Physique des Solides à Orsay. Plusieurs contraintes sont limitantes pour ce type de mesure : le substrat, la dispersion des nanocristaux sans agrégation, leur cartographie et le transport entre les microscopes optique et électronique. Afin de retrouver les mêmes quantum dots sur les trois dispositifs expérimentaux, nous avons utilisé des grilles TEM en nitrure de silicium (Si_3N_4) avec marqueurs en or disposés tous les 5 µm.

Les quantum dots coeur-coque CdSe/CdS synthétisés ont une fluorescence remarquablement stable lorsqu'ils sont excités à puissance monoexctonique. Les temps de vie sur lamelle de verre sont de l'ordre de 25 ns, correspondant à l'état gris chargé des caractérisations faites sur des objets similaires [11]. Sur les grilles en nitrure de silicium, ces temps de vie sont de l'ordre de 10 à 15 nm.

Ces observations en imagerie corrélative microscopie optique et électronique nous ont permis de comparer les caractéristiques de photoluminescence avec la forme et taille des nanocristaux. Il n'a pas été possible d'établir de corrélation évidente,

d'une part parce que la résolution en TEM sur les grilles de nitrure de silicium n'était pas suffisante pour visualiser les plans atomiques en haute résolution. D'autre part, si corrélation il y a, celle-ci résulte probablement de défauts qui se situent à l'interface du coeur et de la coque des nano-objets observés, et donc inobservables en microscopie électronique à transmission conventionnelle.

Au bilan positif, il a pu être vérifié, et c'est une première, que le pic de cathodoluminescence d'un quantum dot coeur-coque CdSe/CdS a la même énergie que celui de photoluminescence.

Nous avons également observé des nanoplaquettes coeur-coque CdSe/CdS en imagerie corrélative de microscopie optique et électronique. Ceci a permis de vérifier sur objets uniques que la transition émissive se décale vers les basses énergies pour des nanoplaquettes dont l'extension latérale est plus grande.

B.4. Modélisation des transitions électroniques

Les transitions électroniques de semi-conducteurs proviennent soit de la création d'un exciton par absorption d'énergie, soit de la recombinaison de l'électron et du trou excitoniques par restitution d'énergie. Les transitions optiques (absorption et émission de photons) sont les plus commodes à étudier. Les niveaux d'énergie découlent de la structure en bandes d'énergie autorisées et interdites des matériaux cristallins. Plusieurs approches prévalent pour leur modélisation.

L'approximation de masse effective détermine les niveaux d'énergie autorisés en partant de la structure bulk du matériau, puis adapte ces niveaux en fonction de la taille et la forme de l'objet. A cause de la diminution de la densité d'états électroniques en limite de bande, seuls vont subsister des niveaux quantifiés qui vont se décaler vers des énergies plus élevées au fur et à mesure que la taille diminue. En approximation parabolique, ce décalage en énergie suit une loi de type $E \sim 1/a^2$, où a représente la taille du nanocristal. Différentes corrections complètent l'équation qui relie l'énergie des transitions à la taille du nanocristal, notamment en tenant compte de l'interaction coulombienne entre électron et trou, ainsi que d'autres effets liés à la polarisation, la corrélation spatiale et l'interaction d'échange. En confinement fort, c'est-à-dire lorsque le rayon du nanocristal est inférieur au rayon de Bohr de l'exciton, l'expérience ne confirme pas les prédictions de l'approximation de masse effective [62, 63]. Ce problème a été qualifié de "problème balayé sous le tapis" [156].

Les approches de combinaison linéaire d'orbitales atomiques (LCAO ou tight-binding) et de pseudo-potentiels empiriques établissent des hamiltoniens dont les valeurs propres se rapprochent des valeurs de l'expérience. La relation qui relie l'énergie aux dimensions du nanocristal n'est dans ce cas généralement pas établie de façon analytique et l'on préfère utiliser des formules d'ajustement empiriques polynomiales, pour les besoins pratiques de détermination de concentrations d'une solution en

nanocristaux. Pour la première transition excitonique du séléniure de cadmium, on trouve ainsi plusieurs formules d'ajustement, des polynômes empiriques de quatrième degré où la taille est exprimée en fonction de la longueur d'onde [114, 115], des équations où l'énergie de confinement en fonction de la taille est donnée par un polynôme du second degré en numérateur [116, 117], ainsi qu'une formule où l'exposant appliqué à la taille du quantum dot est non-entière [118].

Dans cette thèse, nous proposons une équation alternative pour la relation énergie-taille. Cette équation s'écrit:

$$E(a) = E_0 \frac{a + \gamma_\phi}{a + \gamma_t} \tag{B.1}$$

où E_0 est une énergie de référence, a représente le rayon des quantum dots et où γ_ϕ et γ_t sont des facteurs métriques de phase et de délai temporel. Les données expérimentales de quantum dots CdSe et InAs de haute qualité de Norris et de Banin [62, 63] peuvent être ajustées avec cette formule avec un coefficient de détermination supérieur à 0,99, pour toutes les transitions étudiées. Cette équation, que nous nommerons l'équation de saut de phase, a la forme d'un approximant de Padé de premier ordre.

Pour l'étude de l'interprétation physique de cette équation de phase, il est utile d'exprimer le rayon en nombre de monocouches. Nous l'écrirons alors sous la forme:

$$E(n) = E_a \frac{n + \rho_\phi}{n + \rho_t}. \tag{B.2}$$

Cette équation peut être déduite par une approche quantique d'intégrale de chemin, où l'électron (ou le trou) est représenté par un vecteur tournant (phaseur) sur sa trajectoire. En circulant dans le réseau cristallin du semiconducteur, lorsque la phase progresse d'un angle ϕ_a d'atome en atome en un temps t_a, l'énergie de l'électron peut être exprimée par sa vitesse angulaire que multiplie $\hbar$, ainsi: $E = \hbar\phi_a/t_a$. Si nous considérons un nanocristal semiconducteur, un accord de phase va s'établir entre le vecteur tournant représentant l'électron circulant d'atome en atome et les ondes stationnaires occupant tout le nanocristal, de façon similaire à la particule guidée par son onde pilote [161, 160]. En cas de réflexion à la surface, la phase du vecteur tournant doit effectuer un saut de phase pour rester en concordance de phase avec l'onde stationnaire. Si le saut de phase et le temps nécessaire sont notés ϕ_s et t_s, avec $\rho_\phi = \phi_s/\phi_a$ et $\rho_t = t_s/t_a$, nous pouvons déduire l'équation B.2 pour un électron qui rebondit à la surface après avoir progressé en ligne droite de n atomes.

En prenant des données de la littérature, l'équation peut être transposée des quantum dots CdSe de rayon n monocouches aux nanoplaquettes CdSe d'épaisseur n monocouches, tout en gardant les mêmes paramètres $E_a = 1,52\text{eV}$, $\rho_\phi = 3,2$ et

$\rho_t = 0,5$, voir Fig. 4.8. Il faut noter que la valeur ajustée pour l'épaisseur des nanoplaquettes est dans ce cas confirmée par les observations en microscopie électronique, contrairement aux prédictions de l'approximation de masse effective ou du tight binding. Pour le tellure de cadmium, il suffit de remplacer l'énergie de référence par $E_a = 1,39\text{eV}$ pour donner une formule d'ajustement aux données expérimentales des quantum dots et des nanoplaquettes. Pour l'ajustement aux données des nanoplaquettes de sulfure de cadmium, l'énergie de référence est donnée par $E_a = 2,02\text{eV}$.

L'équivalence de la première transition d'absorption pour les quantum dots et nanoplaquettes de même matériau suggère un chemin électronique représenté par Fig. 4.6 et Fig. 4.7. Dans ce cas, le nombre de réflexions par unité de chemin est identique dans les deux cas.

En adaptant l'équation B.2 pour des nanobâtonnets, des nanofils ou des nanoplaquettes à extension latérale limitée, on obtient une équation plus générale:

$$E(n, A) = E_a \frac{A.n + (1 + A)\rho_\phi}{A.n + (1 + A)\rho_t} + E_s \tag{B.3}$$

où:

- E est l'énergie d'une quelconque transition excitonique des spectres d'absorption et d'émission
- n est la taille de la dimension confinante en nombre de monocouches.
- E_a est l'énergie de référence de la transition.
- $\rho_\phi = \phi_s/\phi_a$ est le facteur de saut de phase où ϕ_s est le saut de phase à la surface et ϕ_a est la progression de phase de l'électron ou du trou sur leur chemin entre deux atomes identiques.
- $\rho_t = \phi_s/\phi_a$ est le facteur de délai de phase où t_s est le délai de phase nécessaire pour accomplir un saut de phase ϕ_s et t_a est le délai de phase nécessaire pour progresser d'une phase ϕ_a entre deux atomes identiques.
- A est le ratio d'aspect de l'objet (dimension la plus petite divisée par la dimension la plus grande).
- E_s est un décalage en énergie.

L'ajustement aux données expérimentales fait ressortir des valeurs remarquables et récurrentes pour les paramètres de saut de phase (par exemple 3,2 qui est proche de π). Un aperçu des différentes valeurs de paramètres pour cette équation est donné dans Tab. 4.4.

B.5. Conclusion

Lors de notre travail de recherche doctoral, nous avons déterminé une courbe expérimentale énergie-taille pour les nanocristaux sphériques CdSe sur une plage de tailles couvrant tout le régime de confinement excitonique. Nous avons également obtenu des quantum dots coeur/coque CdSe/CdS non clignotants dans le but d'utiliser les nanocristaux synthétisés dans les mesures croisées de photo- et cathodoluminescence. La colocalisation en microscopie optique et électronique a permis de vérifier que l'énergie du pic d'émission des coeurs-coques CdSe/CdS ne varie pas en fonction du moyen d'excitation employé : faisceau laser ou faiseau électronique.

Nous avons également établi une équation décrivant précisément la relation entre l'energie des transitions et les dimensions du nanocristal, en utilisant une approche quantique de type vecteur tournant avec sauts de phase lors des réflexions à la surface. Cette équation permet de simplifier la caractérisation en taille des nanocristaux semi-conducteurs à partir de leurs transitions électroniques, quelle que soit leur forme.

C. Acknowledgments

I acknowledge the Agence Nationale de la Recherche, who has funded this study about the behaviour of colloidal quantum dots.

Now that I have put a final point to this thesis, I would like to thank the important people who supported me either during this thesis, or even well before during the run-up towards this intense period of three years. These thankwords are personal. I therefore prefer to address them in colloquial language.

Avant tout, je tiens à te remercier, Benoit, d'avoir dirigé cette thèse. J'ai été conquis dès le départ par ton enthousiasme communicatif à propos des quantum dots et nanocristaux affiliés. Merci d'avoir été là pratiquement tous les mardis matin pour faire le point, pour me remettre sur les rails lorsque les synthèses ne produisaient pas les coeurs-coques escomptés, lorsque leur dispersion sur les grilles de TEM laissait à désirer. J'ai également apprécié ton ouverture à mes idées incomplètement formulées. Sans ton écoute et ta capacité à reformuler, je n'aurais jamais pu intégrer le modèle des vecteurs tournants dans cette thèse. Merci spécialement pour le coaching des derniers jours en vue de la soutenance.

Je tiens à remercier les membres de mon jury de thèse. Vos rapports, remarques et questions ont été très pertinents. J'en ai tenu compte en incluant quelques corrections dans la version finale de cette thèse. Nikolay Gippius, спасибо, d'avoir accepté d'être rapporteur, en plein déménagement professionnel France-Moscou. J'imagine que cela n'a pas dû être facile de lire une thèse et écrire un rapport alors que toute l'attention doit être focalisée sur le nouvel environnement de vie et de travail. Christophe Delerue, merci également d'avoir accepté cette charge supplémentaire d'examinateur et de rapporteur dans une période de début d'année universitaire déjà très chargée, de plus avec un manuscrit qui est arrivé très tard. Merci de m'avoir reçu en visite à Lille pour échanger sur le modèle et sur les différentes façons de formuler la dépendance énergie-taille des quantum dots. Mathieu Kociak et Alberto Bramati, merci pour votre intérêt pour les sujets abordés dans mon travail, pour les questions et commentaires pertinents. Mathieu, merci de m'avoir permis de collaborer sur les expériences de cathodoluminescence.

Many thanks, David Norris and Uri Banin, for sending me the original spectral data of your experiments. I would like to express my respect for your work on the CdSe and InAs quantum dots, which are of excellent quality for theoretical modeling. I was impressed by the fact that you could retrieve them so easily more than 15 years after the experiments have taken place.

Je tiens à remercier Cristiano Ciuti d'être venu discuter de mon modèle et de l'avoir mis en perspective avec les théories conventionnelles de masse effective et de tight-binding.

J'aimerais remercier tous ceux qui font tourner le Laboratoire de Physique et d'Etude des Matériaux, Jérôme, Sophie, Marie-Claude, Josiane, Francis et d'autres que je croisais de temps en temps dans les couloirs. Merci également à mon directeur d'école doctorale Jean Hare, à Nadine Yassine. C'est un travail important que de créer et maintenir les bonnes conditions de travail pour un travail de thèse. Merci!

Mickaël, merci pour ton aide sur les manips avec le MicroTime, le laser supercontinuum, les synthèses, les discussions sur les flèches tournantes, nos discussions à table aussi sur des sujets beaucoup plus généraux. Tout cela m'a été très précieux. Je te souhaite bonne continuation à Gand dans ce domaine passionnant et peu exploré des nanocristaux semiconducteurs. Je pense que tu iras loin.

Xiangzhen, grâce à toi, j'ai vu, de mes yeux vu, le détail des quantum dots. J'ai découvert des objets concrets, tellement bien imagés qu'on a l'impression de pouvoir les toucher. Merci pour toutes ces heures où nous avons patiemment cherché, localisé, zoomé, dézoomé les quantum dots uniques qui m'intéressaient. Il en va de même pour les manips avec toi, Patrick: merci pour ton aide pour le choix des grilles TEM, la dispersion des quantum dots, les observations corrélées en fluorescence et en TEM, les manips de diffraction aux rayons X, les explications concernant la structure cristalline.

Ivan, хвала ти! J'ai profité de ton aide sur le montage confocal, la mise en place de filtres, l'alignement des lasers (diode et supercontinuum), ainsi que des discussions sur les débouchés d'un profil d'ingénieur-chercheur (docteur maintenant) atypique comme le mien.

Thomas, tu as été le premier avec qui je pouvais discuter de mon modèle appliqué aux quantum dots, au détour de synthèses difficiles de coeur-coques CdSe/CdS. Ma perception du chemin des électrons, la façon dont il me fallait présenter mon modèle a beaucoup bénéficié de ces discussions. Merci!

Merci Cécile, merci Sylvain, pour les discussions au jour le jour, les petites attentions de collègues de bureau. Votre présence me manquera.

Je tiens à remercier Sandrine et Benoit M.. A mon arrivée, vous étiez les aînés, pratiquement en fin de thèse. Autour d'un premier café, vous m'avez donné envie d'intégrer cette équipe, et plus tard vous m'avez mis en confiance, grâce à vos explications concernant les synthèses des nanoplaquettes et quantum dots coeur-coque dont vous êtes les experts.

Clémentine, nos sujets étaient proches et j'ai profité de tes conseils, de ton aide sur la synthèse des coeurs-coques, des adaptatons du MicroTime. Merci!

Merci Benjamin pour les mesures et déterminations de taille de mes quantum dots en SAXS, alors que mes échantillons avaient souvent une concentration insuffisante.

Je tiens à te remercier Zackaria pour tout ce qui a fait que j'ai pu imager les mêmes dots uniques en microscopie optique et en TEM: les grilles marquées, les pièces sandwich, les manipulations de cathodo au LPS. Cela a aussi été un plaisir de discuter du modèle.

Merci aux collègues opticiens, chimistes, physiciens qui font qu'on vient travailler avec plaisir dans ce laboratoire qui couvre tous les aspects de la recherche sur les nanocristaux semi-conducteurs, unique en France. Merci Elsa, Nicolas, Sophie, Sylvia, Emerson, Brice, Emmanuel, Michel, Gary, Botao, Alexandra, Vincent, Eduardo, Pierre, Mariana, Eleonora, Mohamed, Zhuoyin, Stéphanie, Hadrien, Piernicola, Zhenhua, Wei, Anusuya, Martin, Aude, Adrien, Patrick, Chloé et stagiaires d'année en année.

J'aimerais remercier le personnel de la bibliothèque et de la reprographie. Catherine, merci de m'avoir inclus dans les actions de communication sur le libre accès aux publications. C'est un sujet important, non seulement pour les chercheurs et bibliothécaires mais également pour les curieux, qui pourtant financent ces recherches à travers leur impôts. Lorsque je n'étais pas encore affilié à une institution comme l'ESPCI ou l'UPMC, j'avais beaucoup de mal à accéder à certaines publications.

Merci à toute l'équipe de l'Espace Pierre Gilles de Gennes, en particulier Richard-Emmanuel, Matteo, Virginie, Laurène, qui m'ont permis de communiquer au grand public certains aspects de mes recherches sur les quantum dots. Merci Alexis et Guillaume, à qui j'ai eu le plaisir d'expliquer mes travaux très bien mis en valeur pour l'exposition "Têtes chercheurses". De même, je remercie Danica d'avoir écrit un billet de blog à ce sujet.

Je remercie également les compagnons de déjeuner, de cafés ou de soirées étudiantes, bowling ou poker, partageant le même sort de thésard : Pierre, Emilie, Marc, Ariadna, Daria, Baptiste, Olivier. Si tie, Mihaela, iti multumesc atat ca am putut discuta despre teoria mea, cat si pentru faptul ca m-ai initiat intr-o noua limba si cultura. Iti multumesc Oliviei pentru cuvintele pozitive la adresa muncii mele. Sa nu uit sa le multumesc profesoarei si colegei de banca de la ICR - Doina, Stéphanie, Corinne, Clara, Patrice, Roland, Yves si alte - cu care am putut sa impartasesc experientele de cercetator si impreuna cu care am invatat o noua limba.

Je te remercie tout particulièrement Salwa pour l'intérêt que tu as porté à mon travail. Tu es toujours aussi enthousiaste quand je t'expose un de mes nouveaux projets.

I would also like to thank Alexander and Eva for discussing new physics during this thesis. The umbrellas have been used by different people of the lab, very useful in autumnal Paris.

Merci également à Christine Allais, Guy Berthault, Philippe Laurier, Jean-Bernard Deloly, Jean-Christophe Delville de m'avoir permis de discuter régulièrement d'aspects plus fondamentaux de la physique. Les phénomènes naturels, les données de l'expérience recèlent encore de nombreuses découvertes potentielles.

Merci à ceux qui sont venus assister à ma soutenance, Claude, Fabrice, Damien, ceux que je connais moins bien, ceux que je ne connaissais pas (encore). Cette soutenance clôture un moment important de ma vie.

Et je remercie tout spécialement Tai. J'aime à dire que cette thèse a réellement commencé en 1990, lorsque tu me parlais de modéliser la matière avec des bipoints, des objets étendus et non des objets ponctuels. Je trouvais cela tellement élégant et cela me permettait d'aborder les phénomènes physiques de façon tellement intuitive que cela me travaille depuis 23 ans. Ce manuscrit de thèse, s'il n'est pas l'aboutissement de cette quête, en est une étape importante.

Merci à ceux qui ont croisé ma route pendant toutes ces années et qui m'ont soutenu dans ce projet, par un encouragement, par un intérêt pour mes idées. Ceux que je connais depuis plus longtemps et ceux rencontrés ces trois dernières années. Je pense à Monsieur Zerr, à Ivan. Ik denk ook aan Arnaud, Rogier. Les collègues de ma période Colas, Guillaume, Damien, Loïc, Caroline, ceux de ma période SFR, Ali, Rodolphe, Eric, Lotfi ... J'aimerais en citer plein d'autres...

Merci à mes beaux-parents, à ma belle-famille, pour leur présence régulière à mes côtés, pour les attentions qui permettent de traverser toutes ces années sereinement.

En een speciale dank aan mijn ouders, broer, zus, schoonzus, zwager, en verdere familie. Ik vond het heel leuk Pa, Ma, Nathalie en Yannick dat jullie overgekomen zijn voor de promotie. Ook aan diegenen die vanuit ons kikkerland mijn promotieonderzoek gevolgd hebben.

Een flinke dank aan de vertegenwoordigers van de volgende generatie. Brice, Arnaud, Ella, elke dag geniet ik van jullie!

Et tout ce travail effectué ne serait rien sans Laurence, ma compagne de tous les jours. Un grand merci! Merci de m'avoir accompagné, de continuer à m'assister pour ce projet en dehors des chemins battus. Ton aide m'est toujours extrêmement précieuse.

Chatou, 20 octobre 2013

Bibliography

[1] P. Michler, A. Kiraz, C. Becher, W. V. Schoenfeld, P. M. Petroff, L. Zhang, E. Hu, and A. Imamoglu, "A quantum dot single-photon turnstile device," *Science*, vol. 290, pp. 2282–2285, Dec. 2000.

[2] A. Beveratos, R. Brouri, T. Gacoin, A. Villing, J.-P. Poizat, and P. Grangier, "Single Photon Quantum Cryptography," *Physical Review Letters*, vol. 89, p. 187901, Oct. 2002.

[3] H.-J. Eisler, V. C. Sundar, M. G. Bawendi, M. Walsh, H. I. Smith, and V. Klimov, "Color-selective semiconductor nanocrystal laser," *Applied Physics Letters*, vol. 80, no. 24, p. 4614, 2002.

[4] S. Strauf, K. Hennessy, M. Rakher, Y.-S. Choi, A. Badolato, L. Andreani, E. Hu, P. Petroff, and D. Bouwmeester, "Self-Tuned Quantum Dot Gain in Photonic Crystal Lasers," *Physical Review Letters*, vol. 96, p. 127404, Mar. 2006.

[5] S. Coe, W.-K. Woo, M. G. Bawendi, and V. Bulović, "Electroluminescence from single monolayers of nanocrystals in molecular organic devices," *Nature*, vol. 420, no. 6917, pp. 800–803, 2002.

[6] M. Bruchez, M. Moronne, P. Gin, S. Weiss, and A. P. Alivisatos, "Semiconductor nanocrystals as fluorescent biological labels," *Science*, vol. 281, no. 5385, pp. 2013–2016, 1998.

[7] B. Dubertret, P. Skourides, D. J. Norris, V. Noireaux, A. H. Brivanlou, and A. Libchaber, "In vivo imaging of quantum dots encapsulated in phospholipid micelles," *Science*, vol. 298, no. 5599, pp. 1759–1762, 2002.

[8] A. J. Nozik, "Quantum dot solar cells," *Physica E: Low-dimensional Systems and Nanostructures*, vol. 14, pp. 115–120, Apr. 2002.

[9] B. Mahler, P. Spinicelli, S. Buil, X. Quelin, J.-P. Hermier, and B. Dubertret, "Towards non-Blinking colloidal quantum dots," *Nature Materials*, vol. 7, pp. 659–664, June 2008.

[10] S. Ithurria, M. D. Tessier, B. Mahler, R. P. S. M. Lobo, B. Dubertret, and A. L. Efros, "Colloidal nanoplatelets with two-dimensional electronic structure," *Nature Materials*, vol. 10, pp. 936–941, Oct. 2011.

[11] C. Javaux, B. Mahler, B. Dubertret, A. Shabaev, A. V. Rodina, A. L. Efros, D. R. Yakovlev, F. Liu, M. Bayer, G. Camps, L. Biadala, S. Buil, X. Quelin,

and J.-P. Hermier, "Thermal activation of non-radiative Auger recombination in charged colloidal nanocrystals," *Nature nanotechnology*, vol. 8, pp. 206–212, Feb. 2013.

[12] B. Mahler, N. Lequeux, and B. Dubertret, "Ligand-controlled polytypism of thick-shell CdSe/CdS nanocrystals.," *Journal of the American Chemical Society*, vol. 132, pp. 953–9, Jan. 2010.

[13] C. Javaux, *Étude de la réduction du phénomène de clignotement dans les nanocristaux semi-conducteurs de CdSe/CdS à coque épaisse*. PhD thesis, ESPCI, 2012.

[14] M. Faraday, *Experimental Researches in Electricity*. London: Bernard Quaritch, 1839.

[15] G. Busch, "Early history of the physics and chemistry of semiconductors-from doubts to fact in a hundred years," *European Journal of Physics*, vol. 10, pp. 254–264, 1989.

[16] T. Jenkins, "A brief history of ... semiconductors," *Physics Education*, vol. 40, pp. 430–439, Sept. 2005.

[17] J. W. Hittorf, "Ueber die Allotropie des Selens," *Annalen der Physik und Chemie*, vol. 84, pp. 214–220, 1851.

[18] J. W. Hittorf, "Ueber das elektrische Leitungsvermögen des Schwefelsilbers und Halbschewelkupfers," *Annalen der Physik und Chemie*, vol. 84, pp. 1–28, 1851.

[19] E. Becquerel, "Mémoire sur les effets électriques produits sous l'influence des rayons solaires," *Comptes rendus de l'Académie des sciences*, vol. 9, no. 19, pp. 561–567, 1839.

[20] W. Smith, "The action of light on selenium," *Journal of the Society of Telegraph Engineers*, vol. 2, no. 4, pp. 31–33, 1873.

[21] M. E. Levinshtein and G. S. Simin, *Getting to Know Semiconductors*. Singapore: World Scientific, 1992.

[22] A. G. Bell, "On the Production and Reproduction of Speech by Light," *American Journal of Science*, vol. 20, no. 118, pp. 305–311, 1880.

[23] W. G. Adams and R. E. Day, "The Action of Light on Selenium," *Proceedings of the Royal Society of London A*, vol. 25, pp. 113–117, 1876.

[24] C. E. Fritts, "New form of selenium cell, with some remarkable electrical discoveries made by its use," *American Association for the Advancement of Science, Proceedings*, vol. 32, p. 128, 1883.

[25] C. E. Fritts, "On the Fritts selenium celles and batteries," *American Association for the Advancement of Science, Proceedings*, vol. 33, pp. 97–108, 1884.

[26] C. F. Braun, "Ueber die Stromleitung durch Schwefelmetalle," *Annalen der Physik und Chemie*, vol. 153, pp. 556–563, 1874.

[27] A. Schuster, "On Unilateral Conductivity," *Philosophical Magazine Series 4*, vol. 48, no. 318, pp. 251–257, 1874.

[28] J. Lilienfeld, "Method and Apparatus for Controlling Electric Currents," 1930.

[29] B. Valeur and M. Berberan-Santos, "A brief history of fluorescence and phosphorescence before the emergence of quantum theory," *Journal of Chemical Education*, vol. 88, no. 6, pp. 731–738, 2011.

[30] T. Sidot, "Sur les propriétés de la blende hexagonale," *Comptes rendus de l'Académie des sciences*, vol. 63, pp. 188–189, 1866.

[31] H. J. Round, "A Note on Carborundum," *Electrical World*, vol. 49, no. 6, p. 309, 1907.

[32] O. V. Losev, "Luminous carborundum [silicon carbide] detector and detection with crystals," *Telegrafiya i Telefoniya bez Provodov*, vol. 44, pp. 485–494, 1927.

[33] N. Holonyak and S. F. Bevacqua, "Coherent (Visible) Light Emission from Ga(As(1-x)Px) Junctions," *Applied Physics Letters*, vol. 1, no. 4, p. 82, 1962.

[34] Z. I. Alferov, "The history and future of semiconductor heterostructures," *Semiconductors*, vol. 32, pp. 1–14, Jan. 1998.

[35] B. Lojek, *History of Semiconductor Engineering*. Springer-Verlag Berlin Heidelberg, 2007.

[36] P. R. Morris, *A history of the world semiconductor industry*, vol. 12. Institution Of Engineering And Technology, 1990.

[37] R. P. Feynman, "There's plenty of room at the bottom," *Miniaturization (HD Gilbert, ed.) Reinhold, New York*, 1961.

[38] M. J. O. Strutt, "Zur Wellenmechanik des Atomgitters," *Annalen der Physik*, vol. 391, no. 10, pp. 319–324, 1928.

[39] F. Bloch, "Über die quantenmechanik der elektronen in kristallgittern," *Zeitschrift für physik*, vol. 52, no. 7-8, pp. 555–600, 1929.

[40] W. Pauli, *Wissenschaftlicher Briefwechsel mit Bohr, Einstein, Heisenberg ua/Scientific Correspondence with Bohr, Einstein, Heisenberg ao: Band/Volume 3: 1940-1949*, vol. 2. Springer, 1993.

[41] A. H. Wilson, "The theory of electronic semi-conductors," *Proceedings of the Royal Society of London. Series A, Containing Papers of a Mathematical and Physical Character*, vol. 133, no. 822, pp. 458–491, 1931.

[42] J. Frenkel, "On the solid body model of heavy nuclei," *Phys. Z. Soviet Union*, vol. 9, p. 158, 1936.

[43] G. Wannier, "The structure of electronic excitation levels in insulating crystals," *Physical Review*, vol. 52, no. 3, pp. 191–197, 1937.

[44] N. W. Ashcroft and N. D. Mermin, *Solid State Physics*. 1976.

[45] E. Gross, "Excitons and their motion in crystal lattices," *Physics-Uspekhi*, vol. 5, no. 2, pp. 195–218, 1962.

[46] P. Harrison, *Quantum Wells, Wires and Dots*. 2005.

[47] G. G. Stokes, "On the change of refrangibility of light," *Philosophical Transactions of the Royal Society of London*, vol. 142, no. May, pp. 463–562, 1852.

[48] R. A. Smith, "The electronic and optical properties of the lead sulphide group of semi-conductors," *Physica*, vol. 3, no. 7-12, pp. 910–929, 1954.

[49] R. Dingle, W. Wiegmann, and C. H. Henry, "Quantum States of Confined Carriers in Very Thin AlxGa(1-x)As-GaAs-AlxGa(1-x)As Heterostructures," *Physical Review Letters*, vol. 33, no. 14, pp. 827–830, 1974.

[50] G. Bastard, E. Mendez, L. Chang, and L. Esaki, "Exciton binding energy in quantum wells," *Physical Review B*, vol. 26, no. 4, pp. 1974–1979, 1982.

[51] H. Kishishita, "Optical Properties of Cu-Complex Centres in KCl Single Crystals," *Physica Status Solidi (B)*, vol. 55, no. 1, pp. 399–406, 1973.

[52] T. Tsuboi, "Absorption spectra of heavily Cu+-doped KCl, SrCl2 and KI crystals," *The Journal of Chemical Physics*, vol. 72, no. 10, p. 5343, 1980.

[53] T. Itoh and T. Kirihara, "Excitons in CuCl microscrystals embedded in NaCl," *Journal of Luminescence*, vol. 31-2, no. Dec, pp. 120–122, 1984.

[54] A. I. Ekimov, A. A. Onushchenko, and V. A. Tzehomskii, "Eksitonnoye pogloshcheniye kristallami CuCl v stekloobraznoy matritse," *Fizika i khimiya stekla*, vol. 6, no. 4, pp. 511–512, 1980.

[55] A. I. Ekimov and A. A. Onushchenko, "Quantum size oscillations of interband absorption in CdS microcrystals," in *Proc. of IX All-Union Conf. on Phys. of Semiconductors, v.2, I76 (1982). Editor(s): Abdullaev, G.B., Publisher: Elm, Baku, USSR I76*, vol. 76, pp. 76–77, 1982.

[56] A. I. Ekimov and A. A. Onushchenko, "Quantum size effect in the optical spectra of semiconductor microcrystals," *Soviet Physics Semiconductors USSR*, vol. 16, no. 7, pp. 775–778, 1982.

[57] A. L. Efros and A. L. Efros, "Interband absorption of light in a semiconductor sphere," *Soviet Physics Semiconductors USSR*, vol. 16, no. 7, pp. 772–775, 1982.

[58] A. Henglein, "Photo-Degradation and Fluorescence of Colloidal-Cadmium Sulfide in Acqueous-Solution," *Berichte Der Bunsen-Gesellschaft-Physical Chemistry Chemical Physics*, vol. 86, no. 4, pp. 301–305, 1982.

[59] H. Weller, U. Koch, M. Gutierrez, and A. Henglein, "Photochemistry of Colloidal Metal Sulfides .7. Absorption and Fluorescence of Extremely Small ZnS

Particles - The World of the Neglected Dimensions," *Berichte Der Bunsen-Gesellschaft-Physical Chemistry Chemical Physics*, vol. 88, no. 7, pp. 649–656, 1984.

[60] L. E. Brus, "A simple model for the ionization potential, electron affinity, and aqueous redox potentials of small semiconductor crystallites," *The Journal of Chemical Physics*, vol. 79, no. 11, p. 5566, 1983.

[61] C. B. Murray, D. J. Norris, and M. G. Bawendi, "Synthesis and characterization of nearly monodisperse CdE (E = sulfur, selenium, tellurium) semiconductor nanocrystallites," *Journal of the American Chemical Society*, vol. 115, no. 19, pp. 8706–8715, 1993.

[62] D. J. Norris and M. G. Bawendi, "Measurement and assignment of the size-dependent optical spectrum in CdSe quantum dots," *Physical Review B*, vol. 53, pp. 16338–16346, June 1996.

[63] U. Banin, C. J. Lee, A. A. Guzelian, A. V. Kadavanich, A. P. Alivisatos, W. Jaskolski, G. W. Bryant, A. L. Efros, and M. Rosen, "Size-dependent electronic level structure of InAs nanocrystal quantum dots: Test of multiband effective mass theory," *The Journal of Chemical Physics*, vol. 109, no. 6, p. 2306, 1998.

[64] M. A. Hines and P. Guyot-Sionnest, "Synthesis and Characterization of Strongly Luminescing ZnS-Capped CdSe Nanocrystals," *The Journal of Physical Chemistry*, vol. 100, pp. 468–471, Jan. 1996.

[65] X. Peng, L. Manna, W. Yang, J. Wickham, E. Scher, A. V. Kadavanich, and A. P. Alivisatos, "Shape control of CdSe nanocrystals," *Nature*, vol. 404, pp. 59–61, Mar. 2000.

[66] L. Liu, Z. Zhuang, T. Xie, Y.-G. Wang, J. Li, Q. Peng, and Y. Li, "Shape control of CdSe nanocrystals with zinc blende structure," *Journal of the American Chemical Society*, vol. 131, pp. 16423–9, Nov. 2009.

[67] R. Costi, A. E. Saunders, and U. Banin, "Colloidal hybrid nanostructures: a new type of functional materials.," *Angewandte Chemie (International ed. in English)*, vol. 49, pp. 4878–97, July 2010.

[68] J. S. Son, K. Park, S. G. Kwon, J. Yang, M. K. Choi, J. Kim, J. H. Yu, J. Joo, and T. Hyeon, "Dimension-controlled synthesis of CdS nanocrystals: from 0D quantum dots to 2D nanoplates," *Small*, vol. 8, pp. 2394–402, Aug. 2012.

[69] C. B. Murray, S. Sun, W. Gaschler, H. Doyle, T. a. Betley, and C. R. Kagan, "Colloidal synthesis of nanocrystals and nanocrystal superlattices," *IBM Journal of Research and Development*, vol. 45, pp. 47–56, Jan. 2001.

[70] W. H. Evers, B. D. Nijs, L. Filion, S. Castillo, M. Dijkstra, and D. Vanmaekelbergh, "Entropy-Driven Formation of Binary Semiconductor-Nanocrystal Superlattices," *Nano Letters*, vol. 10, pp. 4235–4241, Sept. 2010.

[71] A. Chaplik, "Electronic properties of quantum points," *JETP Letters*, vol. 50, no. 1, pp. 44–47, 1989.

[72] R. Tsu and L. Esaki, "Tunneling in a finite superlattice," *Applied Physics Letters*, vol. 22, no. 11, p. 562, 1973.

[73] A. L. Efros and M. Rosen, "The Electronic Structure of Semiconductor Nanocrystals," *Annual Review of Materials Science*, vol. 30, pp. 475–521, Aug. 2000.

[74] L. D. Landau and E. M. Lifshitz, *Quantum Mechanics: Non-Relativistic Theory*. 1977.

[75] Y. Kayanuma and H. Momiji, "Incomplete confinement of electrons and holes in microcrystals," *Physical Review B*, vol. 41, no. 14, pp. 261–263, 1990.

[76] G. Einevoll, "Confinement of excitons in quantum dots," *Physical Review B*, vol. 45, no. 7, pp. 3410–3417, 1992.

[77] L. E. Brus, "Electron-electron and electron-hole interactions in small semiconductor crystallites: The size dependence of the lowest excited electronic state," *The Journal of Chemical Physics*, vol. 80, pp. 4403–4409, 1984.

[78] L. E. Brus, "On the development of bulk optical properties in small semiconductor crystallites," *Journal of Luminescence*, vol. 31-32, pp. 381–384, Dec. 1984.

[79] E. A. Hylleraas, "Neue Berechnung der Energie des Heliums im Grundzustande, sowie des tiefsten Terms von Ortho-Helium," *Zeitschrift für Physik*, vol. 54, pp. 347–366, 1929.

[80] Y. Kayanuma, "Wannier exciton in microcrystals," *Solid state communications*, vol. 59, no. 6, pp. 405–408, 1986.

[81] R. Romestain and G. Fishman, "Excitonic wave function, correlation energy, exchange energy, and oscillator strength in a cubic quantum dot," *Physical Review B*, vol. 49, no. 3, pp. 1774–1781, 1994.

[82] Y. Kayanuma and H. Momiji, "Quantum-size effects of interacting electrons and holes in semiconductor microcrystals with spherical shape," *Physical Review B*, vol. 38, no. 14, p. 9797, 1988.

[83] H. Schmidt and H. Weller, "Quantum size effects in semiconductor crystallites: calculation of the energy spectrum for the confined exciton," *Chemical physics letters*, vol. 129, no. 6, pp. 615–618, 1986.

[84] S. Nair, S. Sinha, and K. Rustagi, "Quantum size effects in spherical semiconductor microcrystals," *Physical Review B*, vol. 35, no. 8, pp. 4098–4101, 1987.

[85] D. J. Norris, A. L. Efros, M. Rosen, and M. G. Bawendi, "Size dependence of exciton fine structure in CdSe quantum dots.," *Physical Review B*, vol. 53, pp. 16347–16354, June 1996.

[86] P. Lippens and M. Lannoo, "Calculation of the band gap for small CdS and ZnS crystallites," *Physical Review B*, vol. 39, no. 15, pp. 10935–10942, 1989.

[87] C. Delerue, G. Allan, and M. Lannoo, "Theoretical aspects of the luminescence of porous silicon," *Physical Review B*, vol. 48, no. 15, pp. 24–36, 1993.

[88] S. Pokrant and K. Whaley, "Tight-binding studies of surface effects on electronic structure of CdSe nanocrystals: the role of organic ligands, surface reconstruction, and inorganic capping shells," *The European Physical Journal D-Atomic, Molecular, Optical and Plasma Physics*, vol. 6, no. 2, pp. 255–267, 1999.

[89] A. K. Bhattacharjee and J. Pérez-Conde, "Electronic structure of CdTe nanocrystals : a tight-binding study," *Solid State Communications*, vol. 110, pp. 259–264, 1999.

[90] G. Allan and C. Delerue, "Confinement effects in PbSe quantum wells and nanocrystals," *Physical Review B*, vol. 70, p. 245321, Dec. 2004.

[91] G. Allan and C. Delerue, "Tight-binding calculations of the optical properties of HgTe nanocrystals," *Physical Review B*, vol. 86, p. 165437, Oct. 2012.

[92] G. Dresselhaus, "Spin-orbit coupling effects in zinc blende structures," *Physical Review*, vol. 100, no. 2, pp. 580–586, 1955.

[93] R. J. Elliott, "Spin-Orbit Coupling in Band Theory-Character Tables for Some "Double" Space Groups," *Physical Review*, vol. 17, no. 1936, pp. 280–287, 1954.

[94] A. Baldereschi and N. Lipari, "Energy levels of direct excitons in semiconductors with degenerate bands," *Physical Review B*, vol. 1362, no. 1955, pp. 439–451, 1971.

[95] A. I. Ekimov, A. A. Onushchenko, A. Plyukhin, and A. L. Efros, "Size quantization of excitons and determination of the parameters of their energy spectrum in CuCl," *Sov. Phys. JETP*, vol. 61, no. 4, pp. 891–897, 1985.

[96] N. Chestnoy, R. Hull, and L. E. Brus, "Higher excited electronic states in clusters of ZnSe, CdSe, and ZnS: Spin-orbit, vibronic, and relaxation phenomena," *The Journal of Chemical Physics*, vol. 85, no. 4, p. 2237, 1986.

[97] J. Xia, "Electronic structures of zero-dimensional quantum wells," *Physical Review B*, vol. 40, no. 12, pp. 8500–8507, 1989.

[98] M. Nirmal, D. Norris, M. Kuno, M. G. Bawendi, A. Efros, and M. Rosen, "Observation of the "Dark exciton" in CdSe quantum dots.," Nov. 1995.

[99] S. Brovelli, R. D. Schaller, S. A. Crooker, F. García-Santamaría, Y. Chen, R. Viswanatha, J. a. Hollingsworth, H. Htoon, and V. I. Klimov, "Nano-engineered electron-hole exchange interaction controls exciton dynamics in core-shell semiconductor nanocrystals," *Nature communications*, vol. 2, p. 280, Jan. 2011.

[100] C. Kittel, *Quantum Theory of Solids (Second Revised Printing ed.)*. New York: Wiley, 1987.

[101] E. Kane, "Band structure of indium antimonide," *Journal of Physics and Chemistry of Solids*, vol. 1, no. 4, pp. 249–261, 1957.

[102] J. Luttinger and W. Kohn, "Motion of electrons and holes in perturbed periodic fields," *Physical Review*, vol. 173, no. 1950, pp. 869–883, 1955.

[103] C. Pidgeon and R. Brown, "Interband magneto-absorption and Faraday rotation in InSb," *Physical Review*, vol. 15, no. 1959, 1966.

[104] P. Sercel and K. Vahala, "Analytical formalism for determining quantum-wire and quantum-dot band structure in the multiband envelope-function approximation," *Physical Review B*, vol. 42, no. 6, pp. 3690–3710, 1990.

[105] J. P. Proot, C. Delerue, and G. Allan, "Electronic structure and optical properties of silicon crystallites: Application to porous silicon," *Applied Physics Letters*, vol. 61, no. 16, p. 1948, 1992.

[106] L. W. Wang and A. Zunger, "Pseudopotential calculations of nanoscale CdSe quantum dots," *Physical Review B*, vol. 53, pp. 9579–9582, Apr. 1996.

[107] Y. Chang, "Bond-orbital models for superlattices," *Physical Review B*, vol. 37, no. 14, pp. 8215–8222, 1988.

[108] A. Tomasulo and M. V. Ramakrishna, "Quantum confinement effects in semiconductor clusters. II," *The Journal of Chemical Physics*, vol. 105, no. 9, p. 3612, 1996.

[109] C. Q. Sun, "Size dependence of nanostructures: Impact of bond order deficiency," *Progress in Solid State Chemistry*, vol. 35, no. 1, pp. 1–159, 2007.

[110] Y. A. Yang, H. Wu, K. R. Williams, and Y. C. Cao, "Synthesis of CdSe and CdTe nanocrystals without precursor injection," *Angewandte Chemie (International ed. in English)*, vol. 44, no. 41, pp. 6712–5, 2005.

[111] V. K. LaMer and R. H. Dinegar, "Theory, Production and Mechanism of Formation of Monodispersed Hydrosols," *Journal of the American Chemical Society*, vol. 72, no. 11, pp. 4847–4854, 1950.

[112] X. Peng, J. Wickham, and A. P. Alivisatos, "Kinetics of II-VI and III-V Colloidal Semiconductor Nanocrystal Growth: "Focusing" of Size Distributions," *Journal of the American Chemical Society*, vol. 120, pp. 5343–5344, June 1998.

[113] O. Carion, B. Mahler, T. Pons, and B. Dubertret, "Synthesis, encapsulation, purification and coupling of single quantum dots in phospholipid micelles for their use in cellular and in vivo imaging," *Nature Protocols*, vol. 2, no. 10, pp. 2383–2390, 2007.

[114] W. W. Yu, L. Qu, W. Guo, and X. Peng, "Experimental Determination of the Extinction Coefficient of CdTe, CdSe, and CdS Nanocrystals," *Chemistry of Materials*, vol. 15, pp. 2854–2860, July 2003.

[115] J. Jasieniak, L. Smith, J. V. Embden, and P. Mulvaney, "Re-examination of the Size-Dependent Absorption Properties of CdSe Quantum Dots," *Society*, pp. 19468–19474, 2009.

[116] C. de Mello Donegá and R. Koole, "Size Dependence of the Spontaneous Emission Rate and Absorption Cross Section of CdSe and CdTe Quantum Dots," *The Journal of Physical Chemistry C*, vol. 113, pp. 6511–6520, Apr. 2009.

[117] R. Karel Capek, I. Moreels, K. Lambert, D. De Muynck, Q. Zhao, A. Van Tomme, F. Vanhaecke, and Z. Hens, "Optical Properties of Zincblende Cadmium Selenide Quantum Dots," *The Journal of Physical Chemistry C*, vol. 114, no. 14, pp. 6371–6376, 2010.

[118] Q. Wang and D.-K. Seo, "Synthesis of Deep-Red-Emitting CdSe Quantum Dots and General Non-Inverse-Square Behavior of Quantum Confinement in CdSe Quantum Dots," *Chemistry of Materials*, no. 20, pp. 5764–5767, 2006.

[119] C. A. Leatherdale, W.-K. Woo, F. V. Mikulec, and M. G. Bawendi, "On the Absorption Cross Section of CdSe Nanocrystal Quantum Dots," *The Journal of Physical Chemistry B*, vol. 106, pp. 7619–7622, Aug. 2002.

[120] D. Underwood, T. Kippeny, and S. J. Rosenthal, "Ultrafast carrier dynamics in CdSe nanocrystals determined by femtosecond fluorescence upconversion spectroscopy," *J. Phys. Chem. B*, vol. 105, no. 2, pp. 436–443, 2001.

[121] X. Peng, "Mechanisms for the Shape-Control and Shape-Evolution of Colloidal Semiconductor Nanocrystals," *Advanced Materials*, vol. 15, pp. 459–463, Mar. 2003.

[122] C. Javaux, B. Mahler, M. Nasilowski, A. Dijksman, P. Bassoul, X. Xu, and B. Dubertret, "Rapid, easy and robust synthesis of very thick shell CdSe/CdS colloidal nanocrystals using continuous injection of precursors," *in preparation*, 2013.

[123] S. Ithurria and B. Dubertret, "Quasi 2D Colloidal CdSe Platelets with Thicknesses Controlled at the Atomic Level.," *J. Am. Chem. Soc.*, vol. 130, pp. 16504–5, Nov. 2008.

[124] M. D. Tessier, C. Javaux, I. Maksimovic, V. Loriette, and B. Dubertret, "Spectroscopy of Single CdSe Nanoplatelets," *ACS nano*, vol. 6, pp. 6751–8, Aug. 2012.

[125] B. Mahler, N. Lequeux, and B. Dubertret, "Ligand-controlled polytypism of thick-shell CdSe/CdS nanocrystals," *Journal of the American Chemical Society*, vol. 132, pp. 953–9, Jan. 2010.

[126] A. V. Malko, Y.-S. Park, S. Sampat, C. Galland, J. Vela, Y. Chen, J. A. Hollingsworth, V. I. Klimov, and H. Htoon, "Pump-Intensity- and Shell-Thickness-Dependent Evolution of Photoluminescence Blinking in Individual Core/Shell CdSe/CdS Nanocrystals," *Nano letters*, vol. 11, no. 12, pp. 5213–5218, 2011.

[127] Picoquant, "New Time-Resolved Inverted Microscope MicroTime 200 - Product Release Note," *Journal of fluorescence*, vol. 13, no. 3, pp. 287–288, 2003.

[128] M. Nirmal, B. O. Dabbousi, M. G. Bawendi, J. J. Macklin, J. K. Trautman, T. D. Harris, and L. E. Brus, "Fluorescence intermittency in single cadmium selenide nanocrystals," *Nature*, vol. 383, no. 6603, pp. 802–804, 1996.

[129] P. Spinicelli, S. Buil, X. Quélin, B. Dubertret, B. Mahler, and J.-P. Hermier, "Bright and Grey States in CdSe-CdS Nanocrystals Exhibiting Strongly Reduced Blinking," *Phys. Rev. Lett.*, vol. 102, p. 136801, Apr. 2009.

[130] C. Galland, S. Brovelli, W. K. Bae, L. A. Padilha, F. Meinardi, and V. I. Klimov, "Dynamic Hole Blockade Yields Two-Color Quantum and Classical Light from Dot-in-Bulk Nanocrystals," *Nano letters*, Dec. 2012.

[131] A. P. Alivisatos, "Perspectives on the Physical Chemistry of Semiconductor Nanocrystals," *The Journal of Physical Chemistry*, vol. 100, pp. 13226–13239, Jan. 1996.

[132] Y. Ebenstein, T. Mokari, and U. Banin, "Fluorescence quantum yield of CdSe/ZnS nanocrystals investigated by correlated atomic-force and single-particle fluorescence microscopy," *Applied Physics Letters*, vol. 80, no. 21, p. 4033, 2002.

[133] F. Koberling, A. Mews, G. Philipp, U. Kolb, I. Potapova, M. Burghard, and T. Basché, "Fluorescence spectroscopy and transmission electron microscopy of the same isolated semiconductor nanocrystals," *Applied Physics Letters*, vol. 81, no. 6, p. 1116, 2002.

[134] F. Koberling, U. Kolb, G. Philipp, I. Potapova, T. Basché, and A. Mews, "Fluorescence Anisotropy and Crystal Structure of Individual Semiconductor Nanocrystals," *The Journal of Physical Chemistry B*, vol. 107, pp. 7463–7471, July 2003.

[135] C. Querner, S. Wang, K. Healy, J. A. Fairfield, M. D. Fischbein, and M. Drndic, "Fluorescence Dynamics of Semiconductor Nanorod Clusters Studied by Correlated Atomic Force, Transmission Electron, and Fluorescence Microscopy," *The Journal of Physical Chemistry C*, vol. 112, pp. 19945–19956, Dec. 2008.

[136] L. F. Zagonel, S. Mazzucco, M. Tencé, K. March, R. Bernard, B. Laslier, G. Jacopin, M. Tchernycheva, L. Rigutti, F. H. Julien, R. Songmuang, and M. Kociak, "Nanometer scale spectral imaging of quantum emitters in nanowires and its correlation to their atomically resolved structure," *Nano letters*, vol. 11, pp. 568–573, Feb. 2011.

[137] D. Canneson, I. Mallek-Zouari, S. Buil, X. Quélin, C. Javaux, B. Mahler, B. Dubertret, and J.-P. Hermier, "Strong Purcell effect observed in single thick-shell CdSe/CdS nanocrystals coupled to localized surface plasmons," *Physical Review B*, vol. 84, pp. 1–6, Dec. 2011.

[138] S. Jander, A. Kornowski, and H. Weller, "Energy Transfer from CdSe/CdS Nanorods to Amorphous Carbon.," *Nano letters*, vol. 11, pp. 5179–83, Dec. 2011.

[139] S. J. Leblanc, M. R. McClanahan, M. Jones, and P. J. Moyer, "Enhancement of Multiphoton Emission from Single CdSe Quantum Dots Coupled to Gold Films," *Nano letters*, Mar. 2013.

[140] S. Jin, N. Song, and T. Lian, "Suppressed blinking dynamics of single QDs on ITO," *ACS nano*, vol. 4, pp. 1545–52, Mar. 2010.

[141] Z. Mahfoud, A. Dijksman, C. Javaux, P. Bassoul, A.-L. Baudrion, J. Plain, B. Dubertret, and M. Kociak, "Cathodoluminescence in a Scanning Transmission Electron Microscope: a nanometre counterpart of Photoluminescence for the study of II-VI Quantum Dots.," *in preparation*, pp. 1–10, 2013.

[142] A. Al Salman, A. Tortschanoff, M. B. Mohamed, D. Tonti, F. van Mourik, and M. Chergui, "Temperature effects on the spectral properties of colloidal CdSe nanodots, nanorods, and tetrapods," *Applied Physics Letters*, vol. 90, no. 9, p. 093104, 2007.

[143] M. Fernée, T. Plakhotnik, Y. Louyer, B. N. Littleton, C. Potzner, P. Tamarat, P. Mulvaney, and B. Lounis, "Spontaneous spectral diffusion in CdSe quantum dots," *The Journal of Physical Chemistry Letters*, vol. 3, pp. 1716–1720, 2012.

[144] B. Mahler, B. Nadal, C. Bouet, G. Patriarche, and B. Dubertret, "Core/Shell colloidal semiconductor nanoplatelets," *Journal of the American Chemical Society*, vol. 134, pp. 18591–8, Nov. 2012.

[145] G. D. Scholes and G. Rumbles, "Excitons in nanoscale systems," *Nature Materials*, vol. 5, no. September, pp. 683–696, 2006.

[146] D. F. Styer, M. S. Balkin, K. M. Becker, M. R. Burns, C. E. Dudley, S. T. Forth, J. S. Gaumer, M. A. Kramer, D. C. Oertel, L. H. Park, M. T. Rinkoski, C. T. Smith, and T. D. Wotherspoon, "Nine formulations of quantum mechanics," *American Journal of Physics*, vol. 70, no. 3, pp. 288–297, 2002.

[147] R. P. Feynman, *QED: The Strange Theory of Light and Matter*. Princeton University Press, 1985.

[148] A. T. Dijksman and B. Dubertret, "Accurate Energy-Size Dependence of Excitonic Transitions in Semiconductor Nanocrystals and Nanoplatelets Using a Phase Jump Approach," *in preparation*, 2013.

[149] A. I. Ekimov and A. A. Onushchenko, "Quantum Size Effect in 3-Dimensional Microscopic Semiconductor Crystals," *JETP Letters*, vol. 34, no. 6, pp. 345–349, 1981.

[150] L. E. Brus, "A simple model for the ionization potential, electron affinity, and aqueous redox potentials of small semiconductor crystallites," *The Journal of Chemical Physics*, vol. 79, no. 11, p. 5566, 1983.

[151] A. P. Alivisatos, "Semiconductor clusters, nanocrystals, and quantum dots," *Science*, vol. 271, no. 5251, p. 933, 1996.

[152] K. Leung, S. Pokrant, and K. B. Whaley, "Exciton fine structure in CdSe nanoclusters," *Physical Review B*, vol. 57, no. 19, 1998.

[153] S. Sapra and D. Sarma, "Evolution of the electronic structure with size in II-VI semiconductor nanocrystals," *Physical Review B*, vol. 69, no. 12, pp. 1–7, 2004.

[154] A. Franceschetti, H. Fu, L. W. Wang, and A. Zunger, "Many-body pseudopotential theory of excitons in InP and CdSe quantum dots," *Physical Review B*, vol. 60, no. 3, pp. 1819–1829, 1999.

[155] J. Hu, L. W. Wang, L.-S. Li, W. D. Yang, and A. P. Alivisatos, "Semiempirical pseudopotential calculation of electronic states of CdSe quantum rods," *Journal of Physical Chemistry B*, vol. 106, pp. 2447–2452, Mar. 2002.

[156] D. J. Norris, "Electronic Structure in Semiconductors Nanocrystals: Optical Experiment," in *Nanocrystal Quantum Dots, Second Edition* (V. I. Klimov, ed.), ch. 2, Taylor & Francis, Inc., 2010.

[157] E. Taylor, S. Vokos, and J. O'Meara, "Teaching Feynman's sum-over-paths quantum theory," *Computers in Physics*, vol. 12, no. 2, pp. 190–199, 1998.

[158] P. Onorato, "Low-dimensional nanostructures and a semiclassical approach for teaching Feynman's sum-over-paths quantum theory," *European Journal of Physics*, vol. 32, pp. 259–277, Mar. 2011.

[159] J. C. Maxwell, "XXV. On physical lines of force: Part I. - The Theory of Molecular Vortices applied to Magnetic Phenomena," *The London, Edinburgh, and Dublin Philosophical Magazine and Journal of Science*, vol. 21, no. 139, pp. 161–175, 1861.

[160] Y. Couder, S. Protière, E. Fort, and A. Boudaoud, "Walking and orbiting droplets," *Nature*, vol. 437, p. 208, Sept. 2005.

[161] L. de Broglie, "La Nouvelle Dynamique des Quanta," in *Electrons et photons. Rapports et discussions du Cinquième Conseil de Physique tenu à Bruxelles du 24 au 29 octobre 1927 sous les auspices de l'Institut international de Physique Solvay* (H. A. Lorentz, ed.), pp. 105–132, Paris: Gauthier-Villars, 1928.

[162] D. Bohm, "A suggested interpretation of the quantum theory in terms of "hidden" variables. I," *Physical Review*, vol. 85, no. 2, pp. 166–179, 1952.

[163] A. I. Ekimov and A. A. Onushchenko, "Size quantization of the electron energy spectrum in a microscopic semiconductor crystal," *JETP Letters*, vol. 40, no. 8, pp. 1136–1139, 1984.

[164] A. van Dijken, A. Janssen, M. H. P. Smitsmans, D. Vanmaekelbergh, and A. Meijerink, "Size-selective photoetching of nanocrystalline semiconductor particles," *Chemistry of Materials*, vol. 96, no. 26, pp. 3513–3522, 1998.

[165] C. A. Smith, H. W. H. Lee, V. J. Leppert, and S. H. Risbud, "Ultraviolet-blue emission and electron-hole states in ZnSe quantum dots," *Applied Physics Letters*, vol. 75, no. 12, p. 1688, 1999.

[166] M. V. Kovalenko, E. Kaufmann, D. Pachinger, J. Roither, M. Huber, J. Stangl, G. Hesser, F. Schäffler, and W. Heiss, "Colloidal HgTe nanocrystals with widely tunable narrow band gap energies: from telecommunications to molecular vibrations," *Journal of the American Chemical Society*, vol. 128, pp. 3516–3517, Mar. 2006.

[167] E. Lhuillier, S. Keuleyan, and P. Guyot-Sionnest, "Optical properties of HgTe colloidal quantum dots," *Nanotechnology*, vol. 23, p. 175705, May 2012.

[168] W. W. Yu, J. C. Falkner, B. S. Shih, and V. L. Colvin, "Preparation and Characterization of Monodisperse PbSe Semiconductor Nanocrystals in a Noncoordinating Solvent," *ChemInform*, vol. 35, pp. 3318–3322, Oct. 2004.

[169] W. Ma, S. L. Swisher, T. Ewers, J. Engel, V. E. Ferry, H. A. Atwater, and A. P. Alivisatos, "Photovoltaic performance of ultrasmall PbSe quantum dots," *ACS nano*, vol. 5, pp. 8140–7, Oct. 2011.

[170] O. I. Micic, J. Sprague, Z. Lu, and A. J. Nozik, "Highly efficient band-edge emission from InP quantum dots," *Applied Physics Letters*, vol. 68, no. 22, pp. 3150–3152, 1996.

[171] M. D. Tessier, *Synthèse et Spectroscopie de Puits Quantiques Colloïdaux*. PhD thesis, 2013.

[172] Y.-D. Li, H.-W. Liao, Y. Ding, Y.-T. Qian, L. Yang, and G.-E. Zhou, "Nonaqueous Synthesis of CdS Nanorod Semiconductor," *Chemistry of Materials*, vol. 10, pp. 2301–2303, Sept. 1998.

[173] Q. Yang, K. Tang, C. Wang, Y. Qian, and S. Zhang, "PVA-Assisted Synthesis and Characterization of CdSe and CdTe Nanowires," *Journal of Physical Chemistry B*, vol. 106, pp. 9227–9230, 2002.

[174] S. Kan, T. Mokari, E. Rothenberg, and U. Banin, "Synthesis and size-dependent properties of zinc-blende semiconductor quantum rods," *Nature materials*, vol. 2, pp. 155–158, Mar. 2003.

[175] H. Yu, J. Li, R. A. Loomis, L.-W. Wang, and W. E. Buhro, "Two- versus three-dimensional quantum confinement in indium phosphide wires and dots," *Nature materials*, vol. 2, pp. 517–20, Aug. 2003.

[176] H. Yu, J. Li, R. A. Loomis, P. C. Gibbons, L.-W. Wang, and W. E. Buhro, "Cadmium selenide quantum wires and the transition from 3D to 2D confinement," *Journal of the American Chemical Society*, vol. 125, pp. 16168–9, Dec. 2003.

[177] L.-S. Li, J. Hu, W. Yang, and A. P. Alivisatos, "Band gap variation of size- and shape-Controlled colloidal cdse quantum rods," *Nano Letters*, vol. 1, pp. 349–351, July 2001.

[178] C.-W. Chen, K.-H. Chen, C.-H. Shen, A. Ganguly, L.-C. Chen, J.-J. Wu, H.-I. Wen, and W.-F. Pong, "Anomalous blueshift in emission spectra of ZnO nanorods with sizes beyond quantum confinement regime," *Applied Physics Letters*, vol. 88, no. 24, p. 241905, 2006.

[179] Y. H. Yang, X. Y. Chen, Y. Feng, and G. W. Yang, "Physical mechanism of blue-shift of UV luminescence of a single pencil-like ZnO nanowire," *Nano letters*, vol. 7, pp. 3879–83, Dec. 2007.

[180] A. Matulis and F. Peeters, "Renormalized perturbation series for quantum dots," *Journal of Physics: Condensed Matter*, vol. 6, p. 7751, 1994.

[181] A. Gonzalez, B. Partoens, and F. Peeters, "Padé approximants for the ground-state energy of closed-shell quantum dots," *Phys. Rev. B*, vol. 56, no. 24, pp. 15740–15743, 1997.

[182] P. Onorato, "Low-dimensional nanostructures and a semiclassical approach for teaching Feynman's sum-over-paths quantum theory," *European Journal of Physics*, vol. 32, pp. 259–277, Mar. 2011.

[183] M. Balkanski, "Spectroscopy Methods for Low-Dimensional Systems," *Materials and Measurements in Molecular Electronics*, vol. 81, pp. 21–35, 1996.

[184] Y. Zhang, Y. Tan, H. Stormer, and P. Kim, "Experimental observation of the quantum Hall effect and Berry's phase in graphene," *Nature*, vol. 438, pp. 201–204, 2005.

[185] G. Li and E. Y. Andrei, "Observation of Landau levels of Dirac fermions in graphite," *Nature Physics*, vol. 3, pp. 623–627, July 2007.

[186] R. Deacon, K.-C. Chuang, R. Nicholas, K. Novoselov, and A. Geim, "Cyclotron resonance study of the electron and hole velocity in graphene monolayers," *Physical Review B*, vol. 76, pp. 2–5, Aug. 2007.

[187] G. Kalyuzhny and R. Murray, "Ligand effects on optical properties of CdSe nanocrystals," *The Journal of Physical Chemistry B*, vol. 109, no. 15, pp. 7012–7021, 2005.

[188] D. Hines and P. Kamat, "Quantum Dot Surface Chemistry: Ligand Effects and Electron Transfer Reactions," *The Journal of Physical Chemistry C*, vol. 117, no. 27, pp. 14418–14426, 2013.

[189] J. Jasieniak, C. Bullen, J. van Embden, and P. Mulvaney, "Phosphine-free synthesis of CdSe nanocrystals," *The Journal of Physical Chemistry B*, vol. 109, pp. 20665–8, Nov. 2005.

[190] M. B. Mohamed, D. Tonti, A. Al-Salman, A. Chemseddine, and M. Chergui, "Synthesis of high quality zinc blende CdSe nanocrystals," *The journal of physical chemistry. B*, vol. 109, pp. 10533–7, June 2005.

[191] W. W. Yu, J. C. Falkner, B. S. Shih, and V. L. Colvin, "Preparation and Characterization of Monodisperse PbSe Semiconductor Nanocrystals in a Noncoordinating Solvent.," *ChemInform*, vol. 35, pp. 3318–3322, Oct. 2004.

[192] D. Kaiser, *Drawing Theories Apart*. University of Chicago Press, 2005.

List of abbreviations

AFM	Atomic force microscopy
AlGaAs	Aluminum gallium arsenide
AlN	Aluminum nitride
ARPES	Angle resolved photoemission spectroscopy
CCD	Charge-coupled device
CdS	Cadmium sulfide
CdSe	Cadmium selenide
CdTe	Cadmium telluride
CL	Cathodoluminescence
CuCl	Copper chloride
EMA	Effective mass approximation
ESPCI	Ecole Supérieure de Physique et de Chimie Industrielles
FLSM	Fluorescence lifetime scanning microscopy
FWHM	Full width at half maximum
GaAs	Gallium arsenide
GaN	Gallium nitride
HAADF	High-angle annular dark field
HgTe	Mercury telluride
HRTEM	High resolution transmission electron microscopy
InAs	Indium arsenide
InP	Indium phosphide

InSb	Indium antimonide
LPEM	Laboratoire de Physique et d'Etude des Matériaux
LPS	Laboratoire de Physique des Solides
NPL	Nanoplatelet
PbSe	Lead selenide
PL	Photoluminescence
PLE	Photoluminescence excitation
QD	Quantum dot
SAXS	Small angle X-ray scattering
SEM	Scanning electron microscopy
SPAD	Single photon avalanche detector
STEM	Scanning transmission electron microscopy
TB	Tight-binding
TEM	Transmission electron microscopy
TOPO	Trioctylphosphine oxide
ZnO	Zinc oxide
ZnS	Zinc sulfide
ZnSe	Zinc selenide

Arjen Toni DIJKSMAN

Spectroscopie de Boîtes Quantiques Colloïdales de Forme et Taille Contrôlée

Résumé

Les nanocristaux semi-conducteurs colloïdaux, aussi dénommés boîtes quantiques colloïdales, présentent des propriétés d'absorption et de luminescence qui peuvent trouver des applications pratiques, par exemple dans l'imagerie biomédicale, dans les diodes électroluminescentes et dans le photovoltaïque.

Dans cette thèse, nous nous sommes intéressés à synthétiser des nanocristaux CdSe de différentes tailles et à améliorer leurs propriétés de luminescence par la croissance d'une coque épaisse de CdS. Nous avons caractérisé ces nanocristaux coeur-coque CdSe/CdS en microscopie confocale de fluorescence, en corrélant la photoluminescence des mêmes nanocristaux uniques en cathodoluminescence et en imagerie de microscopie électronique à transmission. Cette corrélation a permis de déterminer que l'énergie de photoluminescence de ces nanocristaux correspond à celle de cathodoluminescence.

A partir d'une modélisation du chemin de l'électron dans le nanocristal, nous proposons une relation qui relie l'énergie des transitions excitoniques à sa taille, de façon linéaire. Cette relation tient compte d'un saut de phase et d'un délai qui correspondent à l'électron rebondissant à la surface. La confrontation de cette relation aux données expérimentales fait ressortir des invariants remarquables qui indiquent que cette relation est transposable à plusieurs matériaux en confinement quantique fort 1D, 2D et 3D.

Mots clefs

Nanocristaux semi-conducteurs ; boîtes quantiques colloïdales ; CdSe ; photoluminescence ; microscopie confocale ; cathodoluminescence ; modèle électronique

Abstract

Colloidal semiconductor nanocrystals, also called quantum dots, show properties of absorption and luminescence that find practical applications, such as biomedical imaging, light-emitting diodes and photovoltaics.

In this thesis, we have synthesized CdSe quantum dots of different sizes and have improved their luminescent properties by growing a thick shell of CdS. We characterized these core-shell CdSe/CdS quantum dots with confocal fluorescence microscopy, correlating their photoluminescence with their cathodoluminescence and with their transmission electron microscopy images. This correlation was used to determine that the photoluminescence energy corresponds to the cathodoluminescence energy.

We propose a model that describes the electron's path in a nanocrystal. This results in a linear equation that relates the energy of excitonic transitions to the size of the nanocrystal. This equation takes into account a phase jump and a time delay that corresponds to the electron bouncing at the surface. Probing this equation with experimental data reveals remarkable invariants that indicate that it can be applied to various materials in the 1D, 2D and 3D strong quantum confinement range.

Keywords

Semiconductor nanocrystals; colloidal quantum dots ; CdSe ; photoluminescence ; confocal microscopy ; cathodoluminescence ; electron model